



UNIVERSITAT ROVIRA I VIRGILI

INSIGHTS INTO THE CO-CATALYST EFFECTS IN LIGHT DRIVEN REACTIONS FOR WATER SPLITTING AND CARBON DIOXIDE REDUCTION

Marta Borges Ordoño

ADVERTIMENT. L'accés als continguts d'aquesta tesi doctoral i la seva utilització ha de respectar els drets de la persona autora. Pot ser utilitzada per a consulta o estudi personal, així com en activitats o materials d'investigació i docència en els termes establerts a l'art. 32 del Text Refós de la Llei de Propietat Intel·lectual (RDL 1/1996). Per altres utilitzacions es requereix l'autorització prèvia i expressa de la persona autora. En qualsevol cas, en la utilització dels seus continguts caldrà indicar de forma clara el nom i cognoms de la persona autora i el títol de la tesi doctoral. No s'autoritza la seva reproducció o altres formes d'explotació efectuades amb finalitats de lucre ni la seva comunicació pública des d'un lloc aliè al servei TDX. Tampoc s'autoritza la presentació del seu contingut en una finestra o marc aliè a TDX (framing). Aquesta reserva de drets afecta tant als continguts de la tesi com als seus resums i índexs.

ADVERTENCIA. El acceso a los contenidos de esta tesis doctoral y su utilización debe respetar los derechos de la persona autora. Puede ser utilizada para consulta o estudio personal, así como en actividades o materiales de investigación y docencia en los términos establecidos en el art. 32 del Texto Refundido de la Ley de Propiedad Intelectual (RDL 1/1996). Para otros usos se requiere la autorización previa y expresa de la persona autora. En cualquier caso, en la utilización de sus contenidos se deberá indicar de forma clara el nombre y apellidos de la persona autora y el título de la tesis doctoral. No se autoriza su reproducción u otras formas de explotación efectuadas con fines lucrativos ni su comunicación pública desde un sitio ajeno al servicio TDR. Tampoco se autoriza la presentación de su contenido en una ventana o marco ajeno a TDR (framing). Esta reserva de derechos afecta tanto al contenido de la tesis como a sus resúmenes e índices.

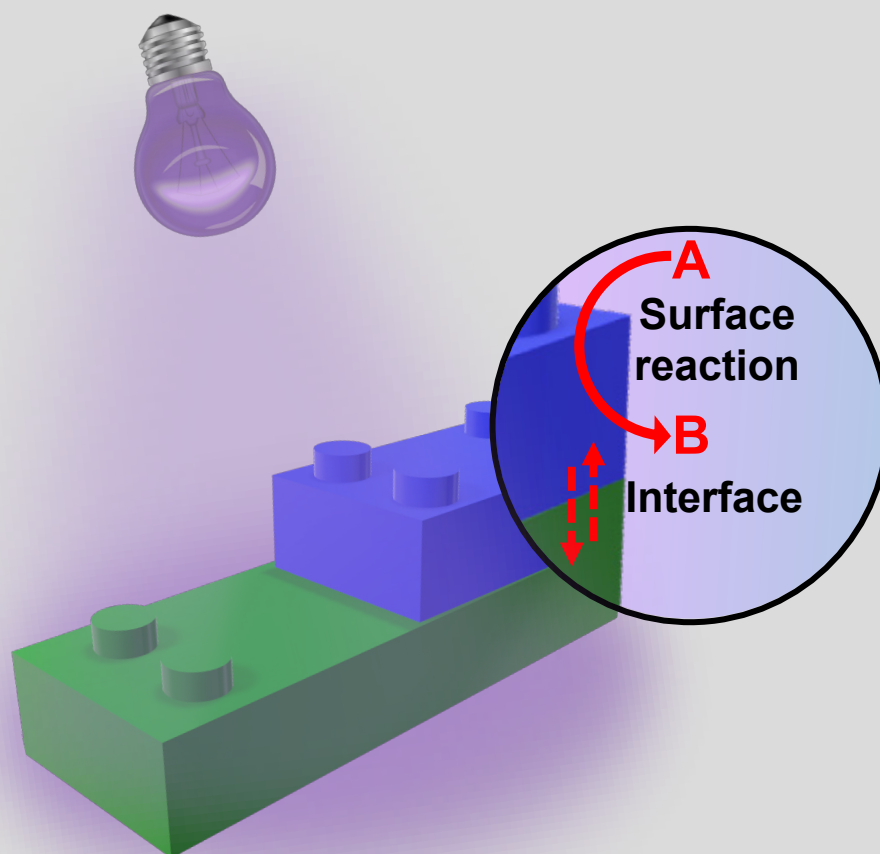
WARNING. Access to the contents of this doctoral thesis and its use must respect the rights of the author. It can be used for reference or private study, as well as research and learning activities or materials in the terms established by the 32nd article of the Spanish Consolidated Copyright Act (RDL 1/1996). Express and previous authorization of the author is required for any other uses. In any case, when using its content, full name of the author and title of the thesis must be clearly indicated. Reproduction or other forms of for profit use or public communication from outside TDX service is not allowed. Presentation of its content in a window or frame external to TDX (framing) is not authorized either. These rights affect both the content of the thesis and its abstracts and indexes.



UNIVERSITAT
ROVIRA I VIRGILI

Insights into the co-catalyst effects in light driven reactions for water splitting and carbon dioxide reduction

MARTA BORGES ORDOÑO



DOCTORAL THESIS
2018

DOCTORAL THESIS

INSIGHTS INTO THE CO-CATALYST EFFECTS IN LIGHT DRIVEN REACTIONS FOR WATER SPLITTING AND CARBON DIOXIDE REDUCTION

MARTA BORGES ORDOÑO

Supervised by:

Prof. Dr. Atsushi Urakawa

ICIQ-URV



UNIVERSITAT
ROVIRA I VIRGILI

Tarragona

2018

Prof. Dr. Atsushi Urakawa
Group Leader
Institute of Chemical Research of Catalonia (ICIQ)
The Barcelona Institute of Science and Technology
Av. Països Catalans 16
43007 Tarragona, Spain

CERTIFIES THAT:

The present study, entitled “Insights into the co-catalyst effects in light driven reactions for water splitting and carbon dioxide reduction”, presented by Marta Borges Ordoño for the award of the degree of Doctor, has been carried out under my supervision at the Institute of Chemical Research of Catalonia (ICIQ), and that it fulfils all the requirements to obtain the Degree of Doctor in Chemical Science and Technology.

Tarragona, 28th of September, 2018

Doctoral Thesis Supervisor

浦川 篤

Prof. Dr. Atsushi Urakawa



UNIVERSITAT
ROVIRA i VIRGILI

Acknowledgements

First, I would like to thank my supervisor Prof. Atsushi Urakawa for giving me the opportunity to join his group to carry out my doctoral studies four years ago. I appreciate his trust and support that helped me to grow as researcher and carry on a successful and complete work. I am grateful to him for letting me see another perspective of science and giving me the facilities to participate in congresses and synchrotron beamtimes, those helped me to expand my scientific knowledge. Thank you for giving me the tools to play around building systems and letting fly my creativity, also for the long scientific discussions, and the optimism and patience through the project challenges. It has been a pleasure to work with you Sensei.

I would like to express my sincere gratitude to all the scientific and non-scientific ICIQ staff, making my life much easier during the past years. Special thanks to Dr. Miguel González Hevia and Dr. Georgiana Stoica (Heterogenous Catalysis Unit) for introducing me to new characterization techniques and allowing me to use the unit's equipment on my own. Thanks to Dr. Fernando Bozoglian (Spectroscopy and Reaction Kinetics Unit), Marta Martinez (X-Ray Diffraction Unit), and Dr. Simona Curreli (Chromatography, Thermal Analysis and Electrochemistry Unit) for their support. Many thanks to José Luis León (Mechanical Workshop) and Xavier Asensio (Glass Blowing Workshop) for solving last minute problems and making feasible crazy ideas into real reactor systems. Marc and Jesús (our logistics guys) also deserve a big thank you for its happiness and good vibes already at early morning, let's not mention how good stories teller you are. I would also thank to Aurora Càceres for the great administrative support and your help during all this time, as well as to Noelia Flores for your support to what probably was one of the most challenging research stays. Thanks to Marta and Eloísa for cheering me up and sharing your doctoral experiences.

Now it is the turn to express a big thank you to all the current members of Urakawa's lab; Atul, Jordi, Juanjo, Rohit, Lingjun, Sorin, and Nat, and to the former ones, Antonio, Luis, Dina, Tsuyoshi, Shunsaku, Shintaro, Andrea, Takuya, Tetsuya, Dragos, Yi, Murli, Joan, Sergio, Satoshi, Silvia, and Rui. Big thank you to Dr. Antonio Bazzo (Xut), this

project would not have happened without your ideas and hard work building functioning reactor setups. Thanks for all the discussion, but above all, your excellent cooking skills (pasta maestro!). Thank you to Dr. Atul Bansode for all the scientific and non-scientific discussions, for all the help in the lab whenever I was lost. For teaching me so many things, and most importantly for encouraging me (especially during my first synchrotron beamtime, Spock). Special thanks to Dr. Jordi Ampurdanés for all the support and help in the lab, with Matlab, and many other techniques, and for keeping always a positive atmosphere everywhere. Good memories in the lab also come to my mind with Dr. Gaikwad (chocolate), thanks for all our jokes and songs. Thank you to all the Japanese community; specially, to Dr. Tsu and his family (Yoko, Toyo, and Machino). Good laughs and parties, it was very nice meeting you again in Japan. Shunsaku, it was great to work with you, although at the beginning our communication was not so fluent, your aptitudes and knowledge about calculations were very helpful. As well with Dr. Shintaro Hara, it was so nice to learn some microscopy tools from you, although it was for a short time. Thank you all and for those who made Japan so nice! And thank you all for tons of good memories!

Thank you to Prof. Wey Yang Teoh for welcoming on his group and showing me another perspective of looking at the results, also for your lessons that brought me back to university, and your support over the last months. Thank you to the members from Teoh's group specially to Xiaomeng, Amy, Rocky, and Violet, that not also assisted me during my stay but also taught me a lot about their cultures.

Special thanks to Dr. Pieter Glatzel for your patience and support during synchrotron beamtime and further data analysis and discussions. Your inputs based on physics purely helped to improve the work quality.

Dragos, Juanjo, y Silvia, ¡muchas gracias chicos! Ha sido un placer compartir lab con vosotros. Juanjo y Silvia me habéis hecho reír en los malos momentos, y habéis hecho menos larga esta espera, casi casi ya estoy a la última en música gracias a vuestros grandes gustos musicales. Drac, desde el día 0 donde compartíamos mesa hasta el último, tus consejos y tu sabiduría me han hecho aprender nuevas técnicas y cómo cuestionarme científicamente todos los resultados, gracias! No me iba a olvidar de Dana, gracias por todos los buenos momentos entre cervezas y música, y por esos skypes y visitas. ¡Gracias a todos por vuestra paciencia, habéis sido mi lab family!

Also, I would like to thank my UK friends Loredana and Iain, Maria Elena and Juan Carlos, and Dora and James, I really appreciate your encouragement when I decided to start the PhD. Specially to Lore and Maria Elena, always supportive despite the distance.

I no podia oblidar la gent de Reus i Tarragona, gràcies per tots els moments fora de la feina, per formar-n'he part i fer que el temps hagi passat volant. En especial a tu Jordi, moltíssimes gràcies per haver compartit tot el que la tesis comporta i aguantar tan bé en els últims mesos, pel teu suport incondicional que ha facilitat poder arribar fins aquí. Gràcies; Aleix, Anna, Lúdia, Ramón, José, Pili, Enzo, Cris, Jordi, Laura, Victor, Lucy, David i Katie. Aleix moltes gràcies per els teus consells gràfics! David i Katie, gràcies per tots els bons moments, experiències viscudes, i tot el vostre suport.

No podia acabar aquesta llista d'agraïments sense reconèixer a la meva família, gràcies per tot el suport rebut en especial als meus pares (Agustí i Pepi) i germà (Marc) per escoltar moltes vegades sense saber de que parlava, i per animar-m'he en els moments difícils. Com sempre heu estat allí quant més us he necessitat, aquesta tesis també us pertany a vosaltres, moltes gràcies!

“Rovira i Virgili” University, ICIQ Fundation, Ministerio de Economia y Competitividad (MINECO), and SEVERO OCHOA grant are kindly acknowledged for financial support, making this doctoral project possible.



UNIVERSITAT
ROVIRA I VIRGILI



Table of contents

CHAPTER 1: Introduction and overview

1.1 Energy sources and CO ₂ mitigation strategies	2
1.1.1 Non-renewable energies.....	2
1.1.2 Alternative energies	3
1.1.2.1 Solar energy.....	5
1.2 Carbon dioxide reduction and water splitting	6
1.2.1 Heterogeneous photocatalytic materials.....	7
1.2.2 Strategies to improve photocatalysts efficiency	9
1.2.2.1 Promoters or co-catalysts.....	9
1.2.2.2 Sacrificial agents	11
1.2.3 Photocatalytic landmarks	12
1.3 Aim and overview of the thesis.....	14
Bibliography	17

CHAPTER 2: Materials and methods

2.1 Photocatalyst preparation.....	22
2.1.1 Ga ₂ O ₃ based materials	23
2.1.2 TiO ₂ based materials	23
2.2 Reactor setup for continuous photocatalytic reactions	24
2.2.1 Slurry and gas phase reactors	25
2.2.2 Illumination sources	26
2.2.3 Analytical system	27
2.3 Spectroscopic techniques and processing tools.....	28

2.3.1 Ultraviolet and visible diffuse reflectance spectroscopy	29
2.3.2 X-ray absorption and emission spectroscopies.....	30
2.3.3 Diffuse reflectance infrared Fourier transformed spectroscopy.....	33
2.3.4 Modulation excitation spectroscopy by phase-sensitive detection and multivariate curve resolution	35
2.4 Electroanalytical methods	37
2.4.1 Rotating disk electrode and photoelectrochemical cell	39
Bibliography	43

CHAPTER 3: Electronic structure modifications of Ga₂O₃

3.1 Introduction	48
3.2 Experimental	50
3.2.1 Materials	50
3.2.2 Reaction setup.....	50
3.2.3 Materials characterization	50
3.2.4 Modulation excitation spectroscopy (MES).....	51
3.3 Results and discussion.....	52
3.3.1 Photocatalytic activity of Zn-Ga ₂ O ₃ and Rh-Cr/Zn-Ga ₂ O ₃	52
3.3.2 Geometrical and electronic structure changes by Zn-loading	53
3.3.3 Role of Rh-Cr co-catalyst.....	58
3.3.4 Synergistic effects of Rh-Cr and Zn	60
3.4 Conclusions.....	62
Bibliography	64

CHAPTER 4: Reaction mechanism of modified TiO₂ with promoters

4.1 Introduction.....	68
4.2 Experimental.....	69
4.2.1 Materials	69
4.2.2 Reaction setup.....	70
4.2.3 Multivariate spectral analysis.....	70
4.3 Results and discussion.....	71
4.3.1 Photocatalytic CO ₂ reduction by TiO ₂ , Co/TiO ₂ and Pt/TiO ₂	71
4.3.2 Mechanistic study of photocatalytic CO ₂ reduction by <i>in situ</i> DRIFTS.....	73
4.3.2.1 Pt/TiO ₂	73
4.3.2.2 TiO ₂ and Co/TiO ₂	77
4.3.3 Origin of transient activity and deactivation	79
4.4 Conclusions.....	80
Bibliography	81

CHAPTER 5: Electrochemical investigations of modified TiO₂ with promoters

5.1 Introduction	86
5.2 Experimental	88
5.2.1 Materials and electrodes preparation.....	88
5.2.2 Reaction setup.....	89
5.2.3 Electrochemical characterization techniques.....	89
5.3 Results and discussion.....	90
5.3.1 Photocatalytic water splitting with TiO ₂ modified materials	90
5.3.2 Redox reactions for Pt and Co decoupled from TiO ₂ (RDE)	92
5.3.2.1 Hydrogen evolution reaction (HER) and oxygen reduction reaction (ORR)	92

5.3.2.2 Oxygen evolution reaction (OER).....	95
5.3.3 Water oxidation with Pt and Co modified TiO ₂ (PEC).....	95
5.4 Conclusions.....	97
Bibliography	99

CHAPTER 6: Conclusions and outlook

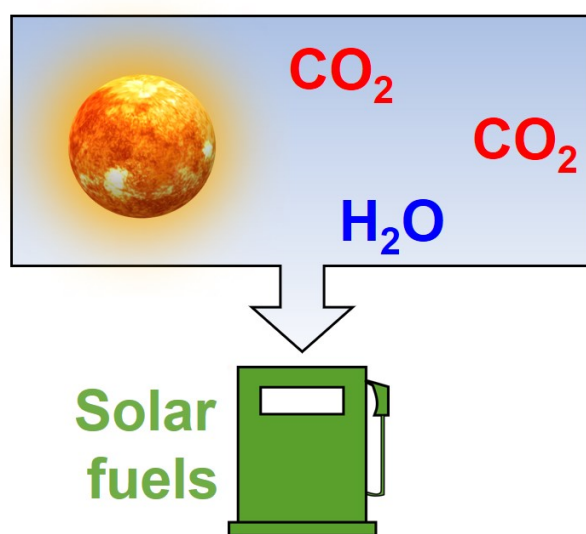
6.1 Summary of thesis.....	104
6.2 Outlook.....	107
6.2.1 Preliminary studies with spectroelectrochemical cell in diffuse reflectance mode.....	108
6.2.2 DRIFTS coupled to photoelectrochemical cell	110
Bibliography	112

CHAPTER 7: Appendices

Appendix A Supplementary Information of Chapter 3.....	116
Appendix B Supplementary Information of Chapter 4.....	127
Shorthand and glossary	137
List of publications.....	141
Curriculum Vitae.....	145

1.

Introduction and overview



1.1 Energy sources and CO₂ mitigation strategies

1.1.1 Non-renewable energies

Over the last 200 years the world population has been growing exponentially. According to the Global Development Programme at the University of Oxford, today's world population is about seven billion of habitants which is seven times more than 200 years ago [1]. This rapid growth of the society has generated a massive energy demand due to the elevated consumption rates of our primary energy source. We are relying on an energy supply based on carbon containing compounds that were formed from plants and animals remains millions of years ago, namely fossil fuels which are scarce and a non-renewable energy source.

Concretely, our energy supply is based on three major forms of fossil fuels: coal, oil, and natural gas. Since the industrial revolution, the combustion of coal has been widely used to produce electricity and heat; nevertheless, coal is being replaced by natural gas due to the environmental and health problems associated with its utilization. On the other side, oil is one of the principal feedstocks for a wide variety of industrial products from gasoline to chemicals. Oil extraction and refinement processes are well-established technologies, and despite the oil crisis in the 1970s, oil production still increased during the 20th-21st centuries. Recent studies have predicted that the oil and natural gas resources might not last more than 50 years if energy trends follow the same directions as last decades [2]. In 2017, 81.4% of the world's total primary energy supply was still obtained from non-renewable sources corresponding to oil (31.7%), coal (28.1%), and natural gas (21.6%) reflecting the high demand of fossil fuels leading to its depletion [3].

Together with the issue of depleting fossil fuels, increasing consumption of coal and oil from human activities since the industrial revolution has contributed to gas pollutants emissions into the atmosphere, mainly as carbon dioxide (CO₂). CO₂, water vapor, methane, and ozone produced the so-called greenhouse effect; this process occurs when solar light is absorbed by gas molecules and emitted back to the surface, thus raising the planet temperature and causing climate change. Currently, the concentration of CO₂ (the main gas causing greenhouse effect) is constantly

monitored as shown from the CO₂ emissions and temperature increase maps in **Figure 1.1**. Last year, global temperatures increased around 1 °C which is already very close to the stipulated limits of 1.5 °C set by the Paris agreement. Clearly, new technologies are required to emerge in the near future to reduce the CO₂ levels, e.g. replacement of primary carbon sources by renewable energy sources, CO₂ recycling, etc.

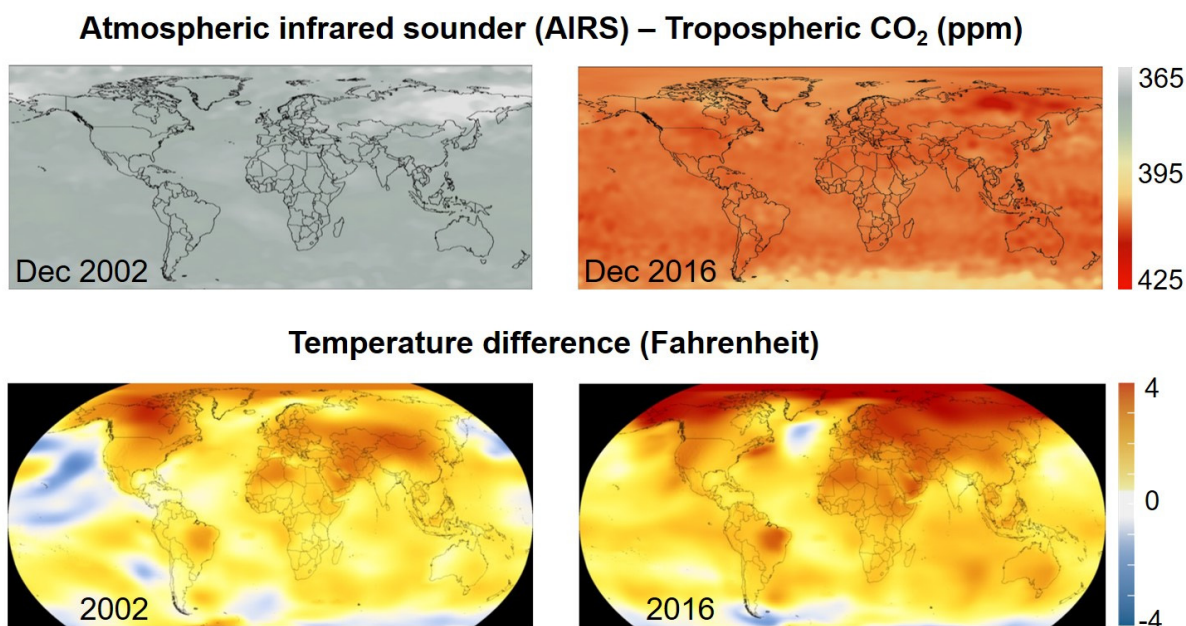


Figure 1.1. Increase in CO₂ concentration (**top**) and temperatures (**bottom**) in the world between 2002 and 2016. Data from the National Aeronautics and Space Administration (NASA) source [4].

1.1.2 Alternative energies

Renewable energy sources account for a 25% of the global energy generation, thus they are a good approach to replace fossil fuels and mitigate greenhouse gases. Therefore, development of energy systems without carbon footprint (carbon-neutral) that are economically and environmentally friendly has become one of the major objectives for researchers around the world. Renewable energies are based on the earth's natural and most abundant resources such as sun, air, and water (**Figure 1.2**). Some of the energy sources are only available where nature makes it feasible such as hydropower and geothermal; on the other hand, power generated from sun, wind, and sea is more flexible and can be widely implemented everywhere.

Chapter 1

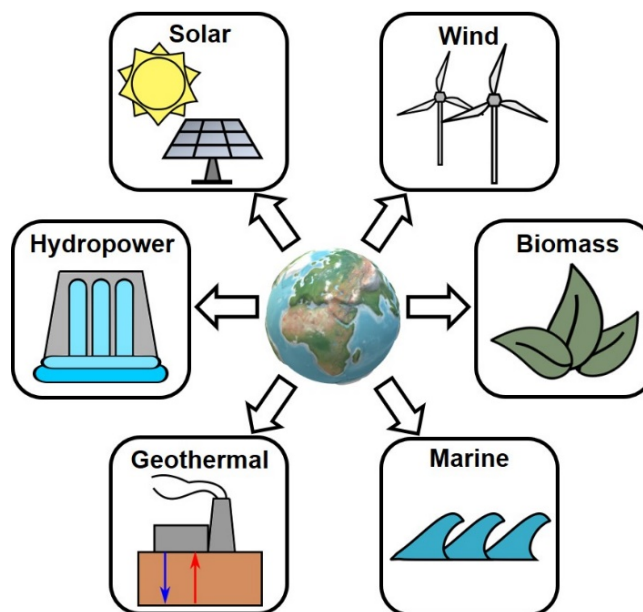


Figure 1.2. Different types of renewable energies obtained from natural sources; solar, wind, biomass, hydropower, geothermal, marine (tidal and wave) energies.

Energy from sun can be utilized to provide electricity through solar photovoltaics or can be directly used for conversion of water and other chemicals, which will be discussed in following sections. The electricity from wind is produced by a wind turbine that rotates converting the kinetic energy into electrical energy, it is a widely implemented technology despite its environmental impacts and costs [5]. Strongly correlated to the wind and sun power are wave and tidal energies, which are based on the ocean movements. Despite the large quantity of sea water in the planet (almost 75% of Earth is covered by ocean), those technologies are costly and might damage the marine life. Furthermore, biomass such as cellulose can be used as feedstock to produce ethanol as motor fuel. However, there are some technical problems associated with the synthesis process and more importantly car engines should be replaced for better ethanol utilization [6]. In brief, despite the great potential of green energies, they are still far from replacing fossil fuels on a large scale due to the high cost of some of these technologies.

Additionally, energy fluctuations from renewable energy sources e.g. on a day without wind, kinetic energy will not be produced, can be overcome by storing energy in chemical compounds, e.g. H_2 or CH_3OH . The so-called *hydrogen economy* proposes the delivery of H_2 to generate energy; industrially, H_2 is produced by steam

reforming, although it could be replaced by a greener solution such as water electrolysis. Nevertheless, the large cost associated with the industrial process (reforming of fossil fuels) and the infrastructure required for storage and transportation of H_2 - which is a flammable and explosive gas - limits its potential applications.

George A. Olah suggested an alternative pathway for converting atmospheric CO_2 into fuels, termed *methanol economy*. The methanol economy introduces a cyclic carbon process where the excess of CO_2 is hydrogenated to produce CH_3OH and/or its derivatives (**Figure 1.3**), in contrast to the unidirectional route from fossil fuels. Unlike H_2 , storage of CH_3OH is less hazardous since CH_3OH is less flammable. However, the important part of this methanol economy is the requirement of H_2 , which can be supplied from renewable energy sources [7, 8]. In this manner, not only CO_2 is continuously captured and transformed but also green energy source such as sunlight is utilized to obtain H_2 .

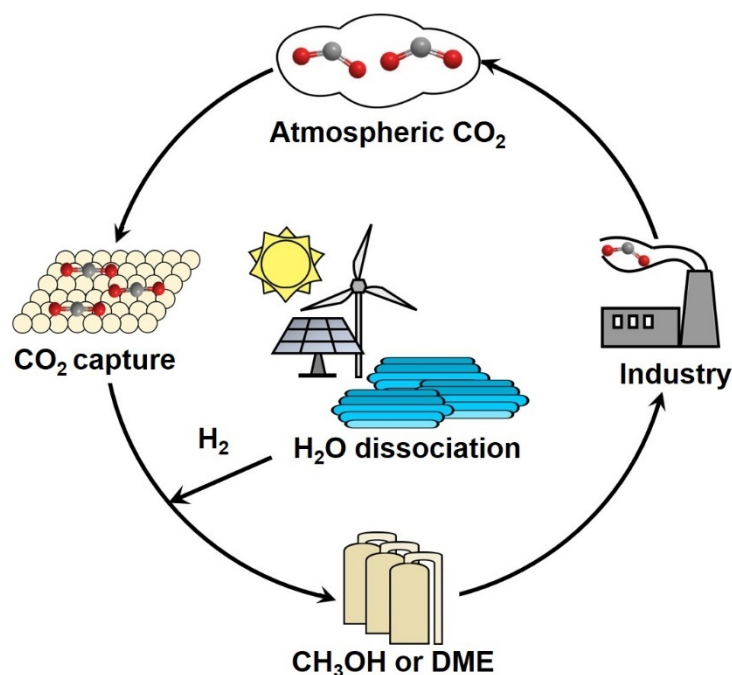


Figure 1.3. Carbon cycle suggested from methanol economy [7].

1.1.2.1 Solar energy

Among all the renewable energies, sun is the most important and abundant energy source. The amount of sunlight that falls on Earth during 1 h is equivalent to all the energy consumed in one year; also, this represents the reason why the vast majority of renewable energy sources depend on the solar energy, except for geothermal and tides energies. The power generation by sunlight can be achieved by

Chapter 1

transferring directly the solar energy to electricity by using photovoltaic devices [9]. Solar cell devices have sun-efficiencies from 20-40% [10]. Despite the efforts for developing alternative semiconductors from silicon, the cost of this technology and the issues associated with the electricity generation depending on the weather conditions and diurnal cycles have delayed its implementation in Europe.

On the other hand, the influence of sunlight into natural processes is well known, in particular the reaction of natural photosynthesis in green plants. In nature, the solar radiation is converted into chemical energy (glucose); likewise, CO₂ is captured and converted into organic compounds leading to a carbon-neutral cycle. Although the natural photosynthesis is highly selective, it cannot cope up with current CO₂ emission rate. Based on the photosynthetic process, the conversion of solar energy into chemical energy offers a sustainable approach to mitigate atmospheric CO₂ concentrations, leading to the so-called *artificial photosynthesis*.

1.2 Carbon dioxide reduction and water splitting

In literature, *artificial photosynthesis* is also used to describe photocatalytic water splitting reaction which consists of dissociation of H₂O molecules into H₂ and O₂ (Eq. (5), Figure 1.4). CO₂ reduction goes hand in hand with water splitting reaction, since H₂O is one of the most abundant starting materials, it is often used as the source of protons to reduce CO₂ (H₂ could also be employed). Consequently, CO₂ reduction in the presence of H₂O competes with water splitting reaction from the reduction of H₂O into H₂ since it is energetically favoured over CO₂ reduction (Eq. (6) compared with Eq. (2), Figure 1.4). Proton transfer from H₂O or H₂ is always coupled with an electron transfer, thus photoreduction of CO₂ involves a series of multielectron processes to break and form new chemical bonds [11]. Despite the thermodynamic and kinetic limitations, distinct fuels have been obtained from the photocatalytic reaction of CO₂, CH₃OH and CH₄ being the most detected products [12].

Several strategies have been attempted to maximize the efficiency of these reactions by homogeneous and heterogeneous catalytic approaches. At the industrial scale, heterogeneous photocatalytic reactions are preferred since utilization of molecular catalysts increases the process cost because metal complexes (i.e.

ruthenium and rhenium) are expensive catalysts [13-16]. Also, performing reactions in liquid and batch conditions is limited by the solubility of CO₂ in H₂O [17]. Both constrains can be overcome by performing the reaction heterogeneously in gas-phase (vapour phase) where water saturated CO₂ is used, which in addition resolves the issue of products separation obtained from the reaction performed in liquid-phase.

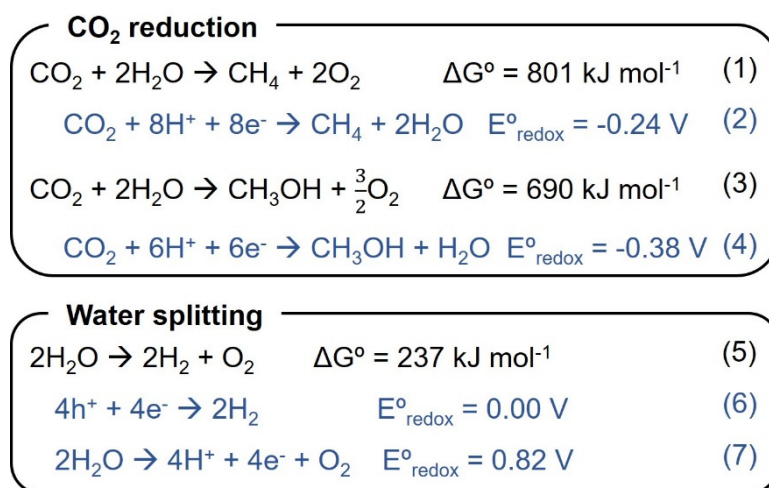


Figure 1.4. Overall CO₂ reduction (1) and water splitting (5) reactions, and electrons/protons involved in CH₄ (2), CH₃OH (4), H₂ (6), and O₂ (7) evolution [14, 18].

Alternatively, CO₂ reduction and water splitting reactions have also been investigated by electrochemical methods [19], by applying a potential energy to an electrode containing the photocatalytic material redox reactions occur. Moreover, photocatalytic and electrocatalytic strategies can be combined in the so-called photoelectrocatalytic cell (PEC) [20, 21], enhancing even more catalytic reaction efficiencies when working at the optimum conditions. Nevertheless, coupling photo-electrochemical principles increases complexity of understanding the reaction mechanisms. Hence, it is scientifically more meaningful to study the reactions independently and later implement a combined approach. Based on this background, photocatalytic and electrocatalytic reactions have been investigated mainly focusing on heterogenous photocatalysts as presented in next section.

1.2.1 Heterogeneous photocatalytic materials

Photocatalytic reactions require a photocatalyst that harvest light and drives the reduction and oxidation reactions. Heterogeneous photocatalysts are usually

Chapter 1

semiconductors materials which absorb a characteristic range of the light spectrum with sufficient energy to produce an internal charge carrier separation upon light absorption. Photon absorption leads to excitation of electrons that are promoted into available energy states in the conduction band (CB) leaving behind a vacancy (hole) in the valance band (VB) (**Figure 1.5**). Induction of charge separation (electron-hole) is only initiated if the light energy is equal to or larger than the semiconductor bandgap ($h\nu \geq E_g$) [22]. Besides the required energy to overcome the semiconductor bandgap and the effective charge mobility, the position of band edge is crucial for catalytic reactions. If bands are located below the energy required for reducing or oxidizing species at the photocatalyst surface then reaction will not occur [23].

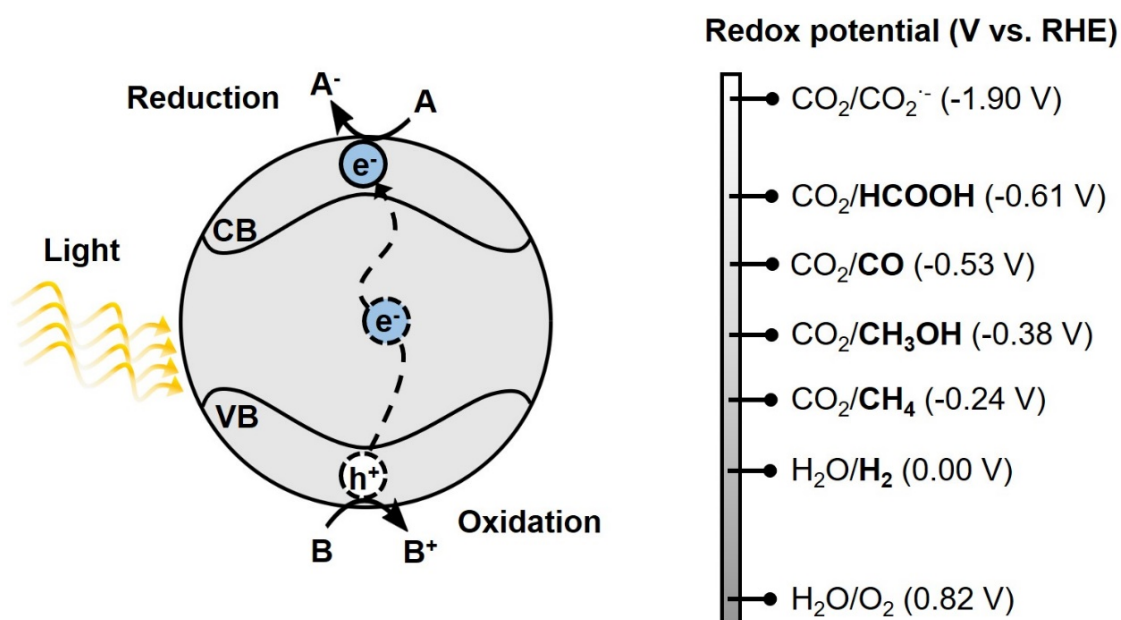


Figure 1.5. Schematic diagram of a semiconductor VB (valence band) and CB (conduction band) with induced charge carrier upon light absorption (**left**). Required band edge energies for certain redox reactions to take place vs. the reference hydrogen electrode (RHE) potentials (**right**).

The bandgap of semiconductors is a very important parameter to consider since it is directly related with the efficiency of light absorption. The bandgap and irradiation wavelength are inversely proportional, the larger the bandgap, shorter the adsorption wavelength. Still, the most studied semiconductor materials have a wide-bandgap limiting the sunlight absorption to the spectral UV region (**Figure 1.6**), as is the case for the widely employed photocatalyst TiO₂ [24]. There are different approaches

reported in literature to enhance photocatalysts efficiency, e.g. addition of promoters or co-catalysts and utilization of sacrificial agents in the reaction media.

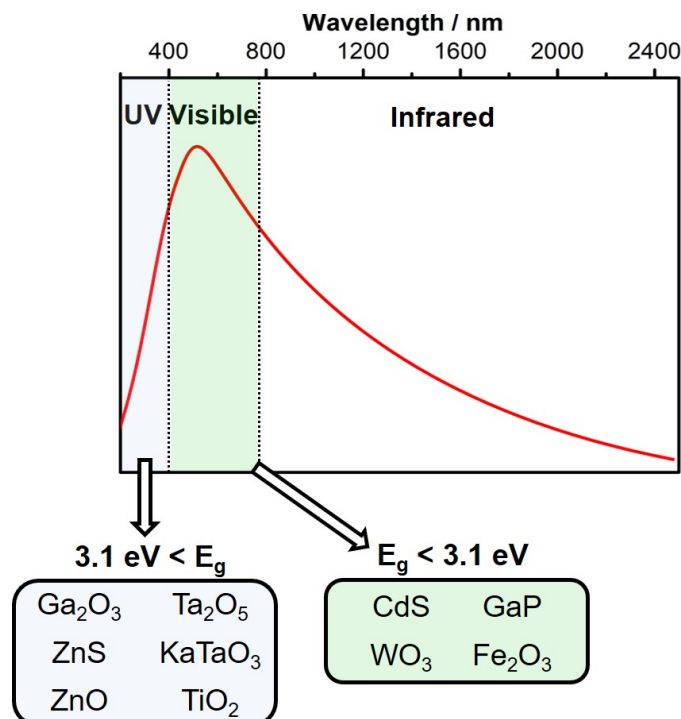


Figure 1.6. Solar spectrum divided into ultraviolet (UV), visible (Vis), and infrared (IR) regions. Main photocatalysts materials with bandgap (E_g) in the UV (blue) and visible (green) regions [25, 26].

1.2.2 Strategies to improve photocatalysts efficiency

1.2.2.1 Promoters or co-catalysts

Bare semiconductor materials usually lack surface active sites for redox reactions to take place, thus leading to poor photocatalytic performance since electron-hole recombination occurs very fast. Modification of semiconductor surface is the most suitable strategy to improve photocatalysts performance, e.g. loading metals, non-metals, or dyes [27]. Among them, the most employed strategy is the metal-loading by impregnation or photodeposition methods to create an interface between metal and semiconductor, also known as co-catalysts or metal promoters.

Addition of co-catalysts promotes the electron-hole trapping from the semiconductor upon material illumination. The formation of a Schottky barrier between the metal and semiconductor is originated from the band bending of the semiconductor material. Initially, when a metal and a n-type semiconductor material are isolated the

Chapter 1

Fermi levels (E_f) are located at different energies (**Figure 1.7-a**), whereas if the metal and n-type semiconductor are in contact with each other the flux of electrons from the semiconductor to the metal induces the alignment of both Fermi levels (**Figure 1.7-b**). The redistribution of charges within the semiconductor material induces the formation of a space charge layer interface (Schottky barrier), causing the bending of the valence and conduction bands of the semiconductor. In the end, the semiconductor has an excess of positive charge and the metal is charged negatively [28, 29].

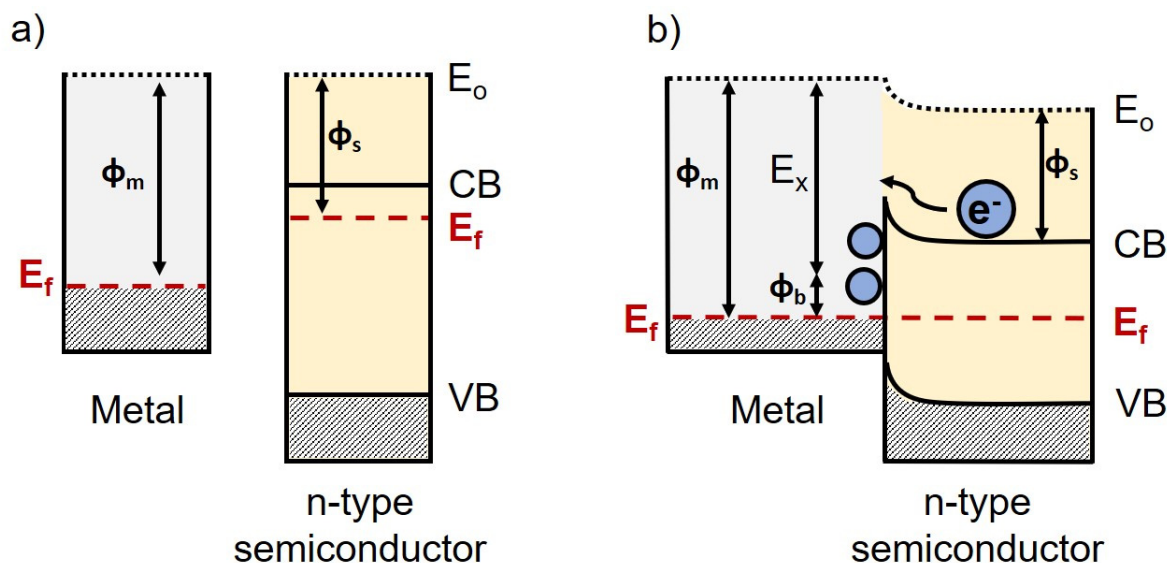


Figure 1.7. a) Isolated metal and n-type semiconductor, b) Schottky barrier formation due to the contact between a metal and a n-type semiconductor. Semiconductor conduction band (CB) and valence band (VB), Fermi level in red (E_f), metal and semiconductor work functions (ϕ), barrier height (ϕ_b), and electron affinity (E_x).

Co-catalysts (metal or metal oxides) are most frequently loaded on semiconductors by impregnation or photodeposition methods which are simple and reproducible, thus allowing to work with a wide variety of metal/metal oxides combinations. In general, doping a semiconductor with a metal promoter facilitates the charge (electron-hole) separation due to the electron trapping or donation from the semiconductor material to the metal resulting in higher photocatalytic activity [30]. Pt has been widely used for photocatalytic water splitting in combination with different types of semiconductors, in particular, Pt-loaded on TiO_2 acts as electron sink since its work function is at higher energy (5.36 eV) than TiO_2 bandgap (4.6 eV), as shown **Figure 1.7-b** [31]. Pt retards the electron-hole recombination rates increasing

photocatalytic efficiencies, thus more electrons participate in reduction reactions and more holes interfere in oxidation reactions; additionally, Pt has catalytic role which promotes H₂ formation [32].

Other noble metals such as Pd, Au, Ru, Rh, and Ag have also been reported as efficient co-catalysts [33, 34]. Similar to Pt, Fermi levels equilibration from metal particle and TiO₂ are indicative of efficient electron transfer promoting photocatalytic reactions. Additionally, Ag and Au nanoparticles present localized surface plasmonic resonance (LSPR) under visible light due to electron transfer from the metal to the semiconductor [35]. Also, transition-metal oxides such as NiO [36] and RuO₂ [37] are known to be efficient co-catalysts for photocatalytic water splitting. RuO₂, like IrO₂, was found to be a good water oxidation co-catalyst [38]. In particular, rhodium and chromium mixed oxides (Rh_{2-y}Cr_yO₃) were found to be beneficial for the overall water splitting in (Ga_{1-x}Zn_x)(N_{1-x}O_x) catalyst [37, 39]. Maeda *et. al* proposed that the Rh-Cr facilitated charge transfer between the photocatalyst and co-catalyst, inhibiting the charge recombination due to the creation of active sites for H₂ evolution [40].

1.2.2.2 Sacrificial agents

Given the complexity of photocatalytic reactions, sacrificial agents can be used to evaluate the semi-reactions (redox) involved in water splitting in solution phase, such as to understand if a photocatalyst is capable of water oxidation. Commonly, electrons are photoexcited from VB to CB and then at photocatalyst surface electrons are involved in reduction reactions leaving a hole in the VB.

If an electron donor is added to the reaction media (e.g. water), the photogenerated holes in the photocatalyst will oxidize the electron donor instead of water, thus water reduction is facilitated. Among electron donors, methanol is the most widely used. Photogenerated holes will oxidize and decompose methanol, so the electrons can participate in the water reduction evolving only hydrogen (**Figure 1.8-a**) [34]. However, in the presence of an electron acceptor such as Ag⁺, electrons will participate in the silver reduction instead of water reduction to H₂ and only O₂ will be evolved (**Figure 1.8-b**) [41, 42].

Chapter 1

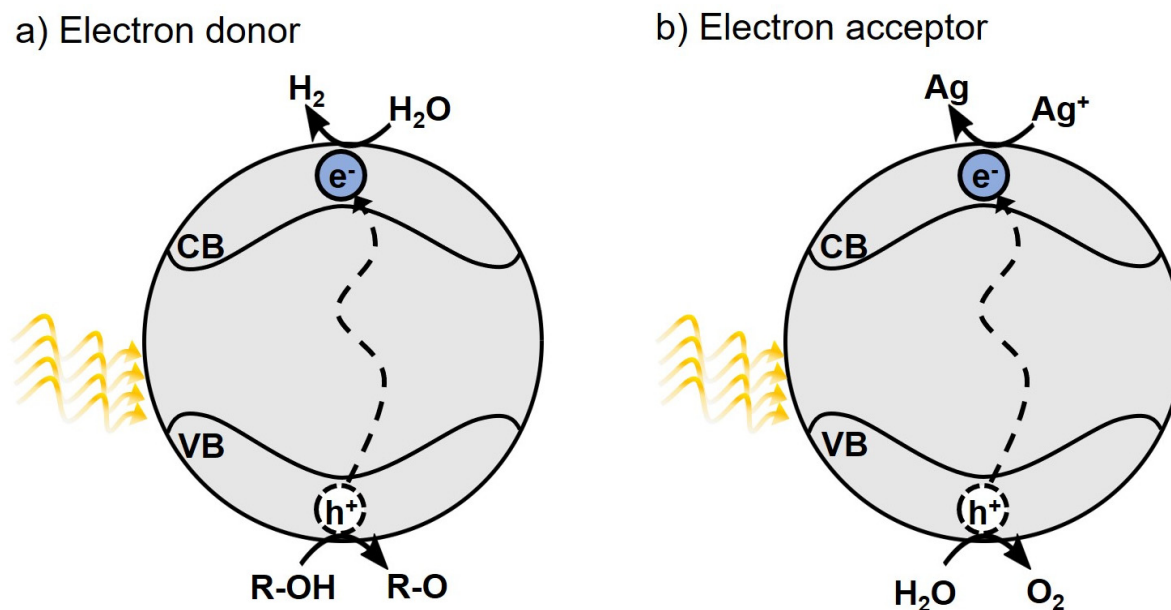


Figure 1.8. Photocatalyst in the presence of **a)** electron donor (e.g. methanol), and **b)** electron acceptor (i.e. silver nitrate).

1.2.3 Photocatalytic landmarks

Since the discovery of photocatalytic water splitting with TiO_2 electrodes by Fujishima and Honda [43], great advances have been made in the field of heterogeneous photocatalysis. Only a few years after the pioneering work by Fujishima and Honda, Inoue *et al.* reported the photocatalytic reduction of CO_2 . Photoreduction of CO_2 was studied under UV light and an external voltage was applied to several semiconductor electrodes to form methanol and formaldehyde [44]. Their work was followed by Bard's, who in 1979-80s proposed the internal electron-hole separations on heterogeneous materials after exposure to light, establishing the mechanistic principles of photocatalysis as known to date [45, 46].

TiO_2 has been the most investigated photocatalyst material, even though pure TiO_2 shows very poor activity for the photocatalytic water splitting [47]. Modified- TiO_2 systems were usually reported since co-catalyst(s) are used to enhance photocatalytic efficiencies by electron trapping or donation in the semiconductor, as discussed in [section 1.2.2.1](#). Together with TiO_2 , Pt was often reported as co-catalyst, since its addition was found to be effective on different combinations with TiO_2 -based photocatalysts [34]. Despite all, most of the reported photocatalytic reactions were

performed in the presence of sacrificial agents, otherwise yields were in the range of few $\mu\text{mol g}_{\text{cat}}^{-1} \text{h}^{-1}$ which is not suitable for practical applications.

The work of Domen *et al.* with NiO-SrTiO₃ brought some remarkable impacts over the photocatalytic performances (hundreds of $\mu\text{mol g}_{\text{cat}}^{-1} \text{h}^{-1}$) [48, 49]. In the meantime, photocatalytic advances were also achieved on the CO₂ reduction. Anpo's work on photoreduction of CO₂ using Ti-modified zeolites and pure TiO₂ yielded methanol and methane, respectively, leading to new discussions about the implication of other catalytic processes, rather than photocatalytic ones, taking place at the materials surface with light [50].

Many other types of Nb-, Ta-, W- and Mo-based materials have also been reported for the photocatalytic water splitting [34], even though TiO₂ was preferred due to its low price and tunability with metal particles, sensitizer molecules, or other semiconductor materials [28]. However, utilization of wide-bandgap materials restricted photocatalytic applications to the UV region, thus sunlight absorption efficiencies were low. Photocatalytic direction towards visible light was achieved by Domen, Maeda and co-workers who reported the well-known GaN:ZnO with enhanced water splitting activity by doping with Rh-Cr oxide [37, 39]; this work was one of the first combining Rh and Cr metals as promoters.

Later, Rh-Cr co-catalyst was used by Sakata *et al.* on a new class of wide-bandgap oxides, Ga₂O₃, and despite its wide-bandgap, high activities were found under UV light (in the range of $\text{mmol g}_{\text{cat}}^{-1} \text{h}^{-1}$) [51, 52]. Due to the appropriate properties of Ga₂O₃, highly porous gallium oxide materials were also evaluated for CO₂ photoreduction reaction leading mainly to CO and CH₄ formation [53], leaving the door open for another type of metal oxide that could potentially replace TiO₂.

In the last 10 years, with the aim to optimize reactors design for enhancing photocatalytic performances, several support materials (glass or fibers) have been investigated to immobilize semiconductors and improve their dispersion. In this regard and with graphene oxide becoming a hot topic, the works of Kamat and Teoh are highlighted since reduced graphene oxide (rGO) was used as a mediator for electron transport of semiconductors with potential applications with Vis-light [54-56].

Chapter 1

The works summarized in this chapter are only a few relevant contributions in the photocatalytic field. Considerable developments on photocatalytic materials and engineering of new reactor systems for photocatalytic processes have been carried out in the last decades. Nevertheless, this field is still far from commercial applications. Optimization of light absorption and clear understanding of the involved processes at the semiconductor surface under irradiation are required. Future investigations should also target the separation of gaseous products to improve efficiencies by avoiding back reactions and get closer to real applications.

1.3 Aim and overview of the thesis

The work presented in this thesis is focused on understanding the role of co-catalysts in the production of H₂ and O₂ from water splitting reaction as well as to produce chemical fuels (e.g. CH₄) from CO₂ photoreduction reaction. Wide-bandgap metal oxides, namely Ga₂O₃ and TiO₂, were employed as photocatalysts with Zn, Rh-Cr, Pt and Co as main co-catalysts. The given photocatalysts were characterized by X-ray absorption and emission spectroscopies to identify changes in physical properties of semiconductor after metal loadings. Photocatalytic reaction was studied *in situ* by infrared spectroscopy to propose a reaction mechanism based on the promoter effects. Furthermore, reduction and oxidation reactions were analysed electrochemically to understand the reaction kinetics and semiconductor properties decoupled from the co-catalyst functions.

[Chapter 2](#) describes the semiconductor materials (Ga₂O₃ and TiO₂) and impregnation method used to modify the photocatalysts. Photocatalytic H₂O splitting and CO₂ reduction reactions setups were optimized for this research work to evaluate both reactions under continuous flow conditions, in liquid-phase as well as in gas-phase. Additionally, basics on spectroscopic methods and data processing tools are described, and some fundamental notions on the electrochemical techniques used are properly introduced.

[Chapter 3](#) highlights the water splitting activity of Ga₂O₃ that was evaluated by the addition of Zn and Rh-Cr co-catalysts. Insights on the occupied and unoccupied electronic states of Zn and Ga were elucidated by X-ray absorption and emission

spectroscopic methods. Additionally, the function of Rh-Cr as electron sink and reduction site was proven by photocatalytic experiments using an electron acceptor (Ag^+) and by learning where Ag was deposited and its effects on the photocatalytic activity. Finally, perturbation of Zn electronic structure by photo activation was studied by modulation excitation X-ray absorption spectroscopy. Importantly, Rh-Cr markedly enhanced the level of the perturbation, serving as a proof of direct communication and synergy between the electronic states of Zn and Rh-Cr deposited on Ga_2O_3 .

Chapter 4 focuses on the study of CO_2 photoreduction reaction for TiO_2 -based materials with Pt and Co promoters. Intermediate species evolved from CO_2 (water saturated) under UV irradiation were studied *in situ* by diffuse reflectance infrared Fourier transformed spectroscopy (DRIFTS) and multivariate curve resolution (MCR) analysis. Photocatalytic and DRIFTS results showed different reaction mechanisms for Pt/ TiO_2 , Co/ TiO_2 , and TiO_2 materials. Formate surface species were identified as common intermediate among the three photocatalysts, although the promoters have influence on the product selectivity in CO_2 reduction. In addition, photocatalytic deactivation could also be attributed to the formation of carbonates blocking the TiO_2 surface active sites. Carbonate species were removed by addition of methanol vapour, thus photocatalyst surface could be regenerated after reaction under UV light.

Chapter 5 describes electrochemical and photo-electrochemical methods for studying redox reactions of TiO_2 -based materials. Co-catalysts were decoupled from TiO_2 and investigated on rGO. Hydrogen evolution reaction (HER) was enhanced with Pt, whereas H_2 barely formed in the presence of Co and sacrificial agents in solution are required (i.e. ethanol). On the other hand, O_2 from water splitting was not detected for Pt/ TiO_2 and Co/ TiO_2 ; even though AgNO_3 was used as electron acceptor, very low concentration of O_2 evolved for Co/ TiO_2 and none for Pt/ TiO_2 . Oxygen evolution reaction (OER) studies of metals/rGO unravelled that Pt and Co are capable of water oxidation, but an intermediate species is formed instead of oxygen. Nevertheless, water oxidation was achieved when co-catalysts were coupled to TiO_2 and the semi-reaction was studied by coupling photo and electrochemical methods, thus indicating the synergy between co-catalyst and semiconductor in the overall photocatalytic water splitting.

Chapter 1

Chapter 6 presents the thesis concluding remarks and a brief outlook on cell design combining DRIFTS, UV-vis light, and electrochemical methods to study *in situ* redox reactions at the electrodes surface for CO₂ photoreduction reaction.

Bibliography

1. Roser, M. and E. Ortiz-Ospina. *World Population Growth*. 2018.
2. Olah, G.A. *Angewandte Chemie International Edition*, 2005. **44**(18): p. 2636-2639.
3. (IEA), I.E.A. *Key world energy statistics*. 2017; Available from: <https://www.iea.org/>.
4. NASA's. *Global Climate Change Vital Signs of the Planet*. 2018 May 15, 2018; Available from: <https://climate.nasa.gov/>.
5. Nanaki, E.A. and G.A. Xydis, *Deployment of Renewable Energy Systems: Barriers, Challenges, and Opportunities*, in *Advances in Renewable Energies and Power Technologies*. 2018, Elsevier. p. 207-229.
6. Hussain, A., S.M. Arif, and M. Aslam. *Renewable and Sustainable Energy Reviews*, 2017. **71**: p. 12-28.
7. Olah, G.A., G.K.S. Prakash, and A. Goepfert. *Journal of the American Chemical Society*, 2011. **133**(33): p. 12881-12898.
8. Olah, G.A., A. Goepfert, and G.K.S. Prakash. *The Journal of Organic Chemistry*, 2009. **74**(2): p. 487-498.
9. Breeze, P., *Renewable Energy Combined Heat and Power*. 2018. 77-83.
10. Rühle, S. *Solar Energy*, 2016. **130**: p. 139-147.
11. Hernandez-Alonso, M.D., et al. *Energy & Environmental Science*, 2009. **2**(12): p. 1231-1257.
12. Lewis, N.S. and D.G. Nocera. *Proceedings of the National Academy of Sciences*, 2006. **103**(43): p. 15729.
13. Maeda, K. and K. Domen. *The Journal of Physical Chemistry Letters*, 2010. **1**(18): p. 2655-2661.
14. Habisreutinger Severin, N., L. Schmidt-Mende, and K. Stolarczyk Jacek. *Angewandte Chemie International Edition*, 2013. **52**(29): p. 7372-7408.
15. Takeda, H., et al. *Journal of the American Chemical Society*, 2008. **130**(6): p. 2023-2031.
16. Benson, E.E., et al. *Chemical Society Reviews*, 2009. **38**(1): p. 89-99.
17. Olivo, A., et al. *Energies*, 2017. **10**(9).
18. Neatu, S., A.J. Maciá-Agulló, and H. Garcia. *International Journal of Molecular Sciences*, 2014. **15**(4).
19. Wang, W., et al. *Chemical Society Reviews*, 2011. **40**(7): p. 3703-3727.
20. Hodes, G. *The Journal of Physical Chemistry Letters*, 2012. **3**(9): p. 1208-1213.
21. Wei, D. and G. Amaratunga. *International Journal of electrochemical science*, 2007. **2**: p. 897-912.
22. Dhakshinamoorthy, A., et al. *Energy & Environmental Science*, 2012. **5**(11): p. 9217-9233.
23. Hernández-Ramírez, A. and I. Medina-Ramírez, *Semiconducting Materials, in Photocatalytic Semiconductors: Synthesis, Characterization, and Environmental Applications*. 2015, Springer International Publishing: Cham. p. 1-40.
24. Osterloh, F.E. *Chemistry of Materials*, 2008. **20**(1): p. 35-54.
25. Matsumoto, Y. *Journal of Solid State Chemistry*, 1996. **126**(2): p. 227-234.
26. Kudo, A. and Y. Miseki. *Chemical Society Reviews*, 2009. **38**(1): p. 253-278.
27. Liu, G., et al. *Journal of Materials Chemistry*, 2010. **20**(5): p. 831-843.

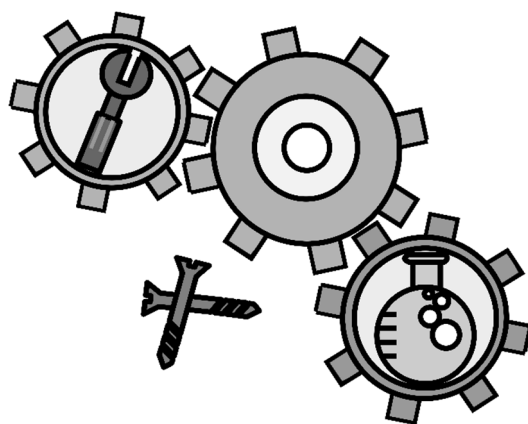
Chapter 1

28. Linsebigler, A.L., G. Lu, and J.T. Yates. *Chemical Reviews*, 1995. **95**(3): p. 735-758.
29. Disdier, J., J.-M. Herrmann, and P. Pichat. *Journal of the Chemical Society, Faraday Transactions 1: Physical Chemistry in Condensed Phases*, 1983. **79**(3): p. 651-660.
30. Shimura, K., T. Yoshida, and H. Yoshida. *The Journal of Physical Chemistry C*, 2010. **114**(26): p. 11466-11474.
31. Herrmann, J.-M. and P. Pichat. *Journal of Catalysis*, 1982. **78**(2): p. 425-435.
32. Courbon, H., J.M. Herrmann, and P. Pichat. *The Journal of Physical Chemistry*, 1984. **88**(22): p. 5210-5214.
33. Park, H., et al. *Journal of Photochemistry and Photobiology C: Photochemistry Reviews*, 2013. **15**: p. 1-20.
34. Chen, X., et al. *Chemical Reviews*, 2010. **110**(11): p. 6503-6570.
35. Kowalska, E., et al. *Physical Chemistry Chemical Physics*, 2010. **12**(10): p. 2344-2355.
36. Yanagida, T., Y. Sakata, and H. Imamura. *Chemistry Letters*, 2004. **33**(6): p. 726-727.
37. Maeda, K., et al. *The Journal of Physical Chemistry B*, 2006. **110**(26): p. 13107-13112.
38. Ma, B., et al. *The Journal of Physical Chemistry C*, 2010. **114**(29): p. 12818-12822.
39. Maeda, K., et al. *Angewandte Chemie International Edition*, 2006. **45**(46): p. 7806-7809.
40. Maeda, K., et al. *Nature*, 2006. **440**: p. 295.
41. Maeda, K., et al. *The Journal of Physical Chemistry C*, 2008. **112**(9): p. 3447-3452.
42. Ohtani, B., et al. *Journal of Photochemistry and Photobiology A: Chemistry*, 1992. **64**(2): p. 223-230.
43. Fujishima, A. and K. Honda. *Nature*, 1972. **238**: p. 37.
44. Inoue, T., et al. *Nature*, 1979. **277**: p. 637.
45. Bard, A.J. *Journal of Photochemistry*, 1979. **10**(1): p. 59-75.
46. Bard, A.J. *Science*, 1980. **207**(4427): p. 139.
47. Chae, J., et al. *Bulletin of the Korean Chemical Society*, 2009. **30**: p. 302-308.
48. Domen, K., A. Kudo, and T. Onishi. *Journal of Catalysis*, 1986. **102**(1): p. 92-98.
49. Domen, K., et al. *Journal of the Chemical Society, Chemical Communications*, 1980(12): p. 543-544.
50. Anpo, M., et al. *Catalysis Today*, 1998. **44**(1): p. 327-332.
51. Sakata, Y., et al. *ChemSusChem*, 2010. **4**(2): p. 181-184.
52. Sakata, Y., et al. *Journal of Catalysis*, 2014. **310**: p. 45-50.
53. Park, H., et al. *Journal of Materials Chemistry*, 2012. **22**(12): p. 5304-5307.
54. Gong, X. and W.Y. Teoh. *Journal of Catalysis*, 2015. **332**: p. 101-111.
55. Teoh, W.Y., J.A. Scott, and R. Amal. *The Journal of Physical Chemistry Letters*, 2012. **3**(5): p. 629-639.
56. Kamat, P.V. *The Journal of Physical Chemistry Letters*, 2010. **1**(2): p. 520-527.

Chapter 1

2.

Materials and methods



2.1 Photocatalyst preparation

Optimization of catalyst materials to achieve high activity, reproducibility, and stability, at low cost is one of the major focuses of the chemical industry. Photocatalytic reactions are still emerging as alternative technologies; however, the use of metal complexes and tandem materials increases photocatalyst costs and complexity of reaction mechanisms. The photocatalytic materials used in the present work are simply based on commercial semiconductors, namely gallium oxide and titanium dioxide (Ga_2O_3 or TiO_2), which are metal oxides with wide-bandgap. In general, bare semiconductor materials have low photocatalytic efficiencies that can be enhanced by metal addition (known as co-catalyst or promoter) as described in [chap. 1, section 1.2.2](#). Chemical methods such as e.g. impregnation is used to deposit metal particles on photocatalysts in a simple and reproducible manner. The most common type of impregnation is known as wet impregnation and this methodology consists of adding an excess of solution containing the metal precursor to the semiconductor material [1]. Wet impregnation is employed to deposit low metal concentrations since the amount of metal loading is restricted from the limited number of adsorption sites at the material surface. Moreover, the amount and type of co-catalyst loading significantly influences the photocatalytic activity, agglomeration of metals at the semiconductor surface will block light adsorption and the activity will decrease, thus metal concentration needs to be initially optimized [2]. The distribution of the metal particles deposited by wet impregnation methodology are mostly non-uniform and located at the metal oxide outer layers which can be easily identified through microscopy analysis.

The impregnation protocol followed in this work has been slightly modified from the conventional one that uses a stirring step during the metal addition; instead, ultrasounds were used to homogeneously mix the metal precursor solution with the semiconductor material. In this way, a metal promoter suspension was added dropwise to the mixed oxide under manual stirring and then sonicated for 3 min; the mixing process was repeated three times. In the next step the mixture was dried at 353 K to remove the excess of water, and it was finally calcined under synthetic air atmosphere ([Figure 2.1](#)).

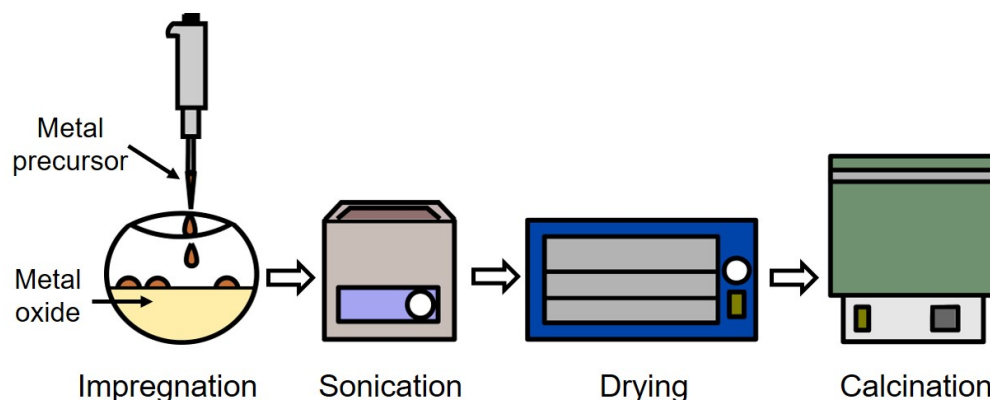


Figure 2.1. Impregnation method followed to deposit co-catalysts on Ga_2O_3 and TiO_2 materials.

2.1.1 Ga_2O_3 based materials

Gallium (III) oxide ($\geq 99.99\%$ trace metal basis, Sigma-Aldrich) was modified with Zn by impregnation method; typically, the raw material was calcined at 773 K for 3 h and then Zn was added. The $\beta\text{-Ga}_2\text{O}_3$ powder was then impregnated with an aqueous solution of $\text{Zn}(\text{NO}_3)_2 \cdot 6\text{H}_2\text{O}$ (99.999% trace metal basis, Sigma-Aldrich) and calcined at 1123 K for 6 h, the Zn loading was varied from 0 to 70 wt% (based on the weight of Zn with respect to that of Ga_2O_3). Zn-modified Ga_2O_3 was then impregnated with Rh (0.5 wt%) and Cr (0.75 wt%) with respect to that of Zn- Ga_2O_3 with an aqueous solution containing RhCl_3 and $\text{Cr}(\text{NO}_3)_3 \cdot 9\text{H}_2\text{O}$ precursors [3]. The as prepared materials were finally calcined at 623 K for 1 h. All the treatments were performed under a flow of synthetic air.

2.1.2 TiO_2 based materials

Titanium (IV) oxide (P25, Degussa) was calcined prior to addition of Pt and Co promoters at 423 K for 3 h. Pt and Co were deposited on TiO_2 by impregnation method. $\text{H}_2\text{PtCl}_6 \cdot 6\text{H}_2\text{O}$ (99.995%, Sigma Aldrich) was used as precursor for Pt modified TiO_2 (labelled as Pt/ TiO_2) synthesis, and $\text{Co}(\text{NO}_3)_2 \cdot 6\text{H}_2\text{O}$ (99.999%, Sigma Aldrich) for Co modified TiO_2 (as Co/ TiO_2); the metal loading is based on the weight of metal with respect to TiO_2 and is equal to 0.2 wt%. Finally, thermal treatment under synthetic air flow was performed at 623 K for 3 h for both materials.

Chapter 2

2.2 Reactor setup for continuous photocatalytic reactions

Photocatalytic reactions were carried out in a home-made setup and the system was configured depending on the process under investigation. Two photocatalytic reactions were examined, CO₂ reduction and water splitting. Water splitting reaction was evaluated in a liquid-phase reactor where the catalyst material was dispersed in water, and an inert gas was used to carry over the generated products to the analytical system (**Figure 2.2-a**) [4]. On the other hand, CO₂ reduction was performed in gas-phase i.e. the reactants (CO₂ and water vapour) were transported to the cell containing the solid powder catalyst (**Figure 2.2-b**); for this reason, a water saturator (maintained at constant temperature of 353 K) was added to the setup. In both cases, the gas flow (4.5 mL min⁻¹) was regulated with a mass flow controller (MFC), and a condenser was placed after the reactor to trap the water before reaching the analytical system consisting of a gas chromatograph (GC) and a mass spectrometer (MS) [5].

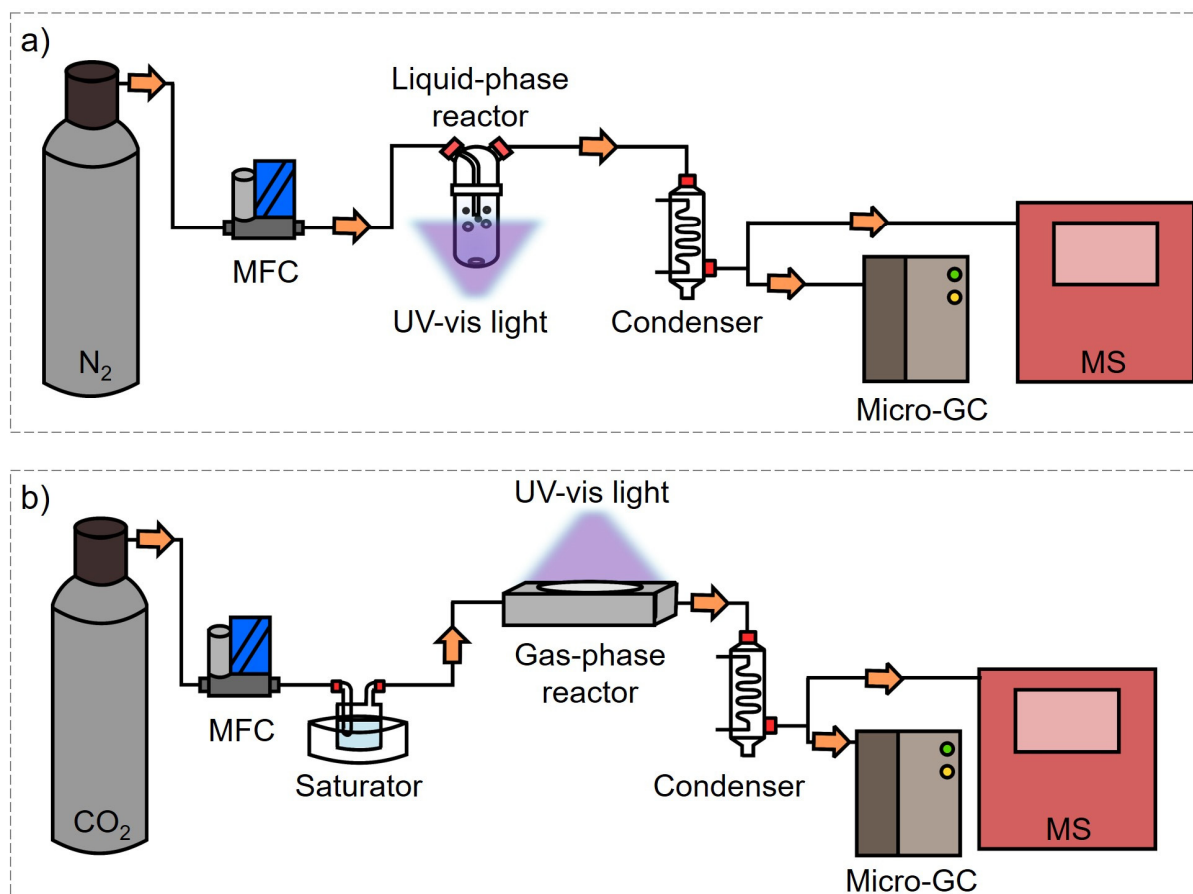


Figure 2.2. a) Liquid-phase and b) gas-phase reactor setups.

2.2.1 Slurry and gas phase reactors

Photocatalytic CO₂ reduction and water splitting reactions were evaluated under different conditions; therefore, distinct reactors were developed for liquid- and gas-phase reactions. The liquid-phase reactor (slurry reactor) consisted of a quartz cylinder transparent to UV with a glass head, gas inlet, and outlet joints (GL13 screw thread connectors) further connected to 1/8" tubing. Typically, 20 mg of photocatalyst (0.6 g L⁻¹) were dispersed in Milli-Q water (35 mL) in the ultrasound bath, and then the suspension was kept under stirring and continuous N₂ gas flow (4.5 mL min⁻¹) during the reaction. The reactor was sealed by means of high temperature resistance grease, and before starting the reactions the O₂ levels were monitored with the GC-MS and the measurements were started when the air was completely removed from the reactor. The light (400 W) was placed at 8 cm in front of the reactor to avoid excessive heat-up and water evaporation; in addition, the temperature inside the reactor was monitored (353 K) with a thermocouple inserted in the quartz tube (**Figure 2.3-a**).

On the other hand, gas-phase reactor consisted of an aluminium cell equipped with a fused silica window and the catalyst in powder form (100 mg) was deposited in the middle of the reactor on top of a quartz wool bed. Additionally, two heating cartridges connected to a power supply were used to keep the cell temperature constant at 423 K to enhanced the formation of carbon containing products [5], and it was also monitored with a thermocouple inserted in the cell below the catalyst bed. The sealing of the cell and the window was achieved by using silicone O-rings and several screws, and the window itself was placed between two additional O-rings to avoid breaking and leakage (**Figure 2.3-b**). The screws were always closed using the same force with a torque wrench at 5 N m⁻¹ which was tested to be the optimum force to avoid gas leakage. Moreover, inert gas had been flowed inside the cell to remove all the air before the experiment was started. The irradiation (400 W) was performed from the top part of the reactor and the light distance was also optimized to 8 cm.

Chapter 2

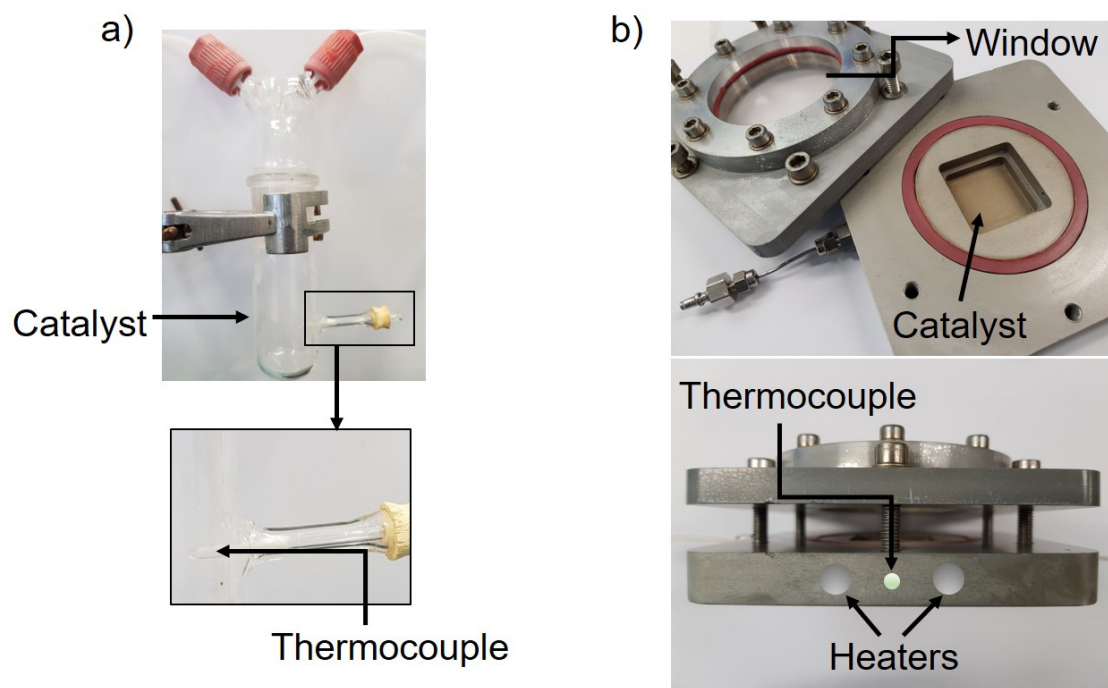


Figure 2.3. Temperature controlled **a)** quartz reactor and **b)** gas-phase cell.

2.2.2 Illumination sources

Light source is an essential element on a photocatalytic setup; although position and type of lamps are not often discussed in literature, without irradiation source reaction products will never be evolved since the photons from the light are required to trigger the chemical reactions. The selection of light source is a critical point when performing photocatalytic reactions; nowadays, there is a wide variety of illumination methods from solar simulators, LEDs, lasers, and gas discharge lamp sources. In this work, illumination sources in the UV spectral region were used since the photocatalysts have low or inexistent activity with visible light because semiconductors display wide-bandgaps (**Figure 2.4-a**). In particular, gas discharge lamps are used due to their higher efficiency and longer lifetimes when compared to incandescent and fluorescent lights. Photocatalytic experiments were performed with a high-pressure Hg custom lamp of 400 W (UV Technik) with a measured intensity of 1.27 mW cm^{-2} (**Figure 2.4-b**); high pressure bulbs were preferred to low pressure ones due to higher light intensity. Photocatalytic tests were performed without optical filters. Furthermore, infrared (IR) measurements were performed also in the UV-vis spectral range with an optical fibre-based light (UV-Consulting Peschl) to locally focus to the sample avoiding

the disturbance of the IR beam. The lamp has a power of 250 W and the specified intensity by the supplier of $<2 \text{ mW cm}^{-2}$ (Figure 2.4-c).

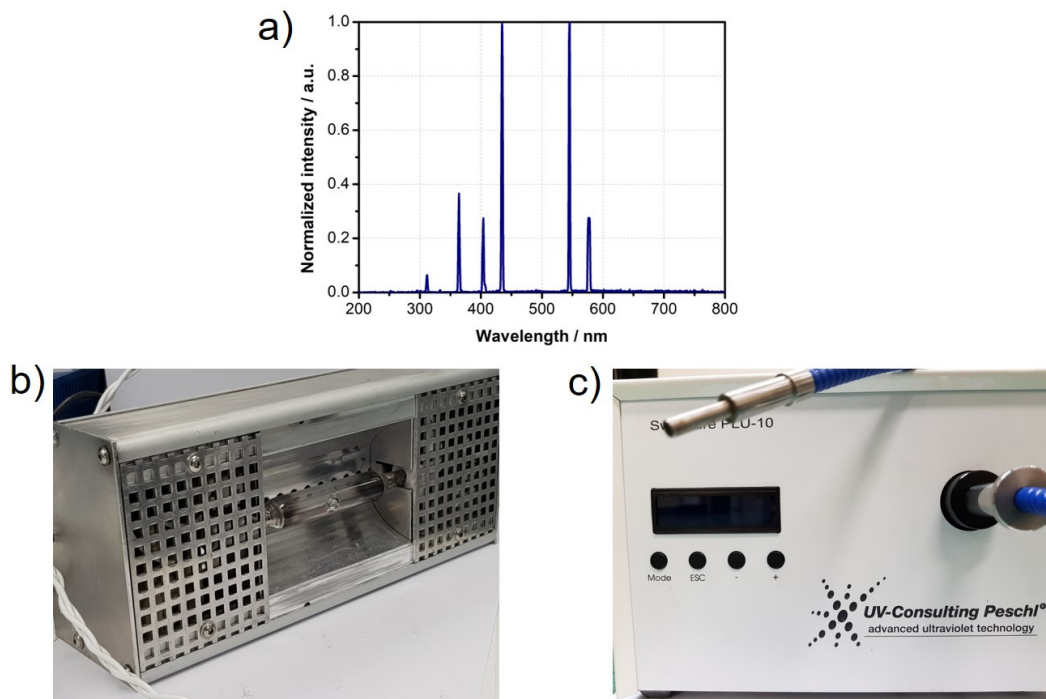


Figure 2.4. a) Light emission spectra (measured on the custom-made lamp). Pictures of the employed UV-vis lamps for b) high-pressure Hg light, and c) optical fibre-based light.

2.2.3 Analytical system

The products evolved from photocatalytic reactions were monitored online with a combined system composed of a mass spectrometer (MS, Pfeiffer Vacuum) and a gas chromatograph (Micro-GC, Agilent). The gas products concentration was quantified by the GC; Micro-GC was preferred due to the small quantity of sample (1-10 μL), and the rapid response compared to conventional GC instrument. The fast acquisition of chromatograms allows to obtain product concentrations in short times (minutes) [6]. Moreover, gas evolution was also continuously monitored by MS, therefore, if product concentration was below the GC detection limits ($<2 \text{ ppm}$) mass fragments were used to confirm any other unidentified products. Therefore, the gas composition (from MS) was converted to a concentration profile by correlating GC concentrations obtained at certain reaction times with the corresponding evolved fragments at the same time, as shown in Figure 2.5.

Chapter 2

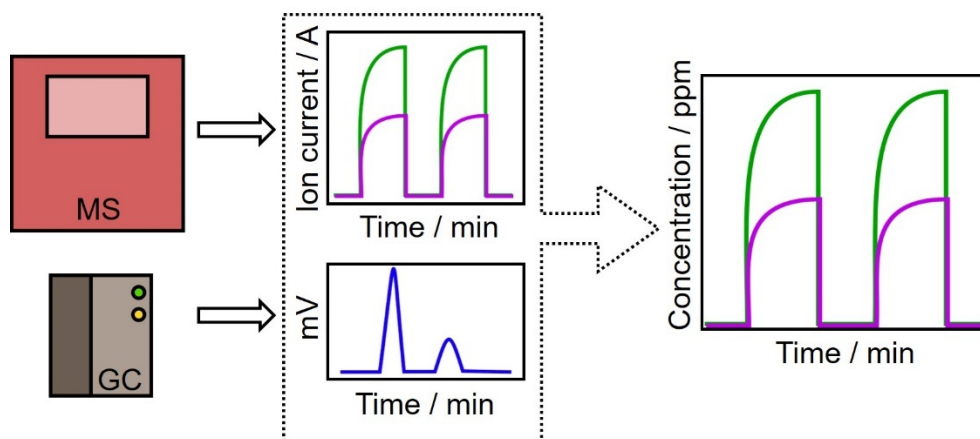


Figure 2.5. Online analytical gas analysis system composed by GC-MS (**left**). Typical MS profile obtained with light off/on experiments (**top**), and corresponding chromatogram acquired every 5 min (**bottom**). Resulting concentration profiles obtained from combining GC-MS data (**right**).

2.3 Spectroscopic techniques and processing tools

Investigation of the electronic properties of photocatalysts is fundamental to properly ascertain their catalytic behaviour. From the extensive number of existent characterization tools, spectroscopy offers the possibility of getting information about the crystal structure and chemical composition of materials. In the same way, the electric interactions within photocatalysts can be thoroughly analysed, i.e. bandgap is an important property to consider when working with semiconductors since their activity is strongly dependent on the efficiency of light absorption. The integral information expressed as bandgap is commonly gained by ultraviolet and visible diffuse reflectance spectroscopy; however, photocatalyst modified with low metal concentrations does not significantly affect the optical bandgap, thus X-ray absorption and emission spectroscopies alternatively show how the electronic structures in a material are influenced. Moreover, infrared experiments offer the possibility to study *in situ* chemical reactions occurring at the catalyst surface allowing a complete characterization of the chemical and physical processes affecting the photocatalytic activity.

2.3.1 Ultraviolet and visible diffuse reflectance spectroscopy

Ultraviolet-visible diffuse reflectance spectroscopy (UV-vis DRS) is a standard optical method to determine the absorption properties of solid materials. Typically, when incident light interacts with a powdered surface, this light is partially absorbed and partially scattered. The thickness of the material is an important parameter to consider when measuring in DRS, and it should be around 1-3 mm to efficiently absorb or scatter light [7]. UV-vis DRS is based on the light reflections in the ultraviolet and visible regions [8]. The spectrum is composed by light scattered from an infinite layer (i.e. sample) with respect to scattered light from a non-absorbing reference sample (e.g. barium sulfate) in function of the wavelength (λ) [9]. The scattered radiation is collected by an integrating sphere, using the following equation:

$$\frac{-dI}{\kappa\rho dS} = I - \frac{j}{\kappa} \quad (1)$$

where I is the incident light intensity; dI/dS the change of intensity with pathlength (dS); ρ is density of the medium; κ is attenuation coefficient due to the absorption and scattering; and j is the scattering function [9]. Kubelka-Munk (K-M) approximation is generally used to solve [Eq. \(1\)](#), where reflectance (R) is related to an apparent absorption (K) and scattering coefficient (S) as shown in [Eq. \(2\)](#):

$$KM = \frac{(1-R)^2}{2R} \quad (2)$$

For semiconductor materials, [Eq. \(2\)](#) is further multiplied by $h\nu$ to estimate their bandgap energy (E_g) which is the required energy to promote an electronic transition from the valence band to the conduction band [10]. Photons will be absorbed if their energy is greater or equal than the E_g , but if it is smaller than E_g photons will be scattered by the semiconductor material, thus bandgap can be estimated from the absorbance at a certain wavelength [10]. Usually, the linear part of the diffuse reflectance spectra is considered to calculate the bandgap energy as shown in [Figure 2.6](#), and then the onset energy (in nm) is converted to eV from the Planck-Einstein relation.

Chapter 2

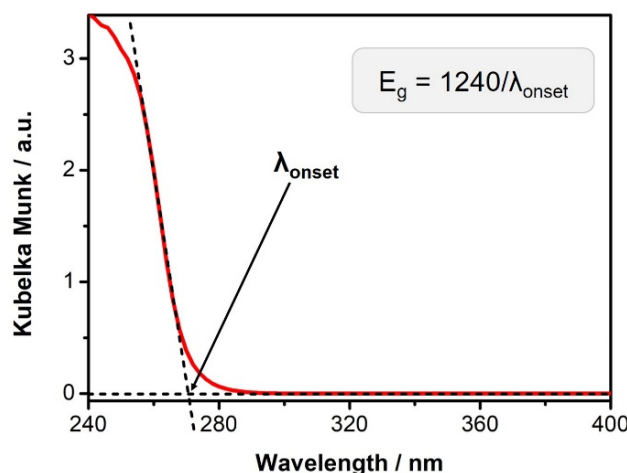


Figure 2.6. Bandgap estimation from the edge of Kubelka-Munk absorption spectra were 1240 eV·nm corresponds to the product of the Planck constant and speed of light from $E=(hc)/\lambda$.

UV-vis DRS measurements were performed on a Shimadzu UV-2401PC spectrophotometer with deuterium and halogen (D₂ and W) lamps as light sources, and a photomultiplier detector. Solid samples were introduced in a round holder with a fused silica window on an integrating sphere attachment ISR-240A (Shimadzu). BaSO₄ was used as internal standard and spectra were collected between 240 and 800 nm. Bandgap was calculated from the slope intersection of the normalized Kubelka-Munk absorption spectrum (**Figure 2.6**).

2.3.2 X-ray absorption and emission spectroscopies

Synchrotron radiation has become one of the very popular approaches within the scientific community due to its application to a wide range of characterization techniques, which offers the possibility of unravelling structural and electronic information of materials otherwise not possible with other conventional methods (e.g. UV-vis DRS). Synchrotron radiation is a powerful source of X-rays generated from high energy electrons moving in a circular path; this process is achieved when a sudden change in direction of the electrons that travel at very high velocities (almost the speed of light) occurs.

Among the available synchrotron techniques, X-ray absorption and emission spectroscopies (XAS and XES) provide unique information about the chemical nature and environment of the atoms in the materials. XAS and XES are element-specific

techniques, meaning that each element in the periodic table can be studied at its own binding energy required for a core electronic transition to occur [11]. Furthermore, amorphous materials can be studied by XAS and XES, a great advantage since not many characterization techniques can be used to study non-crystalline samples. XAS probes the transitions from the metal ground state to an excited state whereas XES measures the decay process from the excited state. X-ray absorption spectrum is divided in two regions (**Figure 2.7**); the X-ray absorption near-edge structure (XANES) where the transition from the metal core electronic state into an excited state occurs, and X-ray absorption fine structure (EXFAS) obtained at higher absorption energies when the electron is excited to higher state and can be released from the metal [12]. From XANES, chemical information about the electronic structure (valence) and symmetry of the metal (i.e. tetrahedral or octahedral geometry) is gained; and the types and distances between the metal and the neighbouring atoms can be gathered from EXAFS. Furthermore, XAS spectra can be acquired in transmission or fluorescence mode; usually, the last one is used on diluted samples with not enough photon absorption to be measured in transmission. Moreover, if high energy resolution is used to unravel little spectral details is called high-energy-resolution fluorescence detected (HERFD)-XAS [13].

Although X-ray absorption is an element selective technique very sensitive to the metal being studied it still presents some limitations when e.g. identifying elements of the similar atomic number (e.g. C or O). Consequently, to complement absorption studies the application of XES can be very advantageous when looking at the $K\beta$ fluorescent emissions (from orbitals at higher energy than 3p shell) gaining evidence on metal occupied states [14]. Emission spectrum is composed of fluorescence transitions; from 2p to 1s orbitals ($K\alpha$ lines) with the strongest spectral intensity, 3p to 1s ($K\beta$ lines) and higher than 3p shell to 1s ($K\beta$ satellite lines); the information gained from those lines is basically about the metal p density of occupied states [14]. From the scope of this work, we will only refer to the $K\beta$ satellite lines to discuss about valence to core emission transitions (**Figure 2.7**). $K\beta$ valence to core X-ray emission spectroscopy (VtC-XES) directly probes the valence orbitals of the metal under investigation. Also, two regions are found in the VtC-XES spectrum assigned to the valence bands (occupied states); transitions with s orbital contribution ($K\beta$ ” or “cross-

Chapter 2

over”), and with p orbitals ($K\beta_{2,5}$). The former also contains information about the chemical bond between the metal and neighbour atom and can be directly correlated to the EXAFS analysis [15].

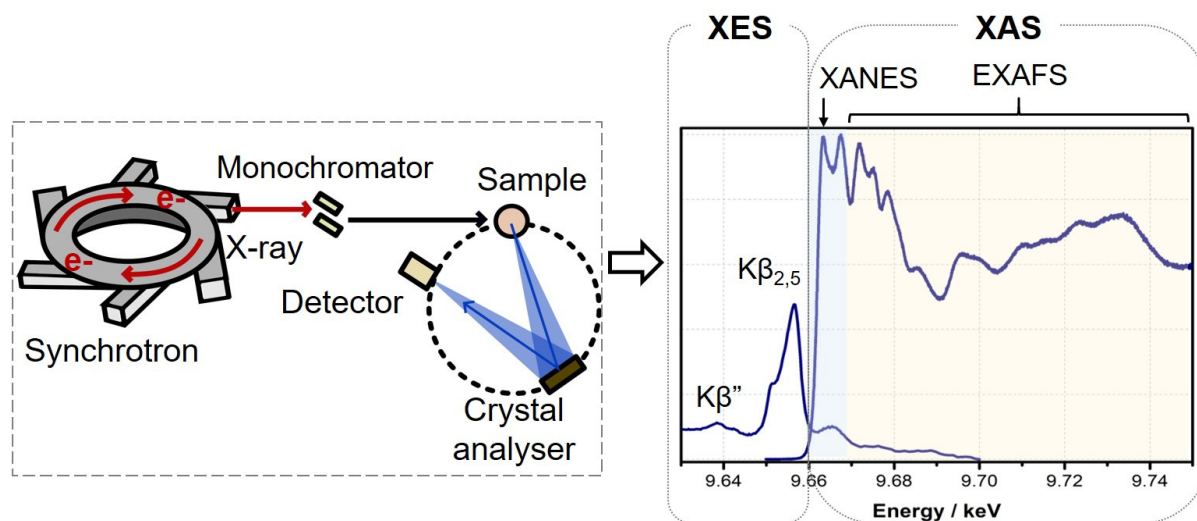


Figure 2.7. Synchrotron illustration for XAS-XES with crystals analyser, and combined XAS-XES spectra with noted regions for XANES and EXFAS (in blue and yellow colours) and $K\beta''$ and $K\beta_{2,5}$ for the VtC-XES spectrum.

XAS and VtC-XES measurements were performed at ID26 of the European Synchrotron Radiation Facility (ESRF) in Grenoble. The incoming energy was selected by the (111) reflection of a pair of cryogenically cooled Si crystals and the beam footprint on the sample was $1.0 \times 0.2 \text{ mm}^2$. Higher harmonics were suppressed by three Si mirrors working at 2.5 mrad. An emission spectrometer with four spherically bent ($r = 50 \text{ mm}$, $R = 1000 \text{ mm}$) analyser crystals in vertical Johann geometry was employed to select the $K\beta$ fluorescence lines of Cr, Zn and Ga using the reflections Ge (333), Si (555) and Ge (555), respectively, and a diode IF3 with Cu+Ni filter was used for Rh detection; other technical details of the beamline can be found at www.esrf.eu/UsersAndScience/EMD/ID26. HERFD-XANES were recorded on the maximum of the $K\beta_{1,3}$ line (9572.6 eV for Zn and 10265.37 eV for Ga) and by varying the incident energy from 10.36 to 10.46 keV (Ga), and 9.65 to 9.75 keV (Zn), in continuous scan mode. The spectra were not corrected for incident beam self-absorption (over-absorption) effects. Linear combination fitting was performed by using additional fitting parameters that account for the spectral distortion arising from self-absorption.

XES was measured for Ga, Zn and Cr K-edges at a fixed incident energy of 10.50, 9.80, and 6.10 keV, respectively. VtC-XES were acquired from 10.28 to 10.4 keV (Ga), 9.59 to 9.70 keV (Zn), and 5.96 to 6.02 keV (Cr) with a step size of 0.30 eV. All samples and reference materials were measured *ex situ* in the form of pellet (13 mm diameter), containing 60 mg of material and 60 mg of cellulose. For *in situ* irradiation experiments, pellets (13 mm diameter) containing 200 mg of pure material were transiently irradiated with DH-2000 (Ocean Optics) UV-vis-NIR deuterium-halogen light source while measuring 10 spectra under dark and then another 10 under light conditions. The light on-off cycles were repeated several times (120 s for each spectral acquisition), and the subtle differences of the spectral features were studied by modulation excitation methodology explained in [section 2.3.4](#). Athena was used to normalize the XANES spectra [16], and for all the samples E_0 was set individually to the corresponding maximum position of the first derivative. Linear combination fitting (LCF) was performed on the normalized XANES spectra and the corresponding standard materials were used for the fittings in the Zn and Ga energy ranges [17].

2.3.3 Diffuse reflectance infrared Fourier transformed spectroscopy

Infrared spectroscopy is a popular analytical tool for surface chemistry investigation of heterogenous materials assisting to gain better understanding on the catalytic processes. The infrared spectrum is obtained by absorption of IR radiation from the different functional groups present on the sample surface, which have assigned a specific frequency (e.g. catalyst containing adsorbed water shows IR bands belonging to the OH group, or upon CO₂ adsorption different type of surface carbonate, and/or bicarbonate species can be formed and identified from the stretching vibrations of CO regions). Also, IR is a powerful tool to follow *in situ* reactions since most of the IR cells have transparent windows e.g. CaF₂ [18]. Infrared can be measured in transmission mode where IR beam travels through the sample, thus requiring a sample preparation (pellet form) and IR transparent materials; or in reflection mode where the scattered light is measured, thus sample preparation is not required but an efficient optics to collect the light is needed. Infrared can also be

Chapter 2

measured in other modes such as attenuated total reflection (ATR) and reflection-absorption IR (IRRAS). ATR depends on the incident angle of IR beam that travels through a prism material with certain reflection angle that then penetrates into the material partially reflecting some light that is further analysed; despite the requirement of flat surfaces, the advantage of ATR is that can be used to measure adsorption of liquids in catalytic materials, whereas IRRAS is mainly used for analysis of film materials since high reflectivity and flat surfaces are required [19]. From the reflectance spectroscopy modes, diffuse-reflectance (DRIFTS) is the most convenient configuration for measuring rough surfaces and with this technique the intensity of IR bands is enhanced due to the multiple light reflections on the material surface [19]. Therefore, highly valuable information about the adsorbed species and the reaction intermediates can be gathered by performing DRIFTS under reaction conditions.

In situ DRIFTS experiments were performed in a FTIR-Vertex 70V instrument (Bruker) equipped with a Praying Mantis (Harrick), a HVC DRP (Harrick) cell, and a liquid nitrogen cooled detector (LN-MCT). The Praying Mantis accessory contained a HVC DRP cell and a combination of optical mirrors to collect and direct the light from the sample to the detector. The Harrick cell consisted of a sample holder at the centre, a gas inlet and outlet, a heating system, two windows IR transparent made of CaF_2 , and a third window of fused silica for the UV irradiation (**Figure 2.8**). The chamber is sealed with an O-ring and 4 screws, so experiments can run in a continuous gas flow through the cell. Additionally, a heating system coupled with a thermocouple allows the control of the catalyst temperature ensuring its stability during the experiment.

In a typical experiment, the cell temperature was set to 423 K under He flow (4.5 mL min^{-1}) for 1 h to clean the impurities and activate the materials. After temperature stabilization, the inlet gas was switched from He to CO_2 with water vapour (4.5 mL min^{-1}) for another 1 h (dark time) and then UV light was switched on (UV cycle). Illumination was performed with the optical fibre-based light already discussed in [section 2.2.2](#). The light off/on cycle was repeated twice (Dark1-UV1-Dark2-UV2) while acquiring spectra at each condition with OPUS software. Background spectrum was collected at the beginning of the experiment, the last spectrum of the He cycle,

for 200 scans. In total 5 cycles in He-Dark1-UV1-Dark2-UV2 were performed and IR was collected every min (72 scans per 5 spectra, 300 spectra in total).

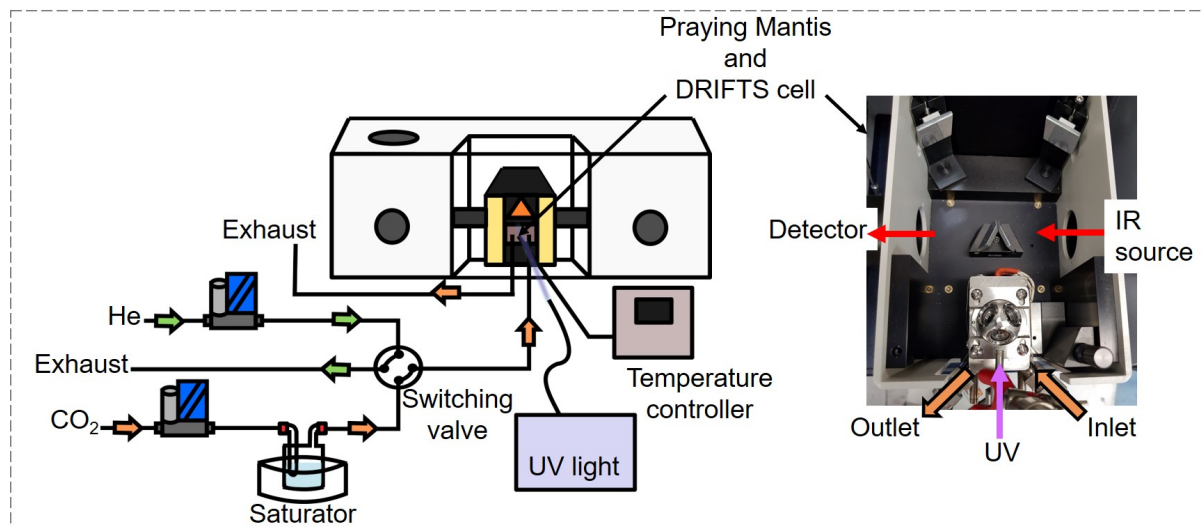


Figure 2.8. DRIFTS setup for CO₂ photoreduction reaction (**left**) and Praying Mantis accessory with the Harrick cell inside (**right**). The switching valve configuration allows to change the gas flow through the cell, and the UV-vis optical fibre was focused onto the photocatalyst powder.

2.3.4 Modulation excitation spectroscopy by phase-sensitive detection and multivariate curve resolution

The implementation of *in situ* spectroscopic techniques provides valuable information about catalytic active sites and surface intermediates under reaction conditions. However, the resulting datasets contain many spectra and are rather complex at a first glance; this results in a cumbersome analysis which challenges the correlation of the spectra with catalytic results. Besides the time-consuming analysis, the datasets also include species that are not directly involved in the reaction (also known as spectators). Furthermore, the signal intensity from the spectators and/or noise are usually stronger than the ones from the species of interest (active species) which might lead to the loss of spectral information and even a misinterpretation of the experimental data. In these cases, the application of modulation excitation spectroscopy (MES) to selectively detect the active species from the catalytic reaction is required. MES uses a periodic stimulation of the system which can be temperature, pH, concentration, or light, and after some time the response of the active species reaches a steady-state where it oscillates at the same frequency with the stimulation.

Chapter 2

Under this principle, light irradiation was considered as the external stimulation for the evaluation of the photocatalysts during *in situ* XAS and DRIFTS measurements.

The combination of MES with spectroscopy allows precise kinetic studies and sensitivity boosting of signals arising from transient processes [20-22]. Therefore, additional mathematical tools are required to process the generated datasets. In this work, phase-sensitive detection (PSD) and multivariate curve resolution (MCR) were applied for the X-ray spectroscopy and DRIFTS data processing, respectively. Two distinct mathematical engines were implemented because PSD method has difficulties in differentiating among overlapped bands which was required on the resulting data from DRIFTS measurements. In this case, MCR was used since is a blind source separation of the spectral components and standards are not required, as other processing methods such as linear combination analysis (LCA) [23].

Phase-sensitive detection (also called demodulation) principle relies on the periodic concentration perturbation (response $A(t)$) to a stimulation (here light on/off). Later, such response is averaged during the stimulation period (time-domain) and then transformed into phase-domain response $A_k(\phi_k^{\text{PSD}})$ using the equations showed in **Figure 2.9**. By transforming the time-domain into phase-domain response the spectator response and noise unaffected by the external perturbation are reduced to 0. From the equation parameters, demodulation index k was fixed to 1 since larger stimulation frequency (ω) is obtained, and demodulation phase angle (ϕ^{PSD}) to 0 for studying the ‘in phase’ angles which are yielded from the maximum amplitude [20-22].

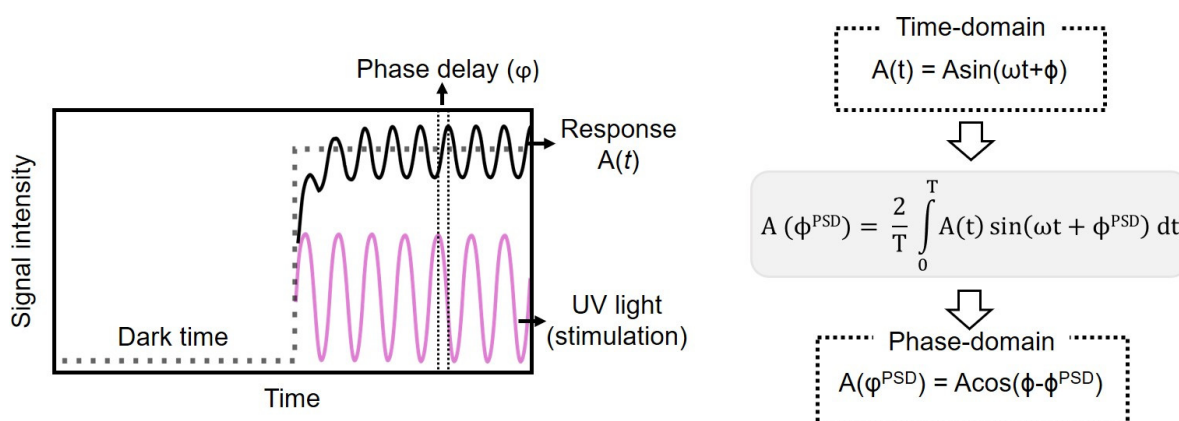


Figure 2.9. Effect of stimulation on the response of active species, and phase-sensitive detection equation for converting time-domain into phase-domain response.

DRIFTS data analysis was performed by MCR due to the complexity and overlapping of spectral bands. MCR is applied to the raw spectra matrix (D) which contains the spectra recorded in time, then the D matrix is decomposed into bilinear contributions of the pure components (columns matrix with concentration (C) and spectra profiles (S)) obtained by solving the equation $D = CS^T + E$ (Figure 2.10). Initially, the number of pure components needs to be defined, and then the alternating least square algorithm (ALS) is used to solve the MCR equation by several iterations until the best combination of C and S matrices is achieved [24]. This process should be repeated until the components with low noise are obtained [23, 25, 26]. Spectral components were normalized to the maximum value and the corresponding concentration profiles were scaled accordingly.

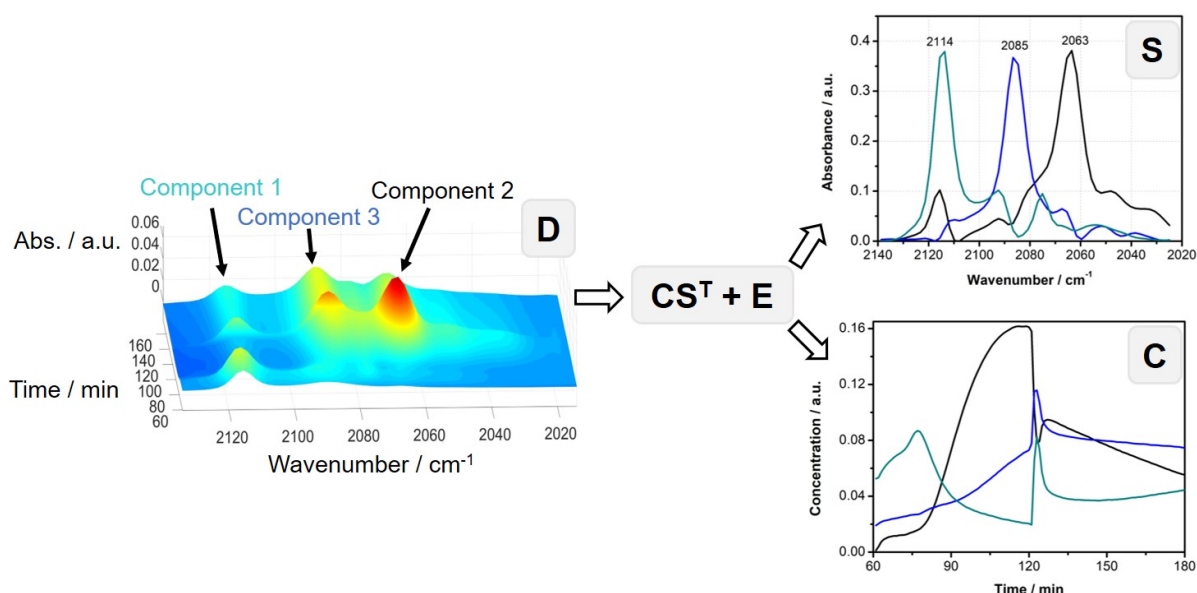


Figure 2.10. Multivariate curve resolution analysis from DRIFTS data (raw data matrix D containing absorbance spectra with time and wavenumber), and the spectral (S) and concentration components (C) obtained after performing MCR on D.

2.4 Electroanalytical methods

So far, application of spectroscopic methods for characterizing physicochemical properties of photocatalysts, and surface chemical species under *in situ* reaction conditions have been examined. Alternatively, electrochemistry, a powerful tool for the investigation of chemical processes involving electrons, is suitable to study photocatalytic reactions since we can mimic reduction and oxidation

Chapter 2

processes of adsorbed species at the photocatalyst surface by applying an external bias potential.

Typically, electroanalytical methods evaluate redox reactions in a three-electrode system which consists of a working electrode (composed by the material of study, usually a semiconductor), a reference electrode, a counter electrode, and an electrolyte solution (**Figure 2.11**). The working electrode (**1**), i.e. drop casted semiconductor on fluorine doped tin oxide (FTO), is in contact with the electrolyte solution and when applying certain potential electric current travels through the semiconductor-electrolyte junction until the Fermi level equals to the redox potentials of the electrolyte. Furthermore, the potential of the working electrode is controlled by a reference electrode (**2**) that has a known reduction potential (e.g. Ag/AgCl $E_{\text{red}}^0 = 0.199 \text{ V}$) [27]. Good reference electrodes require of a stable reduction potential with time, and there are three types of reference electrode: hydrogen, calomel, and glass electrode. Hydrogen (standard or normal) electrode is very stable but it contains Pt, similarly to the calomel electrode which contains Hg, thus can easily react with hydroxides to form metallic complexes [28], which makes it not suitable for certain applications. So, glass electrode such as Ag/AgCl is preferred. It has lower price than hydrogen electrode, but unlike normal electrodes, for comparison of measured potential (vs. Ag/AgCl) to the reversible hydrogen electrode (RHE), reference potential is calculated by using the Nernst equation:

$$E_{\text{RHE}} = E_{\text{Ag/AgCl}} + 0.059 \cdot \text{pH} + E_{\text{Ag/AgCl}}^0 \quad (3)$$

with known glass electrode reduction potential $E_{\text{Ag/AgCl}}^0 = 0.199 \text{ V}$ at 298 K. Usually, this type of electrodes are developed for aqueous electrolytes, however, there are other reference electrodes like Ag/AgNO₃ that can be used for organic electrolytes, thus a known redox process should be measured first (e.g. ferrocene reduction) to compare the measured potentials with the reference electrode [29]. Another element in three-electrodes setup is the counter electrode (**3**), usually a Pt wire, which acts as the current source supplying the same current as the working electrode. Finally, an important parameter of three-electrode configuration is the electrolyte solution (**4**) which is the media where ions move, and aspects such as diffusion and conductivity of electrolytes should be considered before running an experiment [28].

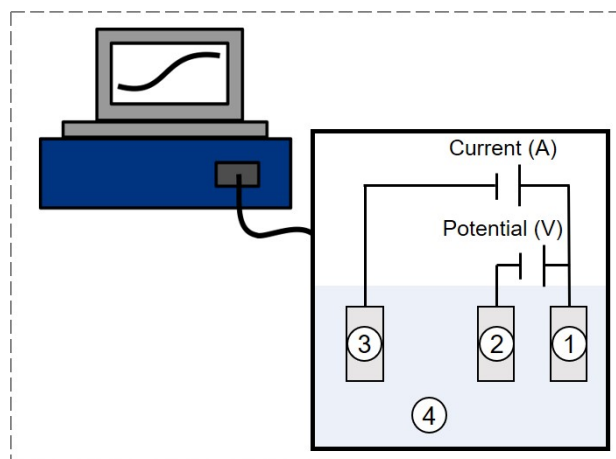


Figure 2.11. Three-electrode setup composed of working electrode (1), reference electrode (2), counter electrode (3), and electrolyte solution (4).

The voltage difference between 1 and 2 is controlled by a potentiostat (Figure 2.11), and the current flow between 1 and 3 is measured. Usually, the control parameter is the cell potential and the measured variable is cell current, thus potentiostat provides electronic hardware to run electroanalytical experiments.

From the available techniques for studying electrochemical reactions, the most used by non-electrochemists are potential sweeps which consist of applying potential that varies with time. Mechanistic insights of electrochemical reactions and kinetic parameters can be studied by performing potential sweeps which induce oxidation and reduction reactions at the working electrode. There are two forms of controlling the sweep, linear sweep voltammetry (LSV) and cyclic voltammetry (CV). The major difference between both techniques is the way that potential is scanned; for LSV potential scan is only performed in one direction (from an initial potential E_i to a final one E_f), whereas for CV once E_f is reached the potential scan goes back to E_i [28, 30]. In this work, we used linear sweep voltammetry because rotating disk electrode technique was applied for evaluating redox species as explained in the following section.

2.4.1 Rotating disk electrode and photoelectrochemical cell

Rotating disk electrode (RDE) is a type of convective electrode operated in three electrode configurations. RDE consists of a disk composed by a conductive material (i.e. glassy carbon) inside of an insulating material (RDE, Figure 2.12-b) that

Chapter 2

is attached to a motor which rotates at certain frequencies f (revolutions per second), usually, described as angular velocity (ω , s^{-1}) where $\omega = 2\pi f$. The material of study is carefully drop casted on the glassy carbon (RDE, **Figure 2.12-b** region **1**) by covering the disk surface to ensure a good contact between the conductive material and catalyst. Electrode rotation induces a flux from the electrolyte solution to the electrode surface; in this way, by changing the electrode velocity, kinetics of redox reactions can be evaluated [30].

The contact between a rotating electrode and electrolyte induces hydrodynamic and convective-diffusion phenomena, thereby equations are reported under steady-state conditions [31]. From solving convective-diffusion equations, Levich equation is obtained:

$$j = 0.62nFAD^{2/3}\omega^{1/2}\nu^{-1/6}C_o^* \quad (4)$$

where the current is function of Faradaic constant (96500 C mol^{-1}), A is the electrode area (cm^2), D is diffusion coefficient of gas in the solvent (i.e. electrolyte, $\text{cm}^2 \text{ s}^{-1}$), ν is viscosity of the solvent $\text{cm}^2 \text{ s}^{-1}$, and C_o concentration of target gas in the solvent (mol cm^{-3}). Experimentally, current generated by the electrode when performing LSV is measured at different frequencies (**Figure 2.12-a**). Then, the obtained current is converted to Levich current (j_m^{-1}) and can be represented at specific potentials (around the onset potential) at different rotational frequencies following the so-called Koutecky-Levich equation (**Figure 2.12-a**). Since current density (j_m) varies with $\omega^{1/2}$, deviation of a plot of j_m^{-1} vs. $\omega^{-1/2}$ from intersecting the origin suggests that there are kinetic limitations in the electron-transfer reaction [31]. j_k corresponds to the current without mass-transfer effects, i.e. when electron transfer is not a limiting factor. Moreover, from the slope calculated from statistical linear regression of j_m^{-1} vs. $\omega^{-1/2}$ plot (Levich constant, B in **Figure 2.12-a**) the number of electrons transferred (n) for the corresponding redox reactions can be obtained.

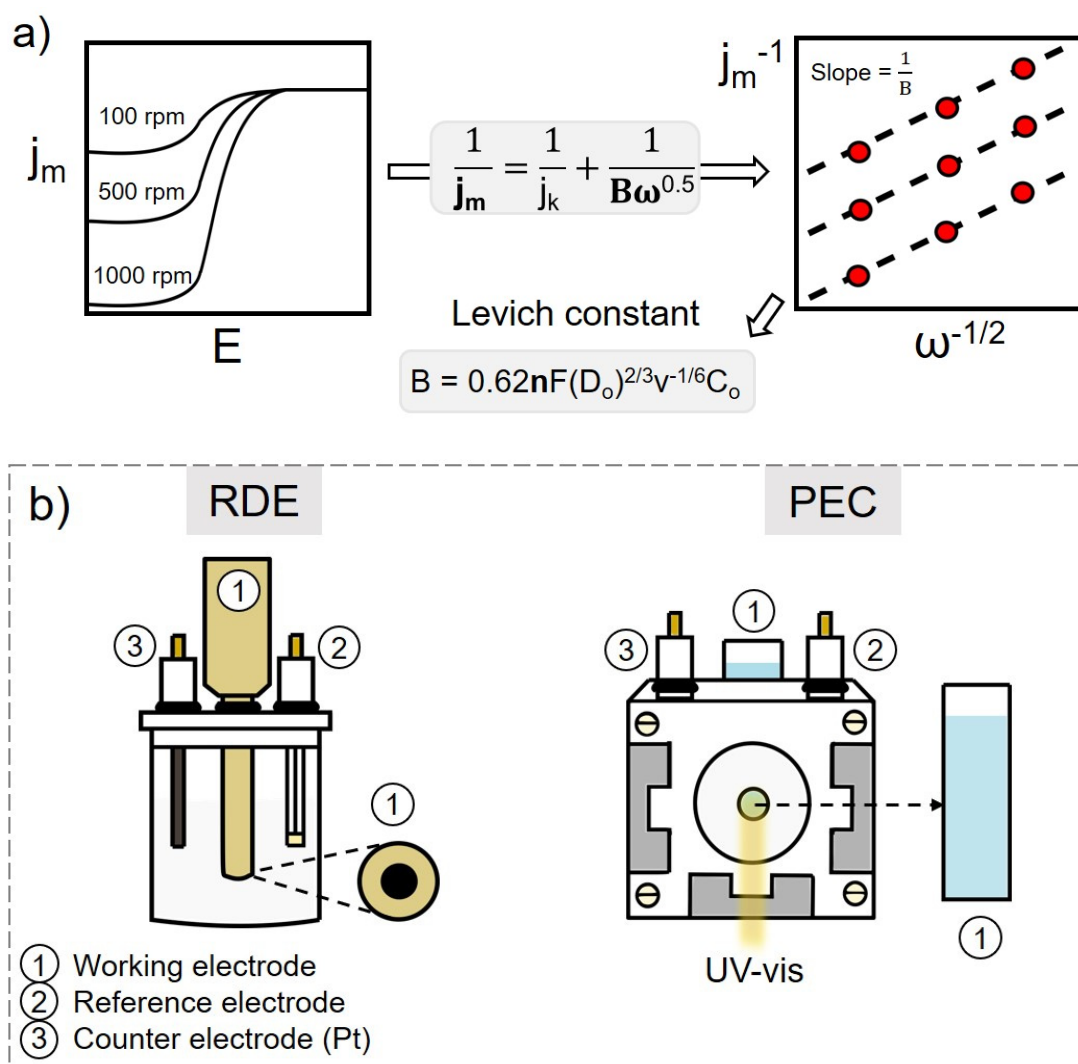


Figure 2.12. a) Calculation of the number of electrons involved in the redox reactions by using the Koutecky-Levich mathematical equation and after performing linear regression to the LSV data at several rotational speeds. b) Rotating disk and photoelectrochemical cells used to perform LSV, with working electrode (1), reference electrode (2), and counter electrode (3).

Measurements performed with photoelectrochemical cell (PEC) were also based on a three electrodes system (PEC, **Figure 2.12-b**). PEC is composed by the same elements as the ones used for RDE measurement. Contrastingly, working electrode (1) is not a carbon based one like for RDE, as it was composed of FTO coated glass with the photocatalyst material (TiO_2 based) deposited by drop casting to cover FTO surface. Prior to semiconductor deposition, FTO surface needs to be cleaned and calcined to avoid impurities that could affect the contact within the electrode surface and the material under investigation. Similar to RDE, we can study

Chapter 2

redox reactions, e.g. by comparing the onset potential position among several photocatalysts, and the efficiency of a semiconductor for oxidation or reduction [32]. Nevertheless, PEC configuration allows us to add an external parameter, namely UV-vis light. Thus, information on how light affects the electrode current density or redox efficiencies will provide additional insights on charge separation within the semiconductor material, as well as kinetic information regarding redox reactions.

Bibliography

1. Pinna, F. *Catalysis Today*, 1998. **41**(1): p. 129-137.
2. Fox, M.A. and M.T. Dulay. *Chemical Reviews*, 1993. **93**(1): p. 341-357.
3. Maeda, K., et al. *The Journal of Physical Chemistry B*, 2006. **110**(26): p. 13107-13112.
4. Bazzo, A. and A. Urakawa. *Catalysis Science & Technology*, 2016. **6**(12): p. 4243-4253.
5. Bazzo, A. and A. Urakawa. *ChemSusChem*, 2013. **6**(11): p. 2095-2102.
6. Kawamura, Y., S. Konishi, and M. Nishi. *Fusion Engineering and Design*, 2001. **58-59**: p. 389-394.
7. Murphy, A.B. *Solar Energy Materials and Solar Cells*, 2007. **91**(14): p. 1326-1337.
8. Gauglitz, G. and T. Vo-Dinh, *Handbook of Spectroscopy*. 2003, Germany: WILEY-VCH.
9. Weckhuysen, B.M. and R.A. Schoonheydt. *Catalysis Today*, 1999. **49**(4): p. 441-451.
10. López, R. and R. Gómez. *Journal of Sol-Gel Science and Technology*, 2012. **61**(1): p. 1-7.
11. Thompson A. C., et al. *X-ray Data Booklet*. 2001; Available from: <http://xdb.lbl.gov/>.
12. Yano, J. and V.K. Yachandra. *Photosynthesis Research*, 2009. **102**(2): p. 241.
13. Glatzel, P., et al. *Catalysis Today*, 2009. **145**(3): p. 294-299.
14. Glatzel, P. and U. Bergmann. *Coordination Chemistry Reviews*, 2005. **249**(1): p. 65-95.
15. Gallo, E. and P. Glatzel. *Advanced Materials*, 2014. **26**(46): p. 7730-7746.
16. Ravel, B. and M. Newville. *Journal of Synchrotron Radiation*, 2005. **12**(4): p. 537-541.
17. Ressler, T., et al. *Environmental Science & Technology*, 2000. **34**(6): p. 950-958.
18. Ryczkowski, J. *Catalysis Today*, 2001. **68**(4): p. 263-381.
19. Zaera, F. *Chemical Society Reviews*, 2014. **43**(22): p. 7624-7663.
20. Baurecht, D. and U.P. Fringeli. *Review of Scientific Instruments*, 2001. **72**(10): p. 3782-3792.
21. Urakawa, A., T. Bürgi, and A. Baiker. *Chemical Physics*, 2006. **324**(2): p. 653-658.
22. Urakawa, A., T. Bürgi, and A. Baiker. *Chemical Engineering Science*, 2008. **63**(20): p. 4902-4909.
23. Voronov, A., et al. *Analytica Chimica Acta*, 2014. **840**: p. 20-27.
24. Jaumot, J., A. de Juan, and R. Tauler. *Chemometrics and Intelligent Laboratory Systems*, 2015. **140**: p. 1-12.
25. Monakhova, Y.B., et al. *Chemometrics and Intelligent Laboratory Systems*, 2010. **103**(2): p. 108-115.
26. Monakhova, Y.B., et al. *Journal of Analytical Chemistry*, 2011. **66**(4): p. 351-362.
27. Grätzel, M. *Nature*, 2001. **414**: p. 338.
28. Brett, C. and O. Brett, *Electrochemistry, principles, methods and applications*. 1993, United States: Oxford University Press Inc.

Chapter 2

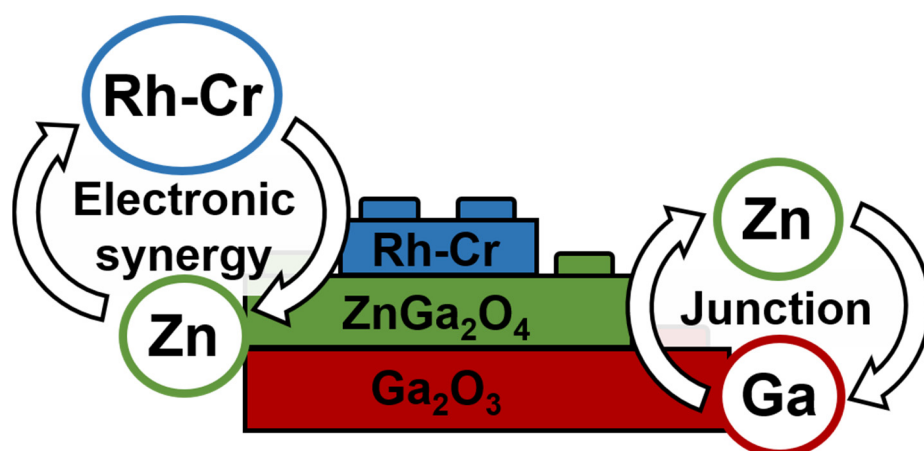
29. Pavlishchuk, V.V. and A.W. Addison. *Inorganica Chimica Acta*, 2000. **298**(1): p. 97-102.
30. Bard, A.J., *Electrochemical methods : fundamentals and applications* ed. L.R. Faulkner. 1980, New York: Wiley.
31. Bard, A.J. and L.R. Faulkner, *Electrochemical methods: fundamentals and applications*. Second edition ed. 2001, New York: John Wiley & Sons.
32. Maljusch, A., et al. *Electrochemistry Communications*, 2014. **38**: p. 142-145.

Chapter 2

3.

Electronic structure modifications of Ga_2O_3

Synergistic interplay of Zn and Rh-Cr promoters on Ga_2O_3 based photocatalysts for water splitting



3.1. Introduction

Photocatalytic water splitting has been extensively studied in recent years as a sustainable path to harvest sunlight to convert the energy contained in photons into the form of chemical energy such as hydrogen [1-3]. TiO_2 is the most widely investigated photocatalyst material because of its abundance, non-toxicity, and low cost [4]; however, the low H_2 productivity achieved by TiO_2 has motivated researchers to look for alternative semiconductor materials [5-7]. Among these, Ga_2O_3 exhibits excellent water splitting activity for pure water under UV-light due to its wide bandgap (4.6 eV) sufficient for the formation of hydrogen as well as oxygen [8]. Nevertheless, bare metal oxides generally lack the surface sites to efficiently activate the redox reactions and often show poor photocatalytic water splitting performance. The most common strategy to improve catalytic activity is the introduction of co-catalyst(s) to promote electron trapping ability near the catalyst surface, extending the life-time of electrons and holes generated upon light excitation and facilitating the redox reactions of adsorbed species at surface active sites of or near the co-catalyst (*chap. 1, section 1.2.2.1*) [9]. Noble metals such as Pt, Ru, and Rh [8], and combinations of metal oxides such as NiO [10], RuO_2 [11], and $\text{Rh}_{2-y}\text{Cr}_y\text{O}_3$ (or simply written as Rh-Cr) are commonly reported as effective co-catalysts when optimally loaded on photocatalysts [12]. Particularly for Ga-based oxide materials, rhodium and chromium mixed oxide was found to be greatly beneficial for overall water splitting, as demonstrated for the visible-light active $(\text{Ga}_{1-x}\text{Zn}_x)(\text{N}_{1-x}\text{O}_x)$ material [11, 13]. More recently, $\text{Rh}_{2-y}\text{Cr}_y\text{O}_3$ deposited on Zn-doped Ga_2O_3 was found to exhibit one of the highest water splitting activities reported to date (21.0 mmol of $\text{H}_2 \text{ h}^{-1}$ and 10.5 mmol $\text{O}_2 \text{ h}^{-1}$) under UV-light irradiation [14, 15].

Promotion of photocatalytic functions by co-catalyst(s) generally involves the formation of additional energy states that facilitate charge carriers (electron-hole) separation by electron trap or donation from the co-catalyst to the semiconductor material [16]. For the most active Rh-Cr and Zn co-doped Ga_2O_3 material, the function of Rh-Cr is generally explained as an electron sink whereas the role of Zn is not clear [17], although we have recently shown that the recombination of charges is greatly delayed by Zn promotion, thus enhancing the life-time of active redox sites and

consequently the photocatalytic activity [18]. However, the origin of the promotional effects and detailed insights into the electronic structure of the materials, particularly the synergistic functions of Rh-Cr and Zn co-promotion at an optimum loading of co-catalysts (especially Zn) [14, 17], are not known. Since the unique combination of the constituting elements of Rh-Cr/Zn-Ga₂O₃ catalyst affords outstanding photocatalytic performance in pure water splitting by a few orders of magnitude higher than those generally reported [14, 18], it is imperative to precisely understand the promotional and synergetic effects of Rh-Cr and Zn towards rational photocatalyst design for hydrogen production from water with sunlight.

Reflecting this background, herein, we uncovered the effects of Zn and Rh-Cr promotion through understanding their impacts on the electronic structure of Ga₂O₃-based photocatalysts. Element selective X-ray absorption and emission spectroscopies (XAS and XES) were employed to learn about the structures of unoccupied (related to conduction band) and occupied (related to valence band) electronic states of Zn and Ga within the catalyst materials, respectively [19, 20]. In contrast to the integral information expressed as the bandgap commonly measured by UV-vis diffuse reflectance spectroscopy (UV-vis DRS) [21, 22], the information from XAS-XES uniquely shows how the electronic structures of atoms in a material are altered and, together with additional structural insights gained by electron microscopy and X-ray diffraction, the exact functions of Zn-Ga heterojunction favourable for charge separation can be elucidated. On the other hand, the function of Rh-Cr as reduction and H₂-evolution site was verified by a control experiment using Ag⁺ as electron scavenger as well as by monitoring the change in the electronic structure of Cr by XAS. Finally, the direct involvement of Rh-Cr component on the charge separation in Zn element was evidenced by means of XAS combined with a modulation excitation technique [23], firmly explaining the electronic interactions of the two promoters and their concerted synergetic functions resulting in the drastic boost of the photocatalytic water splitting activity of Ga₂O₃.

3.2. Experimental

3.2.1 Materials

Zn-modified Ga₂O₃ catalysts were prepared by the impregnation method followed by a thermal treatment as explained in *chap. 2, section 2.1.1*. The loading of Zn was varied from 0 to 70 wt% (based on the weight of Zn with respect to that of Ga₂O₃), and then Rh-Cr was impregnated with the same loading (0.5 wt% of Rh and 0.75 wt% of Cr) for all the Zn-modified Ga₂O₃ samples [24].

3.2.2 Reaction setup

Photocatalytic activity measurements were performed at room temperature using the liquid-phase setup described in *chap. 2, section 2.2* [18]. In brief, the setup consisted of a quartz reactor connected to a gas supply. The reaction products were monitored by an online MS (Pfeiffer Vacuum, Omnistar GSD 320) and the product quantification was verified by a GC (Agilent Technologies, micro-GC 490). Powder catalyst (20 mg, 0.6 g L⁻¹) was dispersed in ultrapure water (35 mL, Milli-Q) and 0.01 M AgNO₃ aqueous solution was used for electron-trapped oxygen evolution studies. The suspension was kept under stirring and continuous N₂ gas flow (4.5 mL min⁻¹) during the reaction. The catalyst solution was purged with N₂ for 1 h prior to irradiation with a 400 W high-pressure Hg lamp (UV-Technik, without optical filter) at 8 cm distance from the reactor to avoid excessive heat-up and water evaporation. The Ga₂O₃-based materials are known to show photocatalytic activity with only UV light (<275 nm) and the test was performed without an optical filter [18]. The reactor temperature was monitored to be about 353 K during the reaction. Repeated light on/off cycles for 1.5 h each on/off phase were studied for overall water splitting reaction. For the evaluation of O₂ evolution reaction in the presence of silver nitrate, the catalyst in solution was continuously irradiated for 4 h.

3.2.3 Materials characterization

Powder X-ray diffraction (PXRD) were performed on a Bruker D8 Advance power diffractometer with a vertical 2theta-theta goniometer in transmission

configuration with Cu K α radiation ($\lambda=1.5406$ Å). Maud software was used to perform phase quantification of the synthesised materials [25]. Instrumental broadening was firstly corrected to perform Rietveld refinement and phase quantification.

XAS and valence-to-core (VtC)-XES measurements were performed at ID26 of the ESRF (details of the spectrometer configuration are found in [chap. 2, section 2.3.2](#)). HERFD-XANES were recorded on the maximum of K $\beta_{1,3}$ line and by varying the incident energy from 10.36 to 10.46 keV (Ga) and 9.56 to 9.75 keV (Zn) in continuous scan mode. XES was measured for Ga and Zn K-edges at a fixed incident energy of 10.50 and 9.80 keV, respectively. VtC-XES were acquired from 10.28 to 10.40 keV (Ga) and 9.59 to 9.70 keV (Zn) with a step size of 0.30 eV (further energy details discussed in [chap. 2, section 2.3.2](#)). Samples and reference materials were measured *ex situ* (in the form of pellet), and 4 wt% Zn-Ga₂O₃ and Rh-Cr/4 wt% Zn-Ga₂O₃ sample were measured *in situ* (under irradiation). Experiments with UV-vis illumination were performed measuring 10 spectra under dark and then under light conditions. Light on-off cycles were repeated 11 times for the material without Rh-Cr (220 spectra in total; 120 s for each spectral acquisition) and 7 times for the samples containing Rh-Cr (140 spectra in total), and the subtle differences of the spectral features were studied by modulation excitation methodology explained in the following section. Athena was used to normalize the XANES spectra [26], and for all the samples E_0 was set individually to the corresponding maximum position of the first derivative. Linear combination fitting (LCF) was performed on the normalized XANES spectra and two standards ZnO and ZnGa₂O₄ (Zn K-edge) and ZnGa₂O₄ and Ga₂O₃ (Ga K-edge) were used for the fitting in the range of 9.65-9.69 keV (Zn) and 10.36-10.40 keV (Ga) [27].

3.2.4 Modulation excitation spectroscopy (MES)

MES allows precise kinetic studies and sensitivity boosting of signals arising from transient processes [23, 28, 29]. In this study the latter advantage (typically 2-3 order of magnitude sensitivity boost) was exploited (further details in [chap. 2, section 2.3.4](#)). The mathematical core of MES is phase sensitive detection (PSD, also called demodulation) as shown in [Eq. \(1\)](#), which converts time-domain response $A(t)$ to a

phase-domain response $A_k(\varphi_k^{\text{PSD}})$ with almost full reduction of the static noise and signals unaffected by the external perturbation (here light on and off) [23, 28].

$$A_k(\varphi_k^{\text{PSD}}) = \frac{2}{T} \int_0^T A(t) \sin(k\omega t + \varphi_k^{\text{PSD}}) dt \quad (1)$$

The PSD analysis was performed at demodulation index $k = 1$.

3.3. Results and discussion

3.3.1 Photocatalytic activity of Zn-Ga₂O₃ and Rh-Cr/Zn-Ga₂O₃

First, effects of Zn-loading amount as well as addition of Rh-Cr promoters to Ga₂O₃ on photocatalytic water splitting activity were systematically studied. **Figure 3.1** compares the productivity of hydrogen and oxygen as a function of Zn-loading with/without addition of Rh-Cr co-catalyst. Bare Ga₂O₃, without Zn and Rh-Cr promoters, shows low H₂ productivity (0.16 mmol g_{cat}⁻¹ h⁻¹), although this productivity level is comparable to that of well-known Pt/TiO₂ photocatalyst (0.10 mmol g_{cat}⁻¹ h⁻¹) [30, 31]. At 2-4 wt% Zn-loading, the H₂ productivity was enhanced reaching 1.1 mmol g_{cat}⁻¹ h⁻¹. However, the H₂ productivity drops at higher Zn-loadings (>20 wt%), as similarly reported by Wang *et al.* who observed the drop in the activity from 3 to 4 Zn-atom% (which would correspond to 1.1-1.4 wt% of Zn of this study) [32]. Remarkably, the addition of Rh-Cr boosts the water splitting activity by almost one order of magnitude, while retaining the activity trends induced by the varying amount of Zn. The highest H₂ productivity of 9.0 mmol g_{cat}⁻¹ h⁻¹ observed for Rh-Cr/4 wt% Zn-Ga₂O₃ was more than the sum of the Rh-Cr effect (3.3 mmol g_{cat}⁻¹ h⁻¹) and the Zn-effect (1.1 mmol g_{cat}⁻¹ h⁻¹), confirming the previously observed synergistic effects of the Zn and Rh-Cr promoters [14, 18]. Stoichiometric production of H₂ and O₂ was not achieved with higher H₂/O₂ ratio possibly due to the formation of peroxo-species [31, 33], although we could not identify such species in the solution.

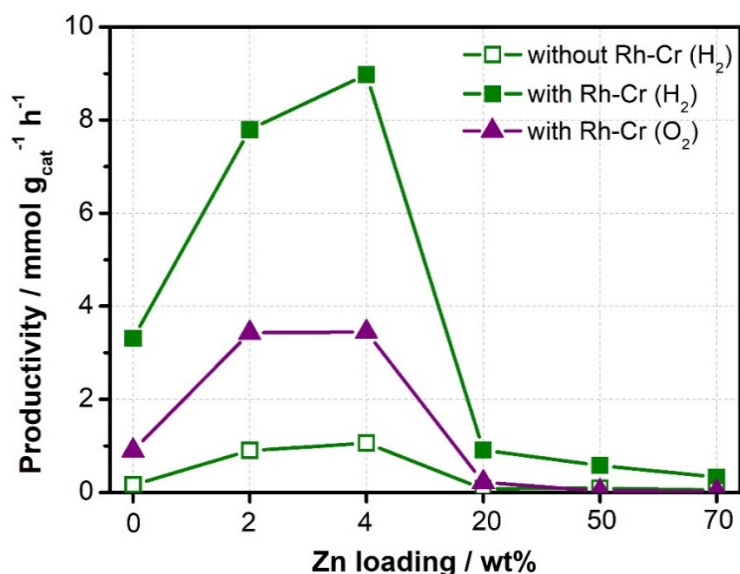


Figure 3.1. H₂ (green) and O₂ (purple) productivity in the photocatalytic water splitting reaction using pure water for $xZn-Ga_2O_3$ and $Rh-Cr/xZn-Ga_2O_3$ (where $x = 0, 2, 4, 20, 50,$ and 70 wt% of Zn). H₂/O₂ productivity was averaged from 4 runs by 1.5 h UV-vis irradiation cycles. O₂ productivity for the materials without Rh-Cr is not shown because of the low amount of O₂ (below the detection limit of the GC) for confident quantification.

3.3.2 Geometrical and electronic structure changes by Zn-loading

The structures of the Zn-promoted Ga_2O_3 materials without Rh-Cr co-catalyst are studied by XRD, XAS, and XES to elucidate the changes induced by the Zn addition. The effects of Rh-Cr co-catalyst on the structure of the catalyst materials are considered to be solely electronic ones due to the low loading of Rh-Cr, as observed from the negligible influence on the characterization results by the presence of Rh-Cr (not shown here).

PXRD results (**Figure 3.2-a**) show that the $Zn-Ga_2O_3$ materials are composed of $\beta-Ga_2O_3$ and $ZnGa_2O_4$ phases at low Zn concentrations (2-4 wt%) in accordance with literature [32], whereas in this work the presence of ZnO phase is also confirmed at high Zn-loading (≥ 20 wt%). The absence of the shifts of the $\beta-Ga_2O_3$ reflection peaks at all Zn-loadings indicates that Zn is not incorporated into the Ga_2O_3 lattice [34]. Electron microscopy and energy dispersive analysis indicate the presence of Zn elements near the material surface (*appx. A, Figure 7.1*). This suggests that $ZnGa_2O_4$ and ZnO are deposited on the surface of Ga_2O_3 as expected from the impregnation and subsequent calcination methods used to prepare the $Zn-Ga_2O_3$ materials.

Chapter 3

Quantitative phase analysis (*appx. A, Figure 7.2*) confirms that up to 4 wt% Zn-loading, Zn is present only as ZnGa_2O_4 , while the amounts of both ZnGa_2O_4 and ZnO, particularly the latter, increase as the Zn-loading increases. Analysis of the HERFD-XANES spectra at Zn K-edge and Ga K-edge by linear combination fitting (**Figure 3.2-b**) [27], together with Zn K-edge VtC-XES (*appx. A, Figure 7.3*) and Zn K-edge EXAFS (*appx. A, Figure 7.4*) point to the identical conclusion, clearly showing how the Zn elements in the materials are present, either solely as ZnGa_2O_4 (2, 4 wt% Zn) in the vicinity of the Ga atoms with the creation of additional electronic states in the valance bands, or as a mixture of ZnGa_2O_4 and ZnO (≥ 20 wt% Zn).

Furthermore, the integral electronic properties of Zn-modified Ga_2O_3 materials are studied by UV-vis DRS through their optical properties (*appx. A, Figure 7.5*). The optical bandgap of Ga_2O_3 is barely modified by the Zn addition (from 4.58 to 4.55 eV). Therefore, the catalytic activity trends at different Zn-loading (**Figure 3.1**) cannot be explained by the change in the bandgap. This is in accordance with the report by Wang *et al.* where Zn- Ga_2O_3 materials were studied for CO_2 reduction [34]. This also implies that the photon energy required to generate excitons (bound electron-hole pairs) is not strong enough to separate electrons and holes, which is required for photocatalytic reactions, and the functions and interface of different components of the photocatalyst facilitate the charge separation.

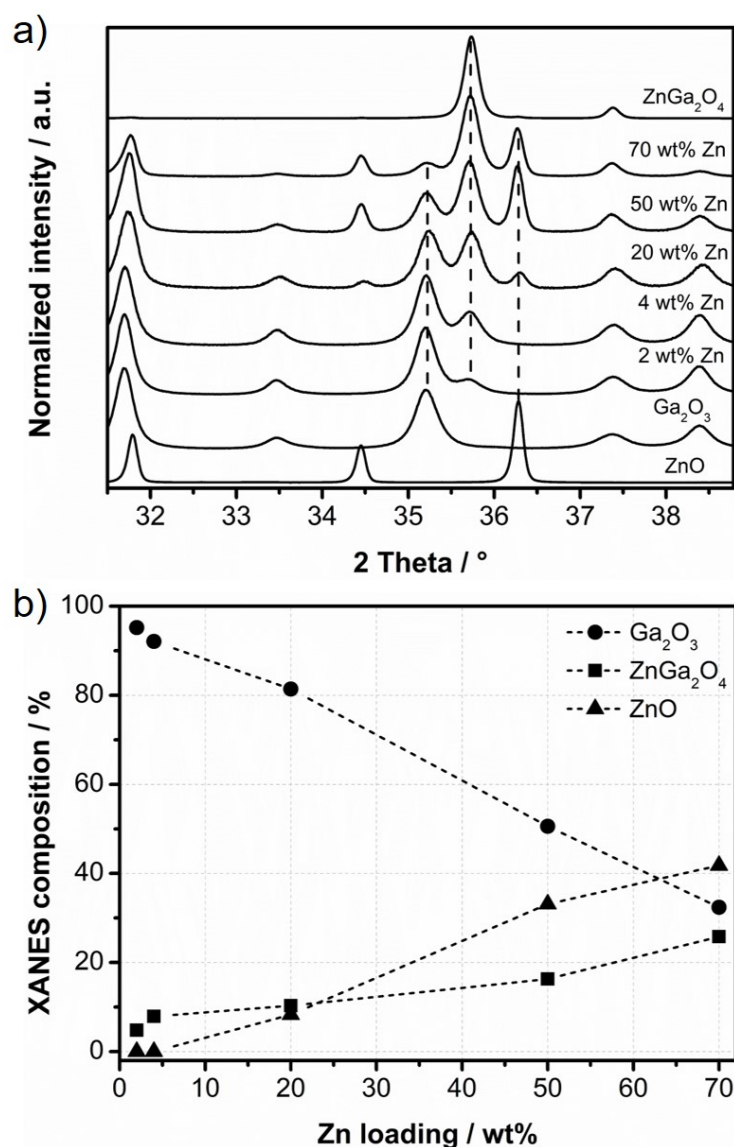


Figure 3.2. a) PXRD patterns for Zn-modified Ga_2O_3 materials, including reference materials ZnO, ZnGa_2O_4 , and Ga_2O_3 . The dotted lines indicate Ga_2O_3 (35.2°), ZnGa_2O_4 (35.7°), and ZnO (36.3°) phases. b) Linear combination fitting analysis of Zn and Ga K-edge XANES spectra using ZnGa_2O_4 and ZnO, and ZnGa_2O_4 and Ga_2O_3 as standards to perform the fitting, respectively.

To gain precise insights into the electronic structures of the Zn-promoted materials, XAS and VtC-XES were employed to study unoccupied and occupied energy states, respectively, of Zn and Ga atoms within the materials (*appx. A, Figure 7.6*) [35]. At both Zn K-edge (**Figure 3.3-a**) and Ga K-edge (**Figure 3.3-b**) the highest occupied energy level (VtC-XES results) are virtually unaltered among the reference materials. Nevertheless, it should be noted that electronic orbital mixing from s orbitals of the O atom and d orbitals of the Ga atom is observed at the VtC-XES $\text{K}\beta''$ line of

Chapter 3

ZnGa₂O₄ (inset in **Figure 3.3-a**; the electronic structure assignments based on DFT calculations are shown in *appx. A, Figure 7.3*), affirming electronic interaction and communication between Zn and Ga atoms in ZnGa₂O₄.

Clear differences are observed for the energy levels of unoccupied states at the Zn and Ga absorption edges. For the Zn K-edge, at small Zn concentrations (2 and 4 wt%) the lowest-unoccupied electronic states appear to be similar to those of ZnGa₂O₄ (*appx. A, Figure 7.6-a*). At increasing Zn-loading where ZnO phase is more prominent, the absorption edges shift to lower energies, corresponding to smaller valence-conduction bandgaps (3.1 eV for ZnO, calculated from the difference between the maximum of the 1st derivative of the emission spectrum and the absorption edge as shown in *appx. A, Figure 7.7*). The bandgap of ZnO derived from the XAS-XES analysis that reflects the Zn p-projected density of states agrees with that of the optical bandgap (3.2 eV) determined by UV-vis DRS. The small bandgap of ZnO (**Figure 3.3** and *appx. A, Figure 7.6*), its increasing light absorption at higher loading (*appx. A, Figure 7.5*) and the coexistence of ZnGa₂O₄ and Ga₂O₃ phases (**Figure 3.2-a**) suggest that ZnO covers ZnGa₂O₄-Ga₂O₃ at high Zn loading. This leads to inefficient use of photons for water splitting reactions (**Figure 3.1**) because the ZnO conduction band energy is very close to the one required for H₂ evolution (-0.2 eV compared to 0 eV, respectively) [36], thus ZnO does not have the appropriate energy for water reduction upon light absorption.

On the other hand, the lowest-unoccupied energy states (XANES onset) of Ga are shifted toward higher energies with higher Zn content (*appx. A, Figure 7.6-b*) as the amount of ZnGa₂O₄ increases (**Figure 3.2-b**), and pure ZnGa₂O₄ shows the highest K-edge energy (**Figure 3.3-b**, 4.42 eV as shown in *appx. A, Figure 7.7*). Thus, Ga in ZnGa₂O₄ has a considerably higher edge energy by ca. 1 eV compared to Ga₂O₃, implying a higher conduction band energy level of the former. These indications of higher conduction band energy level of ZnGa₂O₄, the slightly higher valence band energy by 0.05 ± 0.01 eV (using the 1st moment of the Kβ_{2,5} peak) determined for ZnGa₂O₄ with respect to that of β-Ga₂O₃ (smaller than 1.5 eV reported by valence band XPS) [32], and the Zn-loading-dependent coverage of ZnGa₂O₄ and ZnO over β-Ga₂O₃ surface point to the important roles of ZnGa₂O₄/Ga₂O₃ heterojunction as depicted in **Figure 3.4**. Due to the similar optical bandgaps, excitons

are generated in/on both materials and the electrons will migrate from ZnGa₂O₄ to Ga₂O₃ surface to catalyse reduction reactions and conversely the holes migrate from Ga₂O₃ to ZnGa₂O₄ to catalyse oxidation reactions. The creation of the heterojunction explains the reported longer life-time of photogenerated electrons and holes by transient spectroscopic methods [18, 32]. An adequate amount of ZnGa₂O₄ should be present on Ga₂O₃ to efficiently create the heterojunction, while sufficiently large area of Ga₂O₃ should also be exposed to catalyse hydrogen evolution reactions. On the other hand, upon ZnO formation on the catalyst surface due to excessive Zn-loading, light is merely absorbed by the material without energy harvesting for water splitting (**Figure 3.4**).

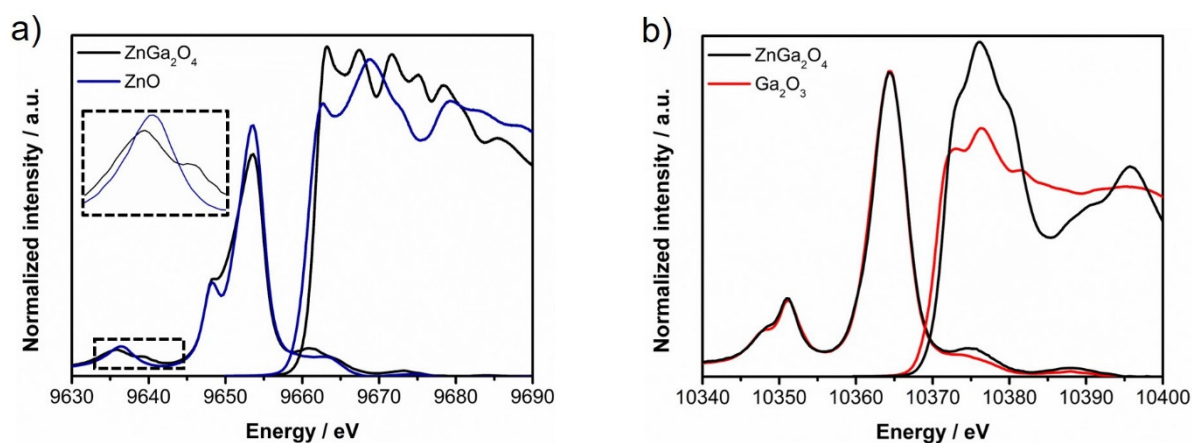


Figure 3.3. XAS and VtC-XES spectra for **a)** Zn K-edge and **b)** Ga K-edge. Pure ZnGa₂O₄ (black), ZnO (blue), and Ga₂O₃ (red). Spectral intensity was normalized to the spectral area.

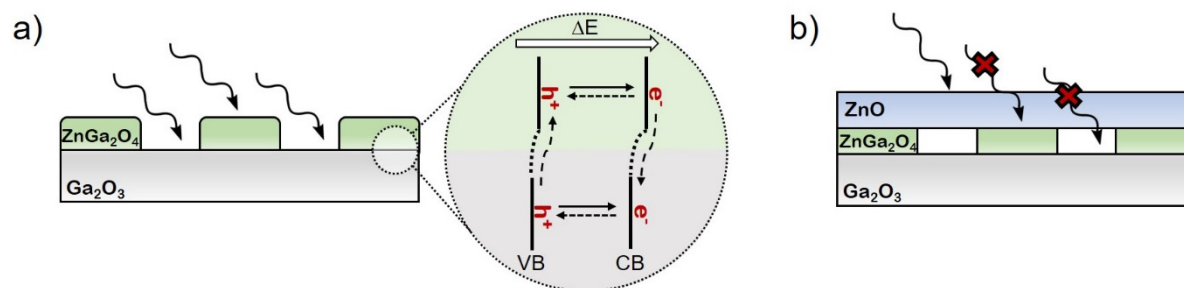


Figure 3.4. Schematic of light absorption for Zn-Ga₂O₃ materials with **a)** low Zn loadings (2-4 wt%) showing the electron and hole migrations between the ZnGa₂O₄/Ga₂O₃ heterojunction, and **b)** high Zn loadings (≥20 wt%).

3.3.3 Role of Rh-Cr co-catalyst

As presented in **Figure 3.1**, a small amount of Rh-Cr drastically boosts the catalytic activity of the Ga_2O_3 and $\text{Zn-Ga}_2\text{O}_3$ materials. Promoting effects of metal co-catalysts in photocatalytic reactions are generally attributed to their function as an electron trap and sink [9, 16, 37]. To firmly understand and attribute the function of Rh-Cr co-catalyst, the water splitting activity and structural changes of 4 wt% $\text{Zn-Ga}_2\text{O}_3$ with/without Rh-Cr were studied using silver nitrate as electron scavenger.

Photocatalytic experiments in the presence of silver nitrate (**Figure 3.5-b**) show fully suppressed H_2 production as anticipated by the efficient electron interception by Ag^+ at the location where free electrons are concentrated and released. To our surprise, only a small amount of O_2 was detected for both materials despite the well-documented function of Ag^+ to enhance water oxidation activity of photocatalysts [38, 39]. Also, the O_2 productivity with and without the Rh-Cr co-catalyst was similar, indicating disabled function of Rh-Cr in the presence of Ag^+ . STEM (*appx. A, Figure 7.8*) and Cr K-edge XANES (*appx. A, Figure 7.9*) of the Rh-Cr/ $\text{Zn-Ga}_2\text{O}_3$ material after the reaction in the presence of AgNO_3 clearly show that Ag deposition occurs around the Cr_xO_y particles, and also, the oxidation of Cr takes place (in comparison to reference spectra the initial +3 oxidation number of Cr increases, although it is not exactly +6, *appx. A, Figure 7.9*) [24]. Similarly to Cr, small changes in the electronic state of Rh were indicated after Ag deposition from the Rh K-edge XANES (Rh oxidation number is slightly oxidized, although initially is not exactly +3, *appx. A, Figure 7.10*) [24], although Rh and its spatial distribution could not be studied by TEM due to low Rh (0.5 wt%). Thus Rh-Cr, particularly Cr, is the site where electrons are released for reduction reactions and hence Ag is selectively deposited on Cr oxide particles. The reduction reaction proceeds in a sacrificial manner for Cr (i.e. Cr is self-oxidized) and thus Ag reduction is efficient through the reducing power of Cr_xO_y sites. This explains the lowered ability of the catalyst for charge separation thus leading to less efficient electron trap after Ag deposition at Rh-Cr sites. Furthermore, the lowered efficiency for charge separation due to the ineffective functioning of Rh-Cr upon Ag deposition explains the suppressed oxygen formation in the presence of Ag^+ (**Figure 3.5-a vs. 3.5-b**).

Ag deposition under illumination (i.e. photodeposition) is shown to be site selective and it is expected to uniquely influence the water splitting activity. This was verified by performing the photocatalytic water splitting tests in pure water using the material after Ag photodeposition for 30 min (20 wt% Ag determined by EDX) and using a comparable material prepared by the impregnation method at the same Ag loading (Figure 3.5-c and 3.5-d). In all cases, lower activity is found in comparison to the materials without Ag deposition (Figure 3.5-a). The most important difference is observed for the Rh-Cr promoted catalyst where Ag-impregnated catalyst showed relatively high H₂ productivity (4.9 mmol g_{cat}⁻¹ h⁻¹) in contrast to the minor activity of the Ag-photodeposited one (0.8 mmol g_{cat}⁻¹ h⁻¹). Microscopic study shows that the Ag deposition by the impregnation method leads to a more homogenous distribution of Ag, which is not site-selective (appx. A, Figure 7.11). Thus, the poisoning of the active sites is not prominent. On the other hand, the catalytic activity is largely suppressed when Ag selectively covers Rh-Cr co-catalyst (speculated for Rh).

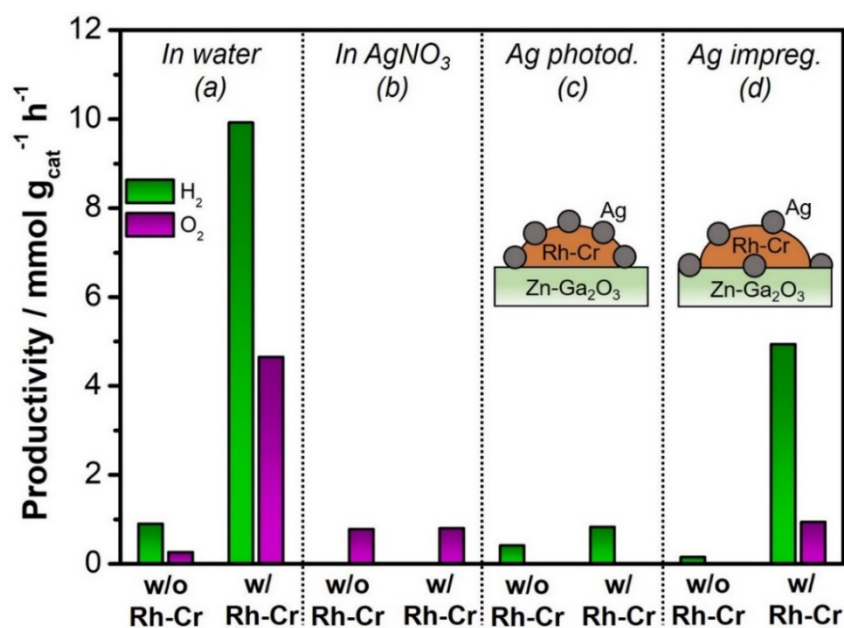


Figure 3.5. H₂ (green) and O₂ (purple) productivity of 4 wt% Zn-Ga₂O₃ with and without Rh-Cr in the photocatalytic water splitting reaction; **a**) in pure water, **b**) in the presence of 0.01 M AgNO₃, **c**) in pure water after 20 wt% Ag-photodeposition and **d**) in pure water after 20 wt% Ag-impregnation. The duration of photocatalytic test was 1.5 h (averaged from 4 runs) except for the case in the presence of AgNO₃ (**b**) for which the test was performed only for 30 min due to fast deactivation induced by Ag deposition on the catalysts. The small difference in the catalytic activity (**a**) compared to those shown in Figure 3.1 is due to the different batch of catalysts synthesised and possibly to the experimental error of different photocatalytic tests. Nevertheless, the difference is within the levels of common tolerance (about 10%).

3.3.4 Synergistic effects of Rh-Cr and Zn

Figure 3.5 also shows that O₂ productivity is fully suppressed when the function of Rh-Cr is disabled by the Ag deposition, affirming that the charge separation facilitated by the role of Rh-Cr as electron sink (reduction site) and the function of Zn through the formation of ZnGa₂O₄/Ga₂O₃ heterojunction (**Figure 3.4**) are interlinked, as also evidenced by the synergistic effects of Zn and Rh-Cr in the photocatalytic activity (**Figure 3.1**). With the aim to directly sense the influence of Rh-Cr co-catalyst on the electronic structure of Zn atoms as a proof of the synergistic interactions, here, the unoccupied state electronic structures of Zn are studied by XANES with *in situ* illumination.

As expected, the XANES difference spectra of Zn-Ga₂O₃ and Rh-Cr/Zn-Ga₂O₃ between the dark and illuminated conditions are very small, close to the level of noise even after signal to noise (S/N) improvement by averaging the respective spectra before subtraction (**Figure 3.6-a**). To drastically boost the sensitivity, the experiments were performed periodically in light-on/off cycles and the resulting spectra were averaged into one light-on/off cycle. Then the averaged spectra were treated by the mathematical engine of modulation excitation spectroscopy, phase sensitive detection (PSD) (**Figure 3.6-b** and *appx. A, Figure 7.12*) [23]. PSD highlights only the intensity which varies at the same frequency as the light on/off stimulus, thus effectively eliminates uncorrelated noise and time-independent static signals. Only the phase-domain spectra at $\varphi_{\text{PSD}} = 0$ are presented since this would be equivalent to the difference spectra of the catalyst under-light minus under-dark. The improvement in S/N is evident, although the spectral features are very small. The physical nature of the small spectral characteristics is verified by the so-called in-phase angle analysis (*appx. A, Figure 7.12-iii*), clearly showing distinct phase angles for each peak (continuously shifting phase angles are due to peak overlaps as expected in XANES, also serving as the proof of the physical nature of the low intensity signals and not of noise).

Two important observations can be made from this light-on/off XANES study. First, the electronic structure of Zn atom, which is present as ZnGa₂O₄ (*vide supra*), is perturbed by the illumination. This is indirect evidence of the charge separation at

ZnGa₂O₄ due to which the electronic structure of Zn is also influenced. Another very striking observation is the effect of Rh-Cr on the degree of the change. The degree of change in the Zn electronic structure is about double by the presence of Rh-Cr co-catalyst. Detailed spectral analysis (i.e. how the Zn orbitals are altered) is beyond the scope of this work; nevertheless, the clearly different spectral features (e.g. where the maxima appears for the two materials) indicate the electronic structure of Zn atom under illumination is different with/without Rh-Cr, possibly due to the different degree of charge separation. This is the first and a clear proof that the charge separation facilitated by Rh-Cr communicates with the electronic structure of Zn. Also, the results imply that the physical vicinity of Rh-Cr is important and how and where Rh-Cr are deposited (e.g. on Ga₂O₃, ZnGa₂O₄ or at their interface) matter for the photocatalytic activity.

Chapter 3

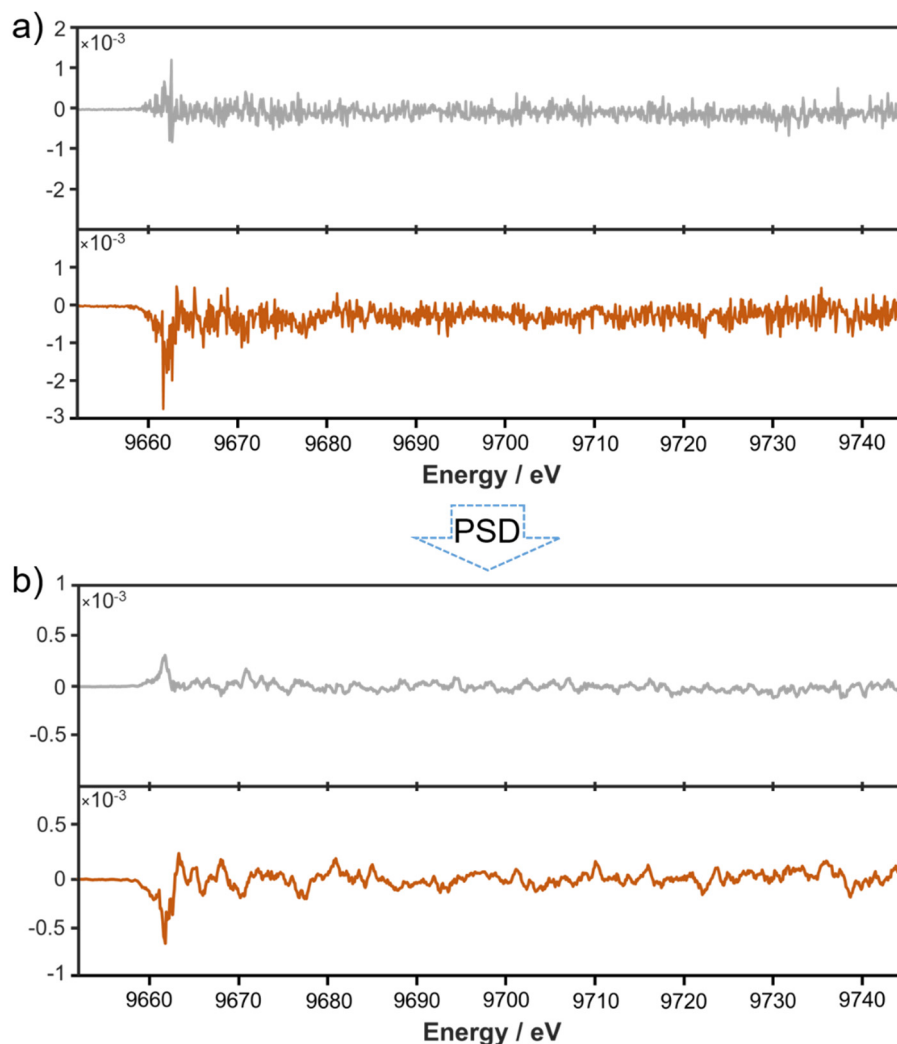


Figure 3.6. a) Averaged Zn K-edge HERDF-XANES spectra, light off subtracted from light on cycle, and b) phase-domain response with $k = 1$ of 4 wt% Zn-modified Ga_2O_3 (grey), and Rh-Cr/4wt% Zn- Ga_2O_3 (brown).

3.4 Conclusions

Zn and Rh-Cr co-catalysts greatly influence the photocatalytic water splitting activity of Ga_2O_3 and their synergistic function is confirmed. At the optimum Zn-loading (2-4 wt%) the formation of the $\text{ZnGa}_2\text{O}_4/\text{Ga}_2\text{O}_3$ heterojunction, with an appropriate exposure of both materials for the redox reactions, is favoured, facilitating the charge transfer and separation between the two semiconductor materials and enhancing the photocatalytic activity. At higher Zn-loading (≥ 20 wt%) ZnO is formed, covering the ZnGa_2O_4 and Ga_2O_3 surface, and it negatively influences the photocatalytic activity due to the light absorption properties and water splitting activity of ZnO. The role of

Rh-Cr as electron trapping sites is evidenced by the studies in the presence of Ag⁺, clearly showing the poisoning of the Rh-Cr active sites after Ag deposition. By depositing Ag in a selective (photodeposition) and non-selective (impregnation) fashions and detailing the electronic structure change of Cr, the function of Rh-Cr co-catalyst in water splitting reaction was affirmed. Finally, the concerted actions between the electron sink (Rh-Cr) and the ZnGa₂O₄/Ga₂O₃ heterojunction are proven by *in situ* illumination modulation excitation XAS spectroscopy. The subtle electronic structure change of Zn atoms in ZnGa₂O₄ under illumination is uncovered. The degree of the change is boosted by the presence of Rh-Cr, serving as a direct proof of communication and synergy of Zn and Rh-Cr co-catalysts on the electronic structure level under photocatalytic conditions.

Bibliography

1. Hernandez-Alonso, M.D., et al. *Energy & Environmental Science*, 2009. **2**(12): p. 1231-1257.
2. Kudo, A. and Y. Miseki. *Chemical Society Reviews*, 2009. **38**(1): p. 253-278.
3. Maeda, K. and K. Domen. *The Journal of Physical Chemistry Letters*, 2010. **1**(18): p. 2655-2661.
4. Fujishima, A. and K. Honda. *Nature*, 1972. **238**(5358): p. 37-38.
5. Bard, A.J. and M.A. Fox. *Accounts of Chemical Research*, 1995. **28**(3): p. 141-145.
6. Linsebigler, A.L., G. Lu, and J.T. Yates. *Chemical Reviews*, 1995. **95**(3): p. 735-758.
7. Maeda, K. and K. Domen. *The Journal of Physical Chemistry C*, 2007. **111**(22): p. 7851-7861.
8. Osterloh, F.E. *Chemistry of Materials*, 2008. **20**(1): p. 35-54.
9. Liu, G., et al. *Journal of Materials Chemistry*, 2010. **20**(5): p. 831-843.
10. Yanagida, T., Y. Sakata, and H. Imamura. *Chemistry Letters*, 2004. **33**(6): p. 726-727.
11. Maeda, K., et al. *The Journal of Physical Chemistry B*, 2006. **110**(26): p. 13107-13112.
12. Maeda, K., et al. *Nature*, 2006. **440**: p. 295.
13. Maeda, K., et al. *Angewandte Chemie International Edition*, 2006. **45**(46): p. 7806-7809.
14. Sakata, Y., et al. *ChemSusChem*, 2011. **4**(2): p. 181-184.
15. Sakata, Y., et al. *Journal of Catalysis*, 2014. **310**: p. 45-50.
16. Shimura, K., T. Yoshida, and H. Yoshida. *The Journal of Physical Chemistry C*, 2010. **114**(26): p. 11466-11474.
17. Sakata, Y., et al. *Catalysis Letters*, 2008. **125**(1): p. 22-26.
18. Bazzo, A. and A. Urakawa. *Catalysis Science & Technology*, 2016. **6**(12): p. 4243-4253.
19. Gallo, E. and P. Glatzel. *Advanced Materials*, 2014. **26**(46): p. 7730-7746.
20. Glatzel, P. and U. Bergmann. *Coordination Chemistry Reviews*, 2005. **249**(1): p. 65-95.
21. López, R. and R. Gómez. *Journal of Sol-Gel Science and Technology*, 2012. **61**(1): p. 1-7.
22. Murphy, A.B. *Solar Energy Materials and Solar Cells*, 2007. **91**(14): p. 1326-1337.
23. Urakawa, A., T. Bürgi, and A. Baiker. *Chemical Engineering Science*, 2008. **63**(20): p. 4902-4909.
24. Maeda, K., et al. *The Journal of Physical Chemistry B*, 2006. **110**(28): p. 13753-13758.
25. Lutterotti, L., et al. *Materials Science Forum*, 1998. **278-281**: p. 87-92.
26. Ravel, B. and M. Newville. *Journal of Synchrotron Radiation*, 2005. **12**(4): p. 537-541.
27. Ressler, T., et al. *Environmental Science & Technology*, 2000. **34**(6): p. 950-958.
28. Baurecht, D. and U.P. Fringeli. *Review of Scientific Instruments*, 2001. **72**(10): p. 3782-3792.

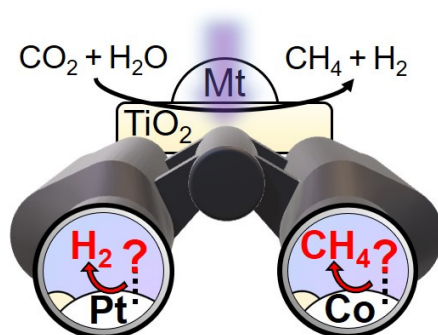
29. Urakawa, A., T. Bürgi, and A. Baiker. *Chemical Physics*, 2006. **324**(2): p. 653-658.
30. Chen, X., et al. *Chemical Reviews*, 2010. **110**(11): p. 6503-6570.
31. Tabata, S., et al. *Catalysis Letters*, 1995. **34**: p. 245-249.
32. Wang, X., et al. *Physical Chemistry Chemical Physics*, 2013. **15**(44): p. 19380-19386.
33. Hill, J.C. and K.-S. Choi. *The Journal of Physical Chemistry C*, 2012. **116**(14): p. 7612-7620.
34. Wang, Z., et al. *Catalysis Science and Technology*, 2016. **6**: p. 1025-1032.
35. Glatzel, P., et al. *Journal of Electron Spectroscopy and Related Phenomena*, 2013. **188**: p. 17-25.
36. Inoue, T., et al. *Nature*, 1979. **277**: p. 637.
37. Disdier, J., J.-M. Herrmann, and P. Pichat. *Journal of the Chemical Society, Faraday Transactions 1: Physical Chemistry in Condensed Phases*, 1983. **79**(3): p. 651-660.
38. Maeda, K., et al. *The Journal of Physical Chemistry C*, 2008. **112**(9): p. 3447-3452.
39. Ohtani, B., et al. *Journal of Photochemistry and Photobiology A: Chemistry*, 1992. **64**(2): p. 223-230.

Chapter 3

4.

Reaction mechanism of modified TiO_2 with promoters

Active surface species ruling product selectivity in photocatalytic CO_2 reduction over Pt or Co promoted TiO_2



4.1 Introduction

Photocatalytic reduction of CO₂ can open paths for sustainable developments to convert the energy contained in photons into chemical forms by the synthesis of chemical energy carriers such as CH₄ and CH₃OH [1, 2]. However, great challenges are associated with the conversion using light due to the high thermodynamic stability of CO₂ molecule. First, high energy input is required to activate CO₂ as evident from the high reduction potential of -1.9 V (E_{red}^0 , vs. RHE) to form a generally well-accepted intermediate, CO₂ radical anion [3]. Another challenge is related to the presence of protons in photocatalytic reactors to produce hydrocarbon or oxygenate chemicals by its reaction with CO₂ and electron. The formation of hydrogen by the proton reduction reaction, considered as water reduction in aqueous media, is energetically more favourable ($E_{\text{red}}^0 = 0$ V vs. RHE) and consequently hydrogen production is generally more facile over CO₂ reduction in the photocatalytic conversion of CO₂ [4, 5]. Therefore, the design of photocatalysts, which can efficiently harness light and at the same time suppress the proton reduction over CO₂ reduction, is demanded.

In addition to catalyst tuning, engineering approaches such as increased CO₂ pressure [6-8] are found effective in improving CO₂ reduction performance and product yields. By performing the reaction in gas-phase using gaseous CO₂ and water vapour, it is possible to regulate and limit the amount of water (thus proton) in the system with respect to that of CO₂, thereby creating a favourable environment for CO₂ reduction. At sufficiently high reaction temperature (above 373 K), this approach could avoid water condensation on catalyst surface and lead to selective production of carbon-containing chemicals over H₂ [9]. Furthermore, one of the major issues of photocatalytic CO₂ reduction over the most actively researched photocatalyst materials, TiO₂ and TiO₂-based materials, is their stability and this aspect is often neglected in literature and not well understood. Typically, the catalytic activity diminishes gradually over time [9, 10]. The origin of the catalyst deactivation has been explained by (i) the loss of surface active sites due to the deposition of carbonaceous species [9], (ii) changes in the metal oxidation state and/or corrosion [11, 12] and (iii) the decrease of surface OH or defective (active) sites [13, 14]. However, convincing

evidence of the activation as well as deactivation processes is not available to date, hindering rational designing of photocatalysts for CO₂ reduction.

The most popular and convenient method to improve photocatalysts is to load suitable co-catalyst(s) on the catalyst to promote electron trapping and facilitate redox reactions of surface chemical species [15, 16] as discussed in *chap. 1, section 1.2.2.1*. Numerous co-catalysts have been investigated for TiO₂ targeting at H₂ production and CO₂ reduction [17, 18]. Pt co-catalyst is reported to induce great enhancement in CO₂ photoreduction due to the formation of Schottky-barrier at Pt-TiO₂ interface [19-21]. Still, the high cost of Pt has motivated researchers to look for alternative co-catalysts to replace Pt by other inexpensive and earth-abundant metals. Among them, cobalt (or cobalt oxide) has drawn attentions because of its high earth-abundance and visible light adsorption properties [19-22].

Reflecting this background, herein we report a mechanistic study of photocatalytic CO₂ reduction over TiO₂, specifically to elucidate the influence of Pt and Co co-catalysts on the formation of surface chemical species and the reaction pathways influencing product selectivity. Surface chemical species and their evolution were elucidated by *in situ* diffuse reflectance infrared Fourier transformed spectroscopy (DRIFTS). Spectral interpretations were facilitated by multivariate spectral analysis, particularly by means of multivariate curve resolution (MCR) to disentangle time-resolved spectra with high-level of band overlaps into a set of chemically meaningful pure-component spectra with respective concentration profiles through the kinetic resolution without the need of reference [23-25]. The evolutions of surface chemical species are correlated with the comparative catalytic tests to gain insights into the effects of co-catalysts on photocatalytic CO₂ reduction chemistry.

4.2 Experimental

4.2.1 Materials

Pt- and Co-modified TiO₂ materials (denoted as Pt/TiO₂ and Co/TiO₂) were prepared by wet impregnation method followed by a thermal treatment (*chap. 2, section 2.1.2*). The loading of Pt and Co was 0.2 wt% based on the weight of metal with respect to that of TiO₂. Commercial P25 (Degussa) was used as TiO₂ source.

4.2.2 Reaction setup

Photocatalytic CO₂ reduction activity tests were performed at 423 K to facilitate CO₂ reduction with respect to H₂ formation (*vide supra* [9]) using the gas-phase reaction setup presented in [chap. 2, section 2.2](#). Powdered catalyst (100 mg) was charged at the bottom of the reactor. The photocatalyst was treated at 423 K under N₂ at the flow rate of 4.5 mL min⁻¹ for 1 h prior to irradiation with a 400 W high-pressure Hg lamp (UV-Technik) without optical filter. Light was placed at 8 cm away from the optical port of the reactor. Photocatalytic reaction was performed under CO₂ flow (4.5 mL min⁻¹) saturated with H₂O vapour (water saturator was maintained at 323 K). Repeated and periodical light on/off cycles of 1.5 h duration were used to evaluate catalytic activity by GC-MS.

In situ DRIFTS studies were performed on a Vertex 70V instrument (Bruker) equipped with a liquid nitrogen-cooled MCT detector and a Praying Mantis optical accessory (Harrick). For a more detailed setup description see [chap. 2, section 2.3.3](#). A few mg of a powder catalyst were loaded into the sample holder of the DRIFTS cell ([chap. 2, Figure 2.8](#)) and the sample was set at 423 K under He flow at 4.5 mL min⁻¹. Prior to admission of gaseous CO₂ and H₂O to the cell, the catalyst was first treated under He for 1 h, then the atmosphere was switched to water-saturated CO₂ at 4.5 mL min⁻¹ when periodic light off/on cycles of 1 h duration each were initiated (Dark1→UV1→Dark2→UV2→...). All measurements were conducted isothermally at 423 K. A SwiftCure PLU-10 UV curing setup (UV-Consulting Peschl) equipped with a high-pressure Hg lamp (250 W) and a quartz optical fibre (3 mm core) was used as the light source. The UV light was guided to the sample through the optical fibre through a window without disturbing the IR sampling. IR spectra were acquired repeatedly for 60 s at the spectral resolution of 4 cm⁻¹. The spectrum recorded under He right before switching to the flow of water-saturated CO₂ was used as the background.

4.2.3 Multivariate spectral analysis

From the time-resolved DRIFT spectra, MCR allows successful extraction of the kinetically pure spectra and corresponding concentration profiles, as described in

chap. 2, section 2.3.4. In this work, MCR was performed on a complete series of acquired spectra, that is, under (i) He (light off) and then under gaseous CO₂+H₂O with (ii) light off (Dark1), (iii) light on (UV1), (iv) light off (Dark2) and (v) light on (UV2). Non-negativity constraints were applied for the MCR analysis.

4.3 Results and discussion

4.3.1 Photocatalytic CO₂ reduction by TiO₂, Co/TiO₂ and Pt/TiO₂

Photocatalytic reduction of CO₂ over TiO₂, Co/TiO₂ and Pt/TiO₂ in the presence of water vapour under the continuous flow condition shows that CH₄ and H₂ are the only detectable products, with the amounts and evolution profiles of the products distinctly different for each catalyst (**Figure 4.1** and *appx. B, Table 7.2*). If the formation rates of CH₄ and H₂ are constant, we expect to observe a straight line for the product concentrations under the flow condition. In reality, a maximum in the concentration of CH₄/H₂ after 15-20 min is observed and then it decays rapidly until it reaches a steady value. Such a steady value is more notably observed for H₂ production over TiO₂ (e.g. **Figure 4.1-a'**). The former activity has been termed *transient* activity indicative of deactivation due to a non-regenerative consumption of active surface species or irreversible change of an active catalyst state. The latter activity is termed *steady-state* activity indicative of stable photocatalytic activity likely induced by the semiconducting nature, i.e. stable charge separation, of catalyst materials. At this high reaction temperature (423 K), CH₄ can be formed and apparently the photocatalytic activity for both CH₄ and H₂ production is dominated by the transient one in agreement with the previous report [9].

Chapter 4

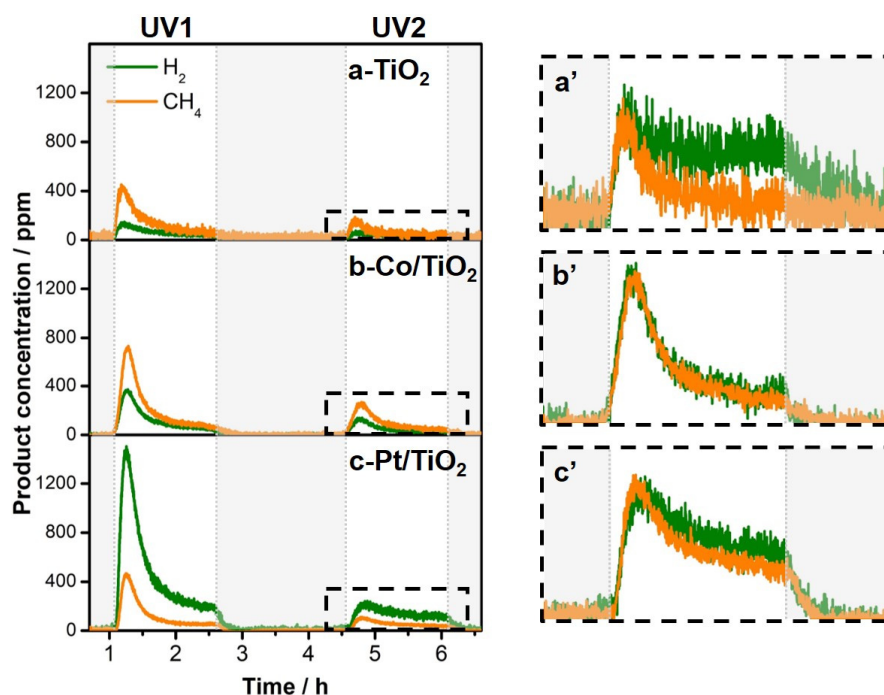


Figure 4.1. (left) Concentration profiles of CH₄ (orange) and H₂ (green) during photocatalytic CO₂ reduction at 423 K under two UV irradiation cycles (UV1 and UV2) of 1.5 h duration over **a**) TiO₂, **b**) Co/TiO₂, and **c**) Pt/TiO₂. (right) Normalized concentration profiles of CH₄ (orange) and H₂ (green) to the maximum concentration during UV2 for TiO₂ (**a'**), Co/TiO₂ (**b'**), and Pt/TiO₂ (**c'**).

At first glance, notable differences in the selectivity trend and amount of products for TiO₂ or Co/TiO₂ against Pt/TiO₂ are clarified. TiO₂ (**Figure 4.1-a**) is more selective for CH₄ production and a similar selectivity trend is confirmed for Co/TiO₂ (**Figure 4.1-b**), with a boost in the production of both CH₄ and H₂ by 44% (2.58 μmol g_{cat}⁻¹ h⁻¹) and 90% (1.52 μmol g_{cat}⁻¹ h⁻¹), respectively, by the addition of the Co co-catalyst. In contrast, the selectivity trend of Pt/TiO₂ (**Figure 4.1-c**) is reversed with remarkably higher productivity of H₂ (5.28 μmol g_{cat}⁻¹ h⁻¹) compared to that of CH₄ (1.46 μmol g_{cat}⁻¹ h⁻¹) [9, 17]. A study of Co/TiO₂ with visible light reported that H₂ was evolved but CH₄ was not detected [22], hinting that there might be possible effects of excitation light wavelength on product selectivity.

The major, transient activities for CH₄ and H₂ production are recovered only to a minor extent after the dark period. Hence, the subsequent irradiation cycle (UV2) showed poorer catalytic performance, and this is a clear indication of deactivation of the photocatalysts or continuous depletion or ineffective regeneration of active species (**Figure 4.1**, and *appx. B, Figure 7.13*) [9, 11, 13, 14].

Looking closer at the CH₄ and H₂ concentration profiles of the three catalysts evidences that the evolution of the two gases is almost identical for Co/TiO₂ and Pt/TiO₂ when the profiles are normalized to the maximum values (**Figure 4.1-b'** and **4.1-c'** during UV2; the same conclusion can be drawn from also the concentration profiles in UV1, *appx. B, Figure 7.13*). In contrast, for TiO₂ the steady-state activity dominates for H₂ production while the transient one is responsible for CH₄ production (**Figure 4.1-a'**). These results clearly suggest that CH₄ and H₂ evolve from the same or highly linked (i.e. in terms of reaction pathways) surface intermediate species over Co/TiO₂ and Pt/TiO₂, whereas two different reaction pathways are active for the formation of CH₄ and H₂ over TiO₂. The former is likely through by an irreversible consumption of surface intermediate species, whereas the latter through the common pathway with separated charges over the semiconducting TiO₂ surface [19].

4.3.2 Mechanistic study of photocatalytic CO₂ reduction by *in situ* DRIFTS

To shed light on the origin of the catalytic activities, reactive surface intermediates and determining factors of product selectivity, *in situ* DRIFTS studies are performed for the three catalysts, mimicking the condition of the catalytic tests (**Figure 4.1**). The formation of H₂ and CH₄ could not be confirmed due to the small amount of the catalysts used and thus to the detection limit. Nevertheless, the evolutions of surface chemical species identified by *in situ* DRIFTS are in line with those observed in the catalytic tests as discussed below; hence the results from the two different experiments are interpreted in a comparable and comparative manner.

4.3.2.1 Pt/TiO₂

To our surprise, remarkable spectral changes are observed for Pt/TiO₂ in the carbonyl stretching region (2040-2160 cm⁻¹), whereas only very minor changes are detected for TiO₂ and Co/TiO₂ (*appx. B, Figure 7.14*). On Pt/TiO₂, three different surface carbonyl species are identified (**Figure 4.2-a**) with respective characteristic bands: (i) CO on reduced Pt (Pt⁰) at 2065 cm⁻¹, (ii) CO on oxidized Pt (Ptⁿ⁺) at 2084 cm⁻¹ [26-28], and (iii) CO bound to Ti³⁺ at 2114 cm⁻¹ [29, 30]. These three bands emerge and diminish dynamically responding to the atmosphere change and light on/off. Ti⁴⁺-CO bands reported at 2180-2200 cm⁻¹ are not detected [31, 32], possibly

Chapter 4

due to its low stability. To the best of our knowledge, this is the first report on the involvement of carbonyl species during the photocatalytic CO₂ reduction and this is enhanced by the Pt co-catalyst.

Upon changing the gas atmosphere from He to water-saturated CO₂ (Dark1) at 423 K, we first observe an increase in the band intensity of CO on Ti³⁺ as clearly confirmed in the 2D plot (**Figure 4.2-a**) and the component concentration profile extracted by the multivariate spectral analysis (**Figure 4.2-b** region **1**, *appx. B*, **Figure 7.15-b**), the corresponding component spectrum of CO on Ti³⁺ is presented in *appx. B*, **Figure 7.15-a**). After ca. 15-20 min in Dark1, at the expense of disappearance of this band, new bands of CO on Pt⁰ and on Ptⁿ⁺ appear prominently and mildly, respectively (**Figure 4.2-a**, and **4.2-b** region **2**). In a lower frequency region of 1300-1700 cm⁻¹, formate, carbonate and bicarbonates species are identified (*appx. B*, **Figure 7.16-a**) [32-35]. Along with the increase of the band of CO on Ti³⁺ (region **1**), the carbonate bands increase remarkably. When CO on Ti³⁺ disappears and CO on Pt⁰/Ptⁿ⁺ is formed (region **2**), there is a significant decrease in the intensity of the carbonate bands. It should be noted that these chemical transformations are taking place on the catalyst surface without irradiation of UV light. These observations indicate that the TiO₂ surface induces multiple surface chemical transformations as depicted in **Figure 4.2-c**, regions **1-2**. After the He treatment, the TiO₂ surface is partially reduced, and upon admission of water-saturated CO₂, first CO₂ undergoes transformation through its surface adsorption mainly as carbonates, leading to dissociation to CO on Ti³⁺. The subsequent decrease of CO on Ti³⁺ and formation of CO on Ptⁿ⁺ imply that there are oxidation processes of the catalyst by the oxygen atom of CO₂ and also H₂O filling the TiO₂ defective sites. This oxidation of TiO₂ renders the adsorbed CO on TiO₂ to migrate to Pt⁰, leading to the abundant formation of CO adsorbed on Pt⁰ at the end of Dark1.

Subsequently, upon light irradiation (UV1) a sudden and drastic decrease of CO on Pt⁰ and the sharp and transient rise of CO on Ti³⁺ are observed. The latter suggests momentary reduction of Ti to Ti³⁺ (**Figure 4.2-b** region **3**) as typically expected from an electron injection or formation of surface vacancies. In a synchronous fashion, the amount of surface formates increases (**Figure 4.2-b** region

3). These observations point out that CO on Pt⁰ reacts with surface OH groups, forming formate species (**Figure 4.2-c** region 3) [36, 37]. The assignment of formate species is confirmed by the emergence of the C-H stretching bands (*appx. B, Figure 7.17*) [34, 35, 38]. On the other hand, the sharp increase of Ptⁿ⁺-CO band indicates a concerted redox process of Pt (oxidation) and TiO₂ (reduction) upon irradiation. After this rapid transformation phase (region 3), there is a gradual decrease of CO on TiO₂ and formate species, accompanied by a steady increase of carbonate species (region 4).

The major photocatalytic activity of Pt/TiO₂ for CO₂ reduction and H₂O splitting is of highly transient nature as illustrated in **Figure 4.1**, and the highly linked or identical chemical origin (intermediate) for the source of CH₄ and H₂ has been suggested (*vide supra*). The observed evolutions of surface chemical species upon light irradiation, especially in region 3 elucidated by DRIFTS match well with the transient product evolution profiles of the catalytic test. Hence, surface formates are suggested to be the intermediate leading to CH₄ as well as H₂ over Pt/TiO₂. It is well known that metallic Pt can efficiently catalyse decomposition of formate/formic acid to yield H₂ [27, 39, 40] and formates can also be an intermediate to methane by further reduction [21, 41, 42]. The former reaction as well as the formation of formate species seem largely favoured or facilitated by the presence of Pt (**Figure 4.2-c**) and this explains the highest transient photocatalytic activity and largest selectivity toward H₂ of Pt/TiO₂ among the three catalysts in photocatalytic CO₂ reduction.

In the catalytic test (**Figure 4.1**), the transient activity is not restored after the first light on/off cycle and considerably lower CH₄ and H₂ productivities are found during UV2. The concentration profiles of the surface species elucidated by the DRIFTS study (**Figure 4.2-b**) evidence that the active formate species are not formed during the subsequent dark (Dark2) and irradiation (UV2) phases (**Figure 4.2-b** regions 5 and 6), supporting that formate is indeed the active intermediate and the catalyst surface is passivated after the first irradiation (UV1). Based on the continuous decrease of CO on Pt⁰, irreversible oxidation of Pt is suggested. Although TiO₂ surface can still be reduced to create surface vacancies as indicated by an initial increase of CO on Ti³⁺ during UV2 (region 6), the oxidation of Pt is suggested to play more critical

Chapter 4

role in the inefficient formation of surface formates. As a consequence, the catalyst surface is more dominated by carbonates over time and the H_2 and CH_4 productivities cannot be restored (**Figure 4.2-c**).

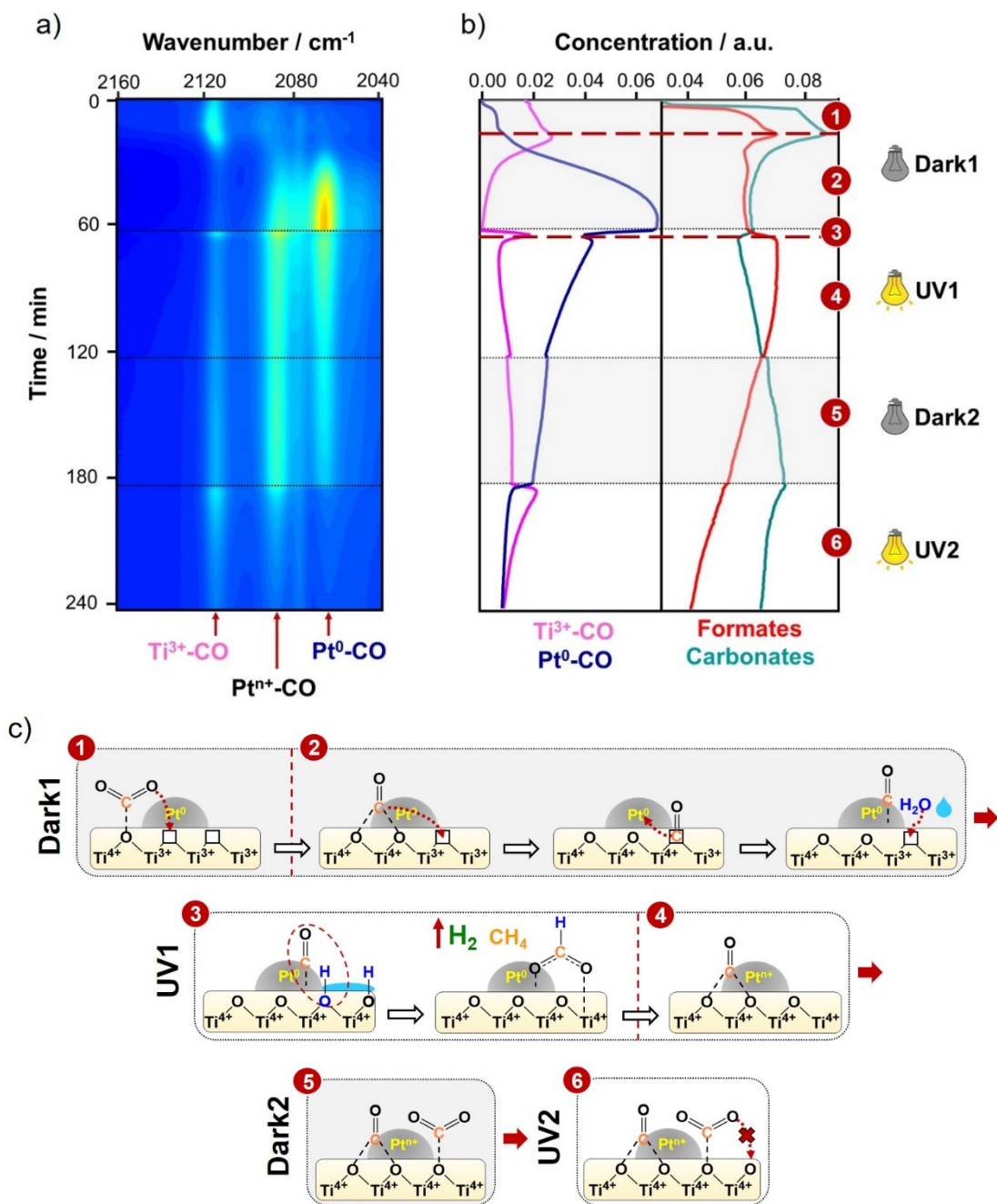


Figure 4.2. **a)** Evolution of surface carbonyl species on Pt/TiO₂ with absorbance from -0.02 (blue) to 0.16 (red) under Dark1, UV1, Dark2, and UV2 (top to bottom). **b)** Component concentration profiles of Ti³⁺-CO (pink) and Pt⁰-CO (blue) obtained by the MCR analysis of **a** and of those of formate (red) and carbonate (cyan) species obtained by the MCR analysis of the spectra in the region between 1300-1700 cm⁻¹ (component spectra can be found in *appx. B, Figure 7.16*). **c)** Proposed CO₂ reduction mechanism over Pt/TiO₂.

4.3.2.2 TiO₂ and Co/TiO₂

To gain further insights into the co-catalyst effects, comparative *in situ* DRIFTS studies performed for Co/TiO₂ and bare TiO₂ to understand the origin of higher CH₄ selectivity of these materials in comparison to Pt/TiO₂ as well as higher steady-state H₂O splitting activity of TiO₂ (**Figure 4.1**). As a general trend, both carbonates and bicarbonates species (*appx. B, Figure 7.16-b* and *7.16-c*) evolve under Dark1 with a notable initial concentration increase (**Figure 4.3-a** and **4.3-b** region **1**) followed by a decrease when formate species emerge (region **1**; a different nature of formates on Co/TiO₂ and TiO₂ compared to those on Pt/TiO₂ is suggested in *appx. B, Figure 7.16*). In contrast to Pt/TiO₂, there are negligible indications and changes in the region of adsorbed CO (*appx. B, Figure 7.14*). This implies that the redox process of TiO₂ and also that of Co is less pronounced compared to the case of Pt/TiO₂, suggesting the important role of Pt facilitating the redox surface chemistry of TiO₂. Nevertheless, a certain concentration of defective sites on TiO₂ are expected to be present, and consequently, a similar mechanism as described over Pt/TiO₂ for the formation of (bi)carbonates and reaction of water with TiO₂ surface are assumed (**Figure 4.3** regions **1** and **2**).

Upon light irradiation (UV1), the concentration of formate species dropped for both Co/TiO₂ (**Figure 4.3-a** region **3**) and TiO₂ (inset, **Figure 4.3-b** region **3**), which was then regained gradually over time. This concentration profile is highly contrasting to the case of Pt/TiO₂ (**Figure 4.2-b** region **3**) where surface formate species increased rapidly upon irradiation. Nevertheless, the major catalytic activity for CH₄ and H₂ formation is of transient nature (**Figure 4.1**) and the sudden change of formate species concentration upon irradiation is the most linked indication to transient catalytic activity. We interpret that in case of Pt/TiO₂ the formation rate of surface formates is higher than that of its decomposition initially, while the opposite is observed for Co/TiO₂ and TiO₂, explaining the initial consumption of formates upon irradiation for the latter cases. It is interesting to note that the presence of Co promoter uniquely enhances the formation of bicarbonate species (**Figure 4.3-a** region **3**) under irradiation. This is likely due to the modification of TiO₂ with more basic properties of cobalt oxide [30, 43]. Surface bicarbonates concentration increases while formates concentration decreases; thus, a fraction of the surface formates species might react

Chapter 4

with surface water leading to bicarbonate species. A similar trend of surface species evolution is observed in the second irradiation cycle (UV2). However, as revealed from the catalytic tests, the degree in the decrease of formate species is less pronounced during UV2, supporting that surface formates is the origin of the transient catalytic activity.

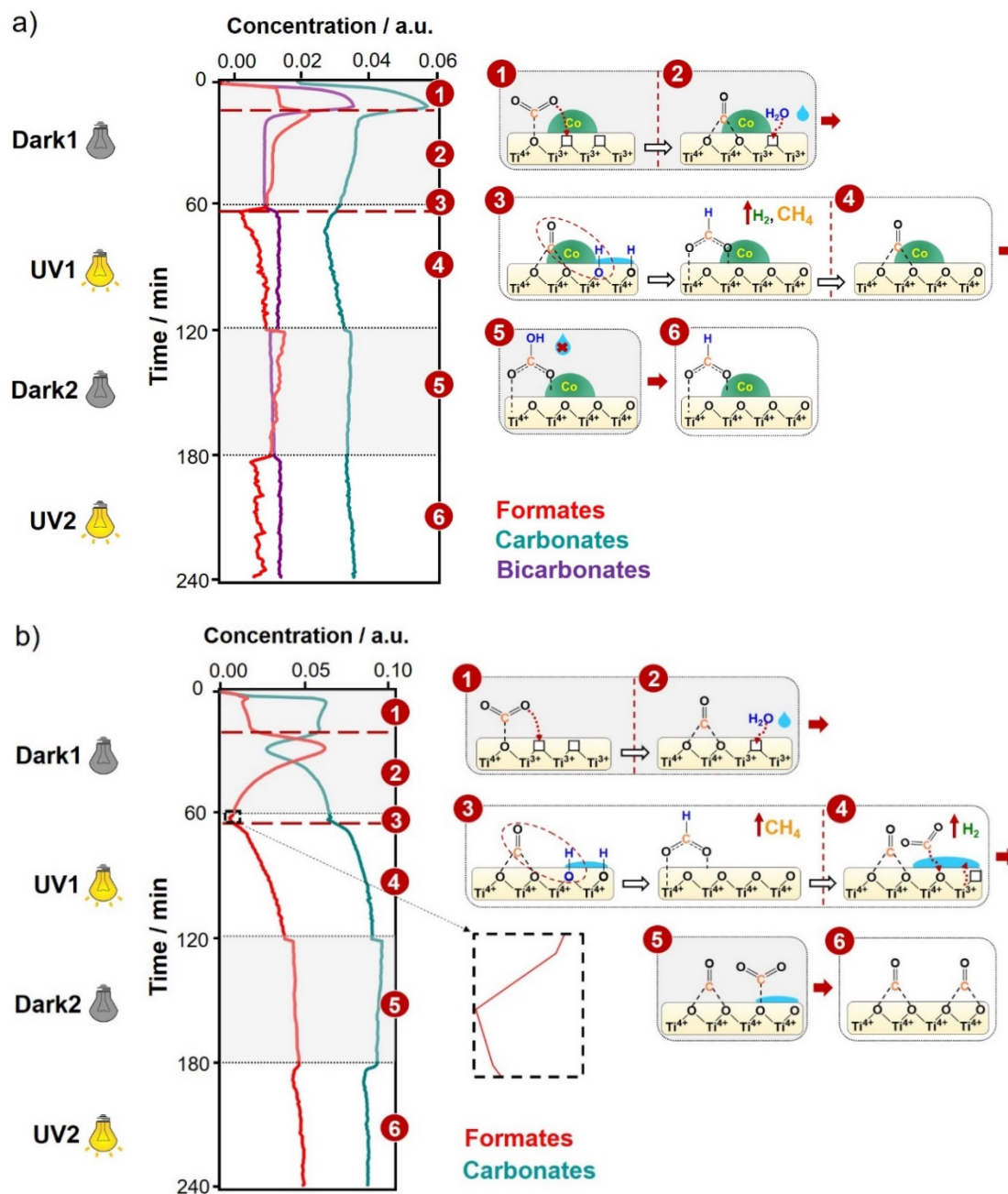


Figure 4.3. (left) Component concentration profiles of formate (red), carbonate (cyan), and bicarbonate (purple) species obtained by the MCR analysis for **a)** Co/TiO₂ and **b)** TiO₂ (corresponding component spectra can be found in *appx. B, Figure 7.16*). (right) Proposed CO₂ reduction mechanism of Co/TiO₂ **(a)** and TiO₂ **(b)**.

4.3.3 Origin of transient activity and deactivation

Above studies show that the transient nature of catalytic activity can be explained by the evolution of surface formates. In case of Pt/TiO₂, its formation as well as decomposition, especially to H₂, are facilitated by the function of Pt (**Figure 4.2**) due to its high activity for formate/formic acid decomposition [27, 39, 40]. In case of TiO₂ and Co/TiO₂, although surface formates are formed, its decomposition to formates is not facilitated and rather its decomposition to CH₄ is favoured (Co species are indicated to remain as Co₃O₄ during the reaction, *appx. B, Figure 7.18*). The identical transient evolution profiles of CH₄ and H₂ for Pt/TiO₂ and Co/TiO₂ (**Figure 4.1**) suggest that formates are the common intermediate for their formation.

On the other hand, as remarked in **Figure 4.1**, TiO₂ shows comparably higher steady-state activity for water splitting, while the steady-state activity is virtually absent for Co/TiO₂ despite the similar photocatalytic activity and selectivity trend of Co/TiO₂ and TiO₂ (**Figure 4.1**). The *in situ* DRIFTS studies (**Figure 4.3**) clarify that the major difference between the two is the presence of bicarbonate surface species in case of Co/TiO₂ whereas carbonate species are more dominant on TiO₂ under the photocatalytic conditions. In addition, in case of Pt/TiO₂ the oxidation of Pt also largely contributes to deteriorate the photocatalytic performance (*vide supra*). Bicarbonate is considered as a protonated form of carbonate and its formation should be facilitated by the presence of surface water. Therefore, the absence of water splitting activity of Co/TiO₂ suggests that water molecules cannot reach TiO₂ surface due to its reaction with carbonates to form bicarbonates which block the surface sites of TiO₂ (**Figure 4.3-a region 5**). On the other hand, carbonates are the dominant surface species on TiO₂ and bicarbonate formation is not facilitated. Thus, when carbonates do not fully cover the TiO₂ surface, water molecules can meet the active sites of TiO₂ under irradiation and H₂ can be produced (**Figure 4.3-b region 4**).

In all cases, a gradual increase of carbonate species is observed with time over light on/off cycles and surface site-blocking by the carbonates is indicated as the main cause of photocatalyst deactivation. The blockage of surface sites and consequent changes of surface chemical states are indicated by Raman spectroscopic characterization of the catalysts before/after the reactions, where an increase in

Chapter 4

fluorescence signals is observed after the reaction (*appx. B, Figure 7.19*) due to accumulation of carbonaceous species [44, 45]. The procedure to reactivate/enhance the catalytic activity by adding methanol into the reaction mixture [13] clearly shows that both CH₄ and H₂ productivities are indeed boosted (*appx. B, Figure 7.20*). *In situ* DRIFTS study under the mimicking reaction condition in the additional presence of methanol manifests that carbonate species can be decomposed/transformed (*appx. B, Figure 7.21*) and the function of methanol can be understood to reactivate the surface by surface carbonate cleaning besides facilitating the formation of formates through oxidation of methanol [46].

4.4 Conclusions

Pt and Co co-catalysts uniquely impact on the activity and product selectivity of TiO₂ in the photocatalytic CO₂ reduction. Their unique roles are elucidated by *in situ* DRIFTS through temporal evolutions of surface species dynamically evolving during light on/off cycles. Decomposition of surface formate species is attributed to the origin of the transient photocatalytic activity. The high selectivity to H₂ of Pt/TiO₂ compared Co/TiO₂ and TiO₂ is explained by the function of formate/formic acid decomposition facilitated by Pt. Co/TiO₂ and TiO₂ show similar product selectivities, although steady-state H₂ production is only observed for TiO₂ due to the blocking of surface sites, i.e. disabled access of water to the active sites, by bicarbonate formation on Co/TiO₂. Increased carbonate formation over the catalyst surface is identified as the major cause of surface site blocking, explaining the gradual deactivation of photocatalysts.

Bibliography

1. Wang, W.-N., et al. *Aerosol and Air Quality Research*, 2014. **14**(2): p. 533-549.
2. Nikokavoura, A. and C. Trapalis. *Applied Surface Science*, 2017. **391**: p. 149-174.
3. Álvarez, A., et al. *ChemPhysChem*, 2017. **18**(22): p. 3135-3141.
4. Dhakshinamoorthy, A., et al. *Energy & Environmental Science*, 2012. **5**(11): p. 9217-9233.
5. Olivo, A., et al. *Energies*, 2017. **10**(9).
6. Mizuno, T., et al. *Journal of Photochemistry and Photobiology A: Chemistry*, 1996. **98**(1): p. 87-90.
7. Galli, F., et al. *Applied Catalysis B: Environmental*, 2017. **200**: p. 386-391.
8. Tseng, I.H., W.-C. Chang, and J.C.S. Wu. *Applied Catalysis B: Environmental*, 2002. **37**(1): p. 37-48.
9. Bazzo, A. and A. Urakawa. *ChemSusChem*, 2013. **6**(11): p. 2095-2102.
10. Liu, L., et al. *Chemical Communications*, 2013. **49**(35): p. 3664-3666.
11. Li, Y., et al. *Applied Catalysis B: Environmental*, 2010. **100**(1): p. 386-392.
12. Litter, M.I. and J.A. Navío. *Journal of Photochemistry and Photobiology A: Chemistry*, 1996. **98**(3): p. 171-181.
13. Liu, L., et al. *The Journal of Physical Chemistry C*, 2017. **121**(1): p. 490-499.
14. Maruo, Y.Y., T. Yamada, and M. Tsuda. *Journal of Physics: Conference Series*, 2012. **379**(1): p. 012036.
15. Park, H., et al. *Journal of Photochemistry and Photobiology C: Photochemistry Reviews*, 2013. **15**: p. 1-20.
16. Daghbir, R., P. Drogui, and D. Robert. *Industrial & Engineering Chemistry Research*, 2013. **52**(10): p. 3581-3599.
17. Indrakanti, V.P., J.D. Kubicki, and H.H. Schobert. *Energy & Environmental Science*, 2009. **2**(7): p. 745-758.
18. Ni, M., et al. *Renewable and Sustainable Energy Reviews*, 2007. **11**(3): p. 401-425.
19. Linsebigler, A.L., G. Lu, and J.T. Yates. *Chemical Reviews*, 1995. **95**(3): p. 735-758.
20. Osterloh, F.E. *Chemistry of Materials*, 2008. **20**(1): p. 35-54.
21. Habisreutinger, S.N., L. Schmidt-Mende, and J.K. Stolarczyk. *Angewandte Chemie International Edition*, 2013. **52**(29): p. 7372-7408.
22. Ola, O. and M.M. Maroto-Valer. *Applied Catalysis A: General*, 2015. **502**: p. 114-121.
23. Voronov, A., et al. *Analytica Chimica Acta*, 2014. **840**: p. 20-27.
24. Monakhova, Y.B., et al. *Journal of Analytical Chemistry*, 2011. **66**(4): p. 351-362.
25. Jaumot, J., A. de Juan, and R. Tauler. *Chemometrics and Intelligent Laboratory Systems*, 2015. **140**: p. 1-12.
26. Barshad, Y., X. Zhou, and E. Gulari. *Journal of Catalysis*, 1985. **94**(1): p. 128-141.
27. Panagiotopoulou, P., et al. *Journal of Catalysis*, 2006. **240**(2): p. 114-125.
28. Stakheev, A.Y., et al. *Journal of Catalysis*, 1997. **169**(1): p. 382-388.
29. Busca, G., et al. *Applied Catalysis*, 1985. **14**: p. 245-260.
30. Hadjiivanov, K.I. and D.G. Klissurski. *Chemical Society Reviews*, 1996. **25**(1): p. 61-69.

Chapter 4

31. Hadjiivanov, K., et al., *FT-IR Spectroscopic Study of NH₃ and CO Adsorption and Coadsorption on TiO₂ (Anatase)*, in *Zeitschrift für Physikalische Chemie*. 1994. p. 281.
32. Liao, L.F., et al. *The Journal of Physical Chemistry B*, 2002. **106**(43): p. 11240-11245.
33. Bianchi, D., et al. *Applied Catalysis A: General*, 1994. **112**(2): p. 219-235.
34. Guglielminotti, E. *Langmuir*, 1990. **6**(9): p. 1455-1460.
35. Kondo, J., et al. *Journal of the Chemical Society, Faraday Transactions 1: Physical Chemistry in Condensed Phases*, 1988. **84**(2): p. 511-519.
36. Iida, H. and A. Igarashi. *Applied Catalysis A: General*, 2006. **298**: p. 152-160.
37. Panagiotopoulou, P. and D.I. Kondarides. *Journal of Catalysis*, 2008. **260**(1): p. 141-149.
38. Bando, K.K., et al. *Applied Catalysis A: General*, 1997. **165**(1): p. 391-409.
39. Alexeev, O.S., et al. *The Journal of Physical Chemistry B*, 2005. **109**(49): p. 23430-23443.
40. Chen, T., et al. *Chinese Journal of Catalysis*, 2008. **29**(2): p. 105-107.
41. He, H., P. Zapol, and L.A. Curtiss. *Energy & Environmental Science*, 2012. **5**(3): p. 6196-6205.
42. Tan, S.S., L. Zou, and E. Hu. *Catalysis Today*, 2008. **131**(1): p. 125-129.
43. Wang, Y., et al. *Journal of Catalysis*, 2016. **337**: p. 293-302.
44. Cats, K.H. and B.M. Weckhuysen. *ChemCatChem*, 2016. **8**(8): p. 1531-1542.
45. Li, C. and P.C. Stair. *Catalysis Today*, 1997. **33**(1): p. 353-360.
46. Whiting, G.T., et al. *ACS Catalysis*, 2015. **5**(2): p. 637-644.

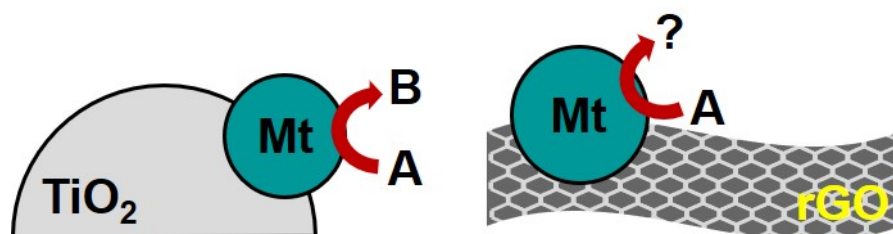
Reaction mechanism of modified TiO₂ with promoters

Chapter 4

5.

Electrochemical investigations of modified TiO_2 with promoters

Decoupling of Pt and Co co-catalyst functions investigated by electrochemical methods



5.1 Introduction

Photocatalytic water splitting and CO₂ photoreduction reactions have been studied using heterogeneous materials such as TiO₂ as an alternative approach to obtain H₂ and chemical fuels [1]. However, due to the low catalytic efficiency of bare TiO₂, promoters are often added to improve the charge carrier (electron-hole) separation upon light absorption (as explained in [chap. 1, section 1.2.2](#)) and surface charge transfer [2-4]. Besides metals or metal oxides promoters, there are other existing modifications that can improve semiconductor performance, like the addition of carbon compounds, in particular reduced graphene oxide, which has attracted great attention in photocatalytic applications due to its unique electronic properties, flexibility, and large surface area [5]. Graphene oxide (GO) is a promising carbon material for the preparation of photoactive composites because of its easy synthesis process, from the chemical oxidation of graphite by using the Hummers and Offeman method [6], and easy transformation to reduced graphene oxide (rGO). Several references in the literature reported the benefits of deposition of rGO on TiO₂ [7-9] to serve as an electron acceptor and hence minimizing electron-hole recombination within the TiO₂ semiconductor [10, 11]. Nevertheless, the conversion efficiencies for TiO₂/rGO composites are still low because rGO extracts TiO₂ photoelectrons interfacially [12], and to further enhance its performance, the addition of metal nanoparticles such as Au [13, 14], Ag [15], and Pt [12] is required. The synergetic effects between the metals and TiO₂ and/or graphene are beneficial for the photocatalytic activity, due to enhanced electron mobility as shown in [Figure 5.1](#) [16, 17]. Moreover, photocatalyst design can be tuned by the selective deposition of metal particle (Mt) onto rGO-TiO₂ (Mt/rGO-TiO₂) or rGO onto Mt/TiO₂ (rGO-Mt/TiO₂), or promoters in both rGO and TiO₂ (Mt/TiO₂-Mt/rGO), depending on the deposition method (e.g. impregnation or photodeposition) or steps followed during synthesis (one layer component or more) [18].

Electrochemical investigations of modified TiO_2 with promoters

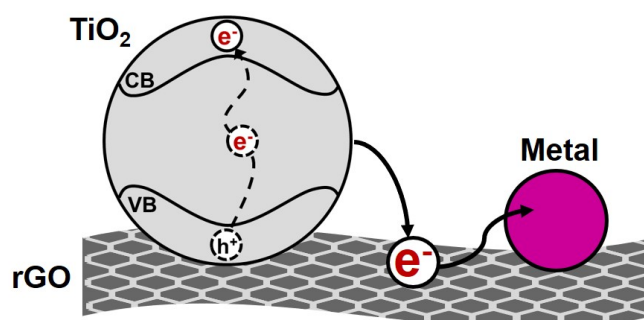


Figure 5.1. Scheme of electron mobility on Mt/rGO- TiO_2 composite with supported metal nanoparticles.

Despite the excellent properties of rGO, metal loading is still required and thus understanding the interaction between semiconductors and metal, e.g., the formation of Schottky barrier [19], is fundamental. Moreover metal promoters can also act as catalytic active sites, influencing the product selectivity (as shown in [chap. 4, section 4.3.1](#)) i.e., Pt was found to act as catalytic site for H_2 formation in gas-phase CO_2 reduction reaction [20], whereas Co on TiO_2 suppressed H_2 formation, thus it is very important to elucidate the role of co-catalysts to understand photocatalytic reaction mechanisms. Alternatively, direct loading of metal particles (promoters with semiconductors, i.e. Mt/ TiO_2) to rGO (without semiconductor, Mt/rGO) can be used to independently study the function of co-catalysts over redox reactions, thus later photocatalytic systems can be designed rationally. Electrochemical characterization techniques are employed to assess the properties of these materials, so the roles of metal/semiconductor and metal/rGO can be studied separately.

Based on the DRIFTS studies performed in [Chapter 4](#) where Pt and Co modified TiO_2 showed different reactive chemical surface species those affecting the selectivity (CH_4 or H_2) of CO_2 photoreaction reaction, here we aim to investigate Pt and Co promoters decoupled (with rGO) and coupled with TiO_2 by electrochemical techniques to get insights into the co-catalytic roles in the hydrogen evolution and oxygen evolution reactions to rationally design a suitable photocatalyst material for water splitting and CO_2 reduction reaction. However, due to the complexity of CO_2 photoreduction reaction, water splitting reaction was firstly studied since the reaction conditions are simplified (e.g. aqueous electrolytes, less amount of sample) and can be performed in solution without the presence of sacrificial agents.

5.2 Experimental

5.2.1 Materials and electrodes preparation

Pt and Co modified TiO₂ materials (Pt/TiO₂ and Co/TiO₂) were prepared by impregnation method as explained in *chap. 2, section 2.1.2*. The loading of metals was 0.2 wt% based on the weight of metal respect to TiO₂ (P25, Degussa).

Reduced graphene oxide (rGO) was synthesised from graphite powder. First, the graphite powder was mixed with H₂SO₄/HNO₃ (Sigma Aldrich) under stirring for 1 h in an ice bath, then KMnO₄ (Sigma Aldrich) was added slowly under stirring for an additional 1 h. The solution was connected to a reflux system at 310 K for 30 min, and water is added slowly and heated to 371 K for another 15 min. Finally, 100 mL of warm water and H₂O₂ (30 wt% in H₂O, Sigma Aldrich) are added slowly to oxidize the graphite, and the product was recovered by centrifuge and washed with warm water. Graphene oxide (GO) is then reduced in water and NaBH₄ (1:8) at 353 K. Reduced graphene oxide is centrifuged and washed with water, and finally dried at 333 K. If metal (Pt or Co) is loaded onto rGO, the metal addition is performed before the reduction of graphene oxide. rGO-TiO₂ composite was prepared by UV-assisted photoreduction method, mixing GO suspension with TiO₂ solution of 50% v/v methanol (1 g L⁻¹). After purging the mixture with N₂ for 30 min, it was irradiated by Xe(Hg) lamp (Newport) for 1 h under continuous stirring and purging. Then, metals can be photodeposited to rGO-TiO₂ composite by photodeposition (2 wt% metal loading with respect).

1 mg of Mt/rGO (Mt = Pt or Co) were dissolved in 0.9 mL of methanol and 0.1 mL of Nafion in the ultrasound bath, Nafion is used to ensure the particles adhesion to the carbon surface at the rotating disk electrode (RDE). The preparation of electrodes consisted of two steps, first the carbon electrode surface was cleaned with a mesh and aluminium powder, and further washed with water. Then 2 µL of the suspension (Mt/rGO) was dropcasted to the centre of the RDE and dry at 333 K, this last step was repeated 3 times until all the carbon surface was covered.

Furthermore, fluorinated tin oxide (FTO) electrodes were prepared by dropcasting a suspension of 10 mg of sample (Mt/TiO₂) in 2.5 mL of ethanol (4 mg mL⁻¹

1). The deposition of semiconductor materials was performed on a heating plate at 313 K, repeated 5 times by deposition of 0.5 mL each time (5 repetitions in total).

5.2.2 Reaction setup

Water splitting reaction was performed to study the materials performance in a liquid-phase reactor setup slightly different than the one presented in [chap. 2, section 2.2](#). The reactor consisted of a three-neck round-bottom flask connected to a gas supply with 40 mg of photocatalyst dispersed in 40 mL of pure water (**Figure 5.2**). Ar was used as carrier gas to analyse H₂, and He was used to check O₂ concentration. The online gas analysis was performed with a GC-8A (Shimadzu) equipped with molecular sieve 5A column (Restek) and thermal conductivity detector (TCD). UV-visible light was used as irradiation source and the light intensity was measured to be 0.6 W (Newport).

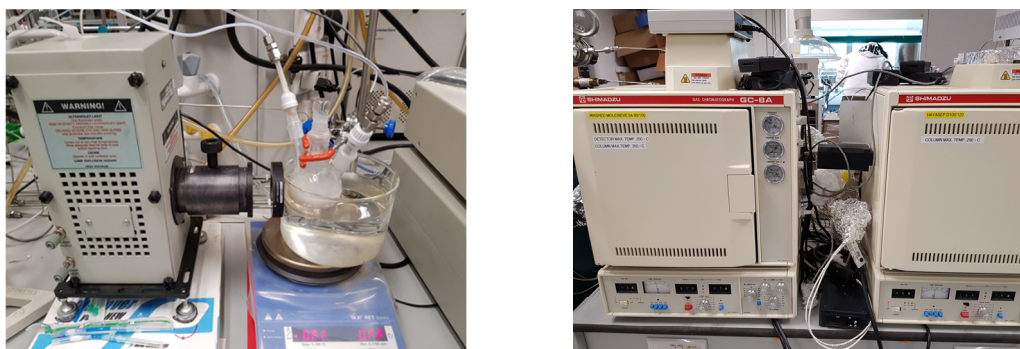


Figure 5.2. (left) alternative water splitting reactor setup and (right) Shimadzu GC.

5.2.3 Electrochemical characterization techniques

Rotating disk electrode (RDE) and photoelectrochemical cell (PEC) were employed, the basics of both techniques were explained in [chap. 2, section 2.4](#). Three electrode configuration consisting of a Ag/AgCl reference electrode, Pt as counter electrode, and corresponding working electrode were used. RDE measurements were performed for Mt/rGO materials, recording linear sweep voltammetry from 1.5 to -0.8 V vs. RHE (0.02 V s^{-1}) for hydrogen evolution reaction (electrolyte saturated with N₂) and oxygen reduction reactions (electrolyte saturated with O₂). The potential direction was inverted from 0.8 to 2.0 V vs. RHE to study water oxidation reactions with electrolyte saturated in N₂ (0.02 V s^{-1}). Onset potentials were taken at the intersection

of the current density change in the current vs. potential (I - V) curves. The number of electrons transferred for reduction and oxidation reactions was calculated from the Koutecky-Levich equation (*chap. 2, section 2.4.1*) at specific potentials. Additionally, PEC configuration was used to evaluate the performance of Mt/TiO_2 electrodes under irradiation (i.e. chopping mode) for oxidation reactions from -0.4 to 1.6 V vs. RHE.

5.3 Results and discussion

5.3.1 Photocatalytic water splitting with TiO_2 modified materials

Hydrogen evolution from photocatalytic water splitting reaction was compared for Pt- and Co-modified TiO_2 and TiO_2 -rGO composite. In pure water, H_2 evolution was measured for the Pt-containing photocatalysts, but H_2 could not be detected for Co promoted ones (**Figure 5.3**). Hence, sacrificial donor (e.g., ethanol) was added to facilitate the hydrogen evolution reaction. In all cases, the tested materials show stable H_2 formation over 4 h under irradiation, as evident from the linear rate of H_2 production with reaction time (**Figure 5.3**). While linear H_2 formation is expected given the unlimited water reagent, the linear evolution observed for the case of ethanol addition indicates the excess of sacrificial donor, at least within the first hour of reaction. In any case, the comparison between Pt/ TiO_2 (**Figure 5.3-a**) and Co/ TiO_2 (**Figure 5.3-b**) in water/ethanol reveals faster formation of H_2 in the presence of Pt than Co, confirming the more efficient role of Pt in promoting Schottky-barrier charge separation and/or co-catalytic water reduction as previous discussed (*chap. 4, section 4.3.1*) [21, 22]. Moreover, the rate of H_2 produced with Pt/ TiO_2 photocatalyst is $21 \text{ mL } H_2 \text{ h}^{-1} \text{ g}_{TiO_2}^{-1}$ which is superior to the reported activity of similar Pt loading by Abe *et al.* ($3.5 \text{ mL } H_2 \text{ h}^{-1} \text{ g}_{TiO_2}^{-1}$) [23], however, it is a tricky comparison since illumination sources used on their experiment compared to the one here have different light intensity and emission spectra. Similarly, H_2 evolution obtained from Co/ TiO_2 (0.2 wt% metal loading) in water/ethanol was higher ($588 \text{ mmol } H_2 \text{ h}^{-1} \text{ g}_{Co}$) than others reported in literature ($248 \text{ mmol } H_2 \text{ h}^{-1} \text{ g}_{Co}$) [24]. And so, high rates of H_2 evolution were successfully achieved with Pt/ TiO_2 and Co/ TiO_2 .

Attempt to evaluate the photocatalytic oxygen evolution activity was carried out by adding 0.01 M $AgNO_3$ as sacrificial electron acceptor. Quantification of molecular

Electrochemical investigations of modified TiO₂ with promoters

oxygen was very challenging due to the low sensitivity of TCD towards O₂ and the possible formation of peroxy-species in solution, which are even more difficult to detect [25]. Nevertheless, metals such as Pt are reported to participate in the formation of water from the back reaction between H₂ and O₂ [26]. Despite that, O₂ was detected in the presence of cobalt whereas Pt/TiO₂ did not show formation of O₂. This confirms the more active role Co as the oxygen evolution co-catalyst or the lower activity of Co for the backward reaction.

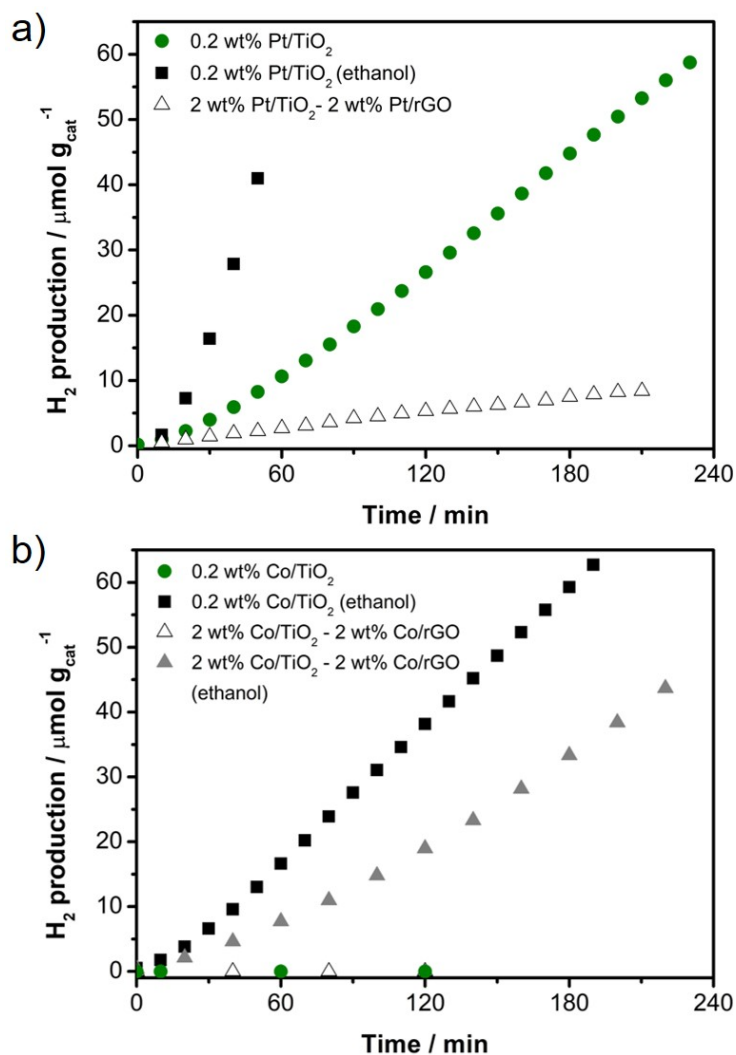


Figure 5.3. Cumulative photocatalytic H₂ production for pure water and water/ethanol mixture (10 % vol ethanol) for **a)** Pt/TiO₂ and **b)** Co/TiO₂. Black squares for Mt/TiO₂ in the presence of ethanol, Pt/TiO₂ in pure water (green), and triangles for Mt/TiO₂-Mt/rGO. GC injections were performed every 10 min under Ar continuous flow.

Interestingly, the H₂ concentration substantially decreased when Pt is loaded on both TiO₂ and rGO, i.e., 2% Pt/TiO₂-2% Pt/rGO (**Figure 5.3-a**). This could be due

Chapter 5

to the non-optimal amount of metal loading. Nevertheless, the Pt/TiO₂-Pt/rGO has stable water splitting activity and can be a potential material for studying CO₂ photoreduction. Likewise, the deposition of Co on both TiO₂ and rGO, i.e., 2% Co/TiO₂-2% Co/rGO shows lower hydrogen evolution activity compared to Co/TiO₂ in the presence of sacrificial agent. H₂ was not formed without electron donor in solution, thus cobalt promoter might not act as hydrogen evolution site. To further verify the co-catalytic roles of Co and Pt, we present the electrochemical investigation below.

5.3.2 Redox reactions for Pt and Co decoupled from TiO₂ (RDE)

5.3.2.1 Hydrogen evolution reaction (HER) and oxygen reduction reaction (ORR)

The Pt and Co supported on rGO were characterized using a rotating disk electrode (RDE) to study their co-catalytic roles as redox active sites. First, *I-V* curves for Pt/rGO and Co/rGO were evaluated for the water reduction (to form hydrogen) in N₂-saturated electrolyte solution (**Figure 5.4-a**). The addition of metals to rGO decreases the rGO overpotential for HER, as reported by Nguyen *et al.* [27]. Pt/rGO shows an onset potential of -0.16 V vs. RHE for hydrogen evolution, which is much lower than that for Co/rGO (onset potential of -1.0 V vs. RHE), thus elucidating that Pt is more reactive than Co as co-catalyst for HER. The obtained onset potential for Pt is lower (-0.16 V vs. RHE) than -0.46 V vs. RHE reported by Nguyen [27]. The Pt amount (2 wt%) used in the current work was based on the Pt loading optimized previously by Gong and Teoh [18], whereas in Nguyen's work, much more Pt than rGO was used (4 mg Pt for 1.5 mg of GO). On the other hand, Co/rGO onset potential is higher than the reported by Fei *et al.* [28], and although, similar metal loading was used (i.e. 2 wt%), the amount of sample loaded onto the working electrode was 3 times higher (0.283 mg cm⁻²) than the used for this work (0.085 mg cm⁻²) which will affect the electrode performance.

From the Koutecky-Levich plot (**Figure 5.4-b** and **5.4-c**), the number of electrons transfer, *n*, was estimated to be ~2, which corresponds (2H⁺ + 2e⁻ → H₂) for Pt, whereas no electrons were possible to be calculated for Co sample. The formation of H₂ for Pt/rGO confirms the role of Pt acting as hydrogen evolution catalyst as previously discussed in the water splitting photocatalytic results (**Figure 5.3-a**).

Electrochemical investigations of modified TiO₂ with promoters

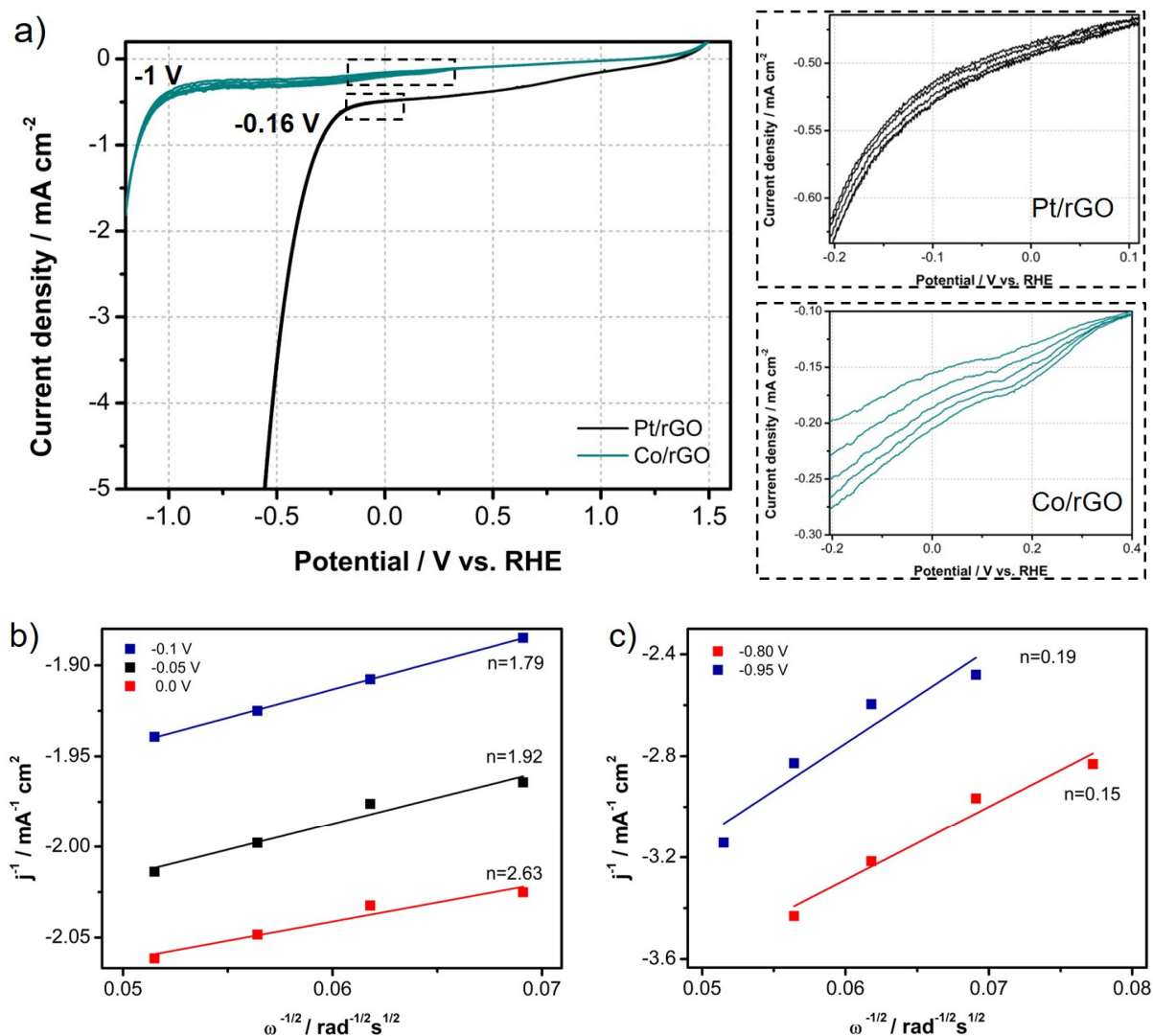


Figure 5.4. a) Hydrogen evolution reaction after N₂ purging the electrolyte solution (Na₂SO₄ 0.2 M, pH 7) for Pt/rGO (black) and Co/rGO (dark cyan) from 1.5 to -0.8 V vs. RHE (0.02 V s⁻¹) with rotating disk speeds (rpm) from 100 to 3600 rpm. Calculated electron transferred from b) Pt/rGO at three potentials 0.75 V (black), 0.80 V (red), and 0.85 V (blue) vs. RHE, and c) Co/rGO at -0.8 V (red) and -0.95 V (blue) vs. RHE.

Oxygen reduction reaction (ORR) was measured for the same materials with O₂ saturated electrolyte. Oxygen can be directly reduced to water involving four-electron or through peroxide intermediate species with two-electron reduction process (Figure 5.5-b) [29]. Pt and Co modified TiO₂ have comparable current densities in O₂ (Figure 5.5-a) and N₂ (Figure 5.4-a) saturated electrolytes, however, the onset potentials are higher in the presence of oxygen. Moreover, Pt/rGO (onset at 0.58 V vs. RHE) and Co/rGO (onset at 0.33 V vs. RHE) show large overpotentials to reduce

Chapter 5

oxygen to water (+1.23 V vs. RHE). Therefore, the number of electrons transfer was calculated to understand which intermediate species are formed for each co-catalyst. The number of transferred electrons on Pt was estimated to be ~ 2 (Figure 5.5-c), and ~ 1 for Co (Figure 5.5-d). Two-electron process indicates that oxygen reduction on Pt/rGO occurs by the formation of hydrogen peroxide species [30]. On the other hand, one-electron process for Co/rGO suggests that oxygen is reduced to hydroperoxyl species (Figure 5.5-d). Eventually, Pt and Co modified rGO required of high potentials to reduce oxygen to water.

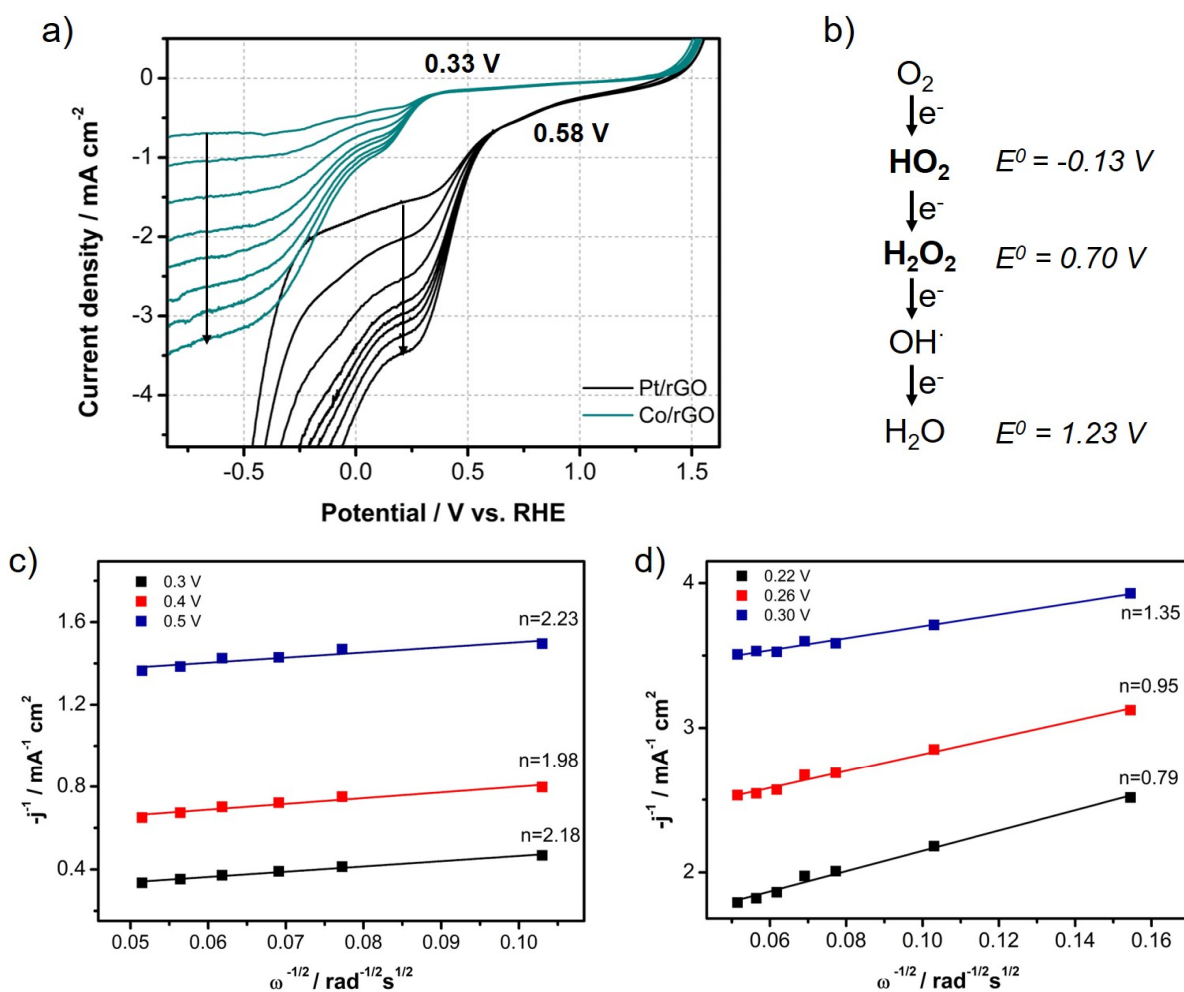


Figure 5.5. **a)** Oxygen reduction reaction after O_2 saturation of the electrolyte solution (Na_2SO_4 0.2 M, pH 7) for Pt/rGO (black) and Co/rGO (dark cyan) from 1.5 to -0.8 V vs. RHE (0.02 V s^{-1}). The arrows direction indicates the direction followed with increasing rotating disk speed (rpm) from 100 to 3600 rpm. **b)** Oxygen reduction intermediate species with corresponding standard reduction potentials (Brett, C, Electrochemistry principles, methods, and applications. 1993: Oxford University). Electron transferred calculated for **c)** Pt/rGO at 0.3 V (black), 0.4 V (red), and 0.5 V (blue) vs. RHE, and **d)** Co/rGO at 0.22 V (black), 0.26 V (red), and 0.30 V (blue) vs. RHE.

5.3.2.2 Oxygen evolution reaction (OER)

Water oxidation was then studied for Pt/rGO and Co/rGO where it is elucidated that both co-catalysts are capable of water oxidation (**Figure 5.6-a**). Moreover, like for the hydrogen evolution reaction, the overpotential required with Pt (onset at 1.70 V vs. RHE) is lower than for Co/rGO (onset at 1.96 V vs. RHE), thus Pt is better catalyst to oxidize water. However, the number of electrons transfer calculated from Koutecky-Levich equation gave a value of n from 1.4 to 2.2 (**Figure 5.6-b**), indicating that intermediate oxidation species are formed (e.g. O*) from the oxidation of water rather than oxygen, since 4 electrons are required for O₂ evolution [31]. After oxidation reaction, metals could be deactivated (e.g., by corrosion) as attributed by Reier *et al.* [32], which could explain the low current density obtained with Co.

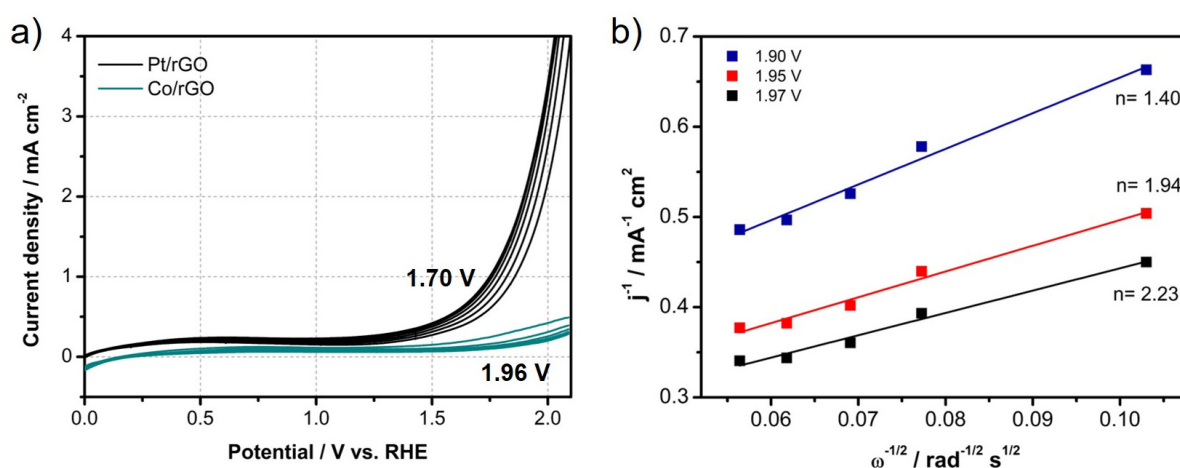


Figure 5.6. **a)** Water oxidation in N₂-saturated aqueous electrolyte (Na₂SO₄ 0.2 M, pH 7) for Pt/rGO (black) and Co/rGO (dark cyan) from -0.10 to 2.09 V vs. RHE (0.02 V s⁻¹) with rotating disk speeds (rpm) from 100 to 3600 rpm. **b)** The calculated electron transfer number from Pt/rGO at three potentials 1.97 (black), 1.95 (red), and 1.90 V vs RHE (blue).

5.3.3 Water oxidation with Pt and Co modified TiO₂ (PEC)

In **Figure 5.3**, the roles of co-catalyst for HER were studied in a free suspension form, and this makes difficult to distinguish if the co-catalysts (Pt and Co) were acting as HER or OER. Although, it is reported that Pt acts as better HER due to the Schottky barrier formation (*chap. 1, Figure 1.7*) which forces Pt to be more reductive site [33-35], the role of Co is not yet clear. Further understanding of the co-catalytic role is required, thus photoelectrochemical cell was used to evaluate Pt and Co promoters

Chapter 5

by measuring anodic current under irradiation of TiO_2 , so forcing Pt and Co to act as an OER co-catalyst. Based on the above results which showed that partial water oxidation reaction can occur with the addition of Pt and Co (without TiO_2), the performance of both co-catalysts with TiO_2 semiconductor was studied. Photoinduced charge separation was measured on Pt/ TiO_2 , Co/ TiO_2 , and TiO_2 by chopping UV illumination (light on/off).

As shown in the J - V curves in **Figure 5.7**, higher photocurrent densities were measured for Pt and Co modified TiO_2 compared to bare TiO_2 . Note that the broad anodic hump for the Pt/ TiO_2 and Co/ TiO_2 is a result of increased capacitance at the metal-semiconductor interface. The existence of broad hump is independent of photoexcitation and hence does not affect the photocurrent measurements. Higher photocurrent reflects more efficient charge separation [36], and in this case, due to the more efficient hole oxidation on the electrode surface. The higher photocurrent of Pt/ TiO_2 (0.04 mA cm^{-2} at $+1.23 \text{ V vs RHE}$) compared to Co/ TiO_2 (0.004 mA cm^{-2} at $+1.23 \text{ V vs RHE}$) corroborates the earlier identification of lower onset potential of the former by RDE. The PEC results show that Pt/ TiO_2 and Co/ TiO_2 can catalyse the evolution of oxygen from water. When coupled with the earlier results on HER, we confirm that the overall photocatalytic water splitting is achieved with the assistance of the co-catalysts when combined with TiO_2 semiconductor. Depending on the spatial location of the co-catalyst or more specifically the interfacial states on which the co-catalysts are deposited, the co-catalysts may be electron and/or hole acceptors. This in turn determines whether the co-catalysts surface become HER and/or OER sites, respectively.

From **Figure 5.7**, the onset potential of the TiO_2 , or the potential where photocurrent was first detected, was measured to be -0.23 V vs. RHE . The value is comparable for Co/ TiO_2 (-0.30 V vs. RHE) and Pt/ TiO_2 (-0.26 V vs. RHE) and is basically the quasi-Fermi level of TiO_2 [36]. Being an n-type semiconductor, the measured quasi Fermi-level is close to the conduction band edge of the TiO_2 . Given the bandgap of 3.2 eV for TiO_2 , the valence band edge can be estimated to be 2.8 V vs. RHE . At the conduction band edge, the RDE-derived kinetic currents for HER ($j_{k,\text{HER}}$) were estimated from j_m at the highest rotation speed (i.e. 3600 rpm) which are

-0.67 and -0.21 mA cm⁻² for Pt and Co co-catalysts, respectively. Because of the limitation of the maximum anodic potential that can be applied on the glassy carbon electrode, we could only approximate the kinetic currents for OER ($j_{k,OER}$, also estimated from j_m at 3600 rpm) at 2.10 V vs. RHE. The $j_{k,OER}$ values are 6.05 and 0.29 mA cm⁻² for Pt and Co co-catalysts, respectively. In the case where both Pt and Co are ambivalent co-catalysts, the ratios of $j_{k,HER} : j_{k,OER}$ reflect the fraction of the respective co-catalysts that act as catalytic reductive and oxidative sites during the water splitting reaction. In this case, the $j_{k,HER} : j_{k,OER}$ was found to be 0.11 for Pt co-catalyst and 0.73 for Co co-catalyst, these ratios elucidate higher overpotential obtained for OER (**Figure 5.6-a**) compared to HER (**Figure 5.4-a**). This is the first time that such approximation has ever been established. The ratios are based solely on their co-catalytic activities and discount the increased fraction of electrons that is trapped on the co-catalyst as a result of Schottky barrier formation, thus catalysing HER and leaving only a small fraction to catalyse OER.

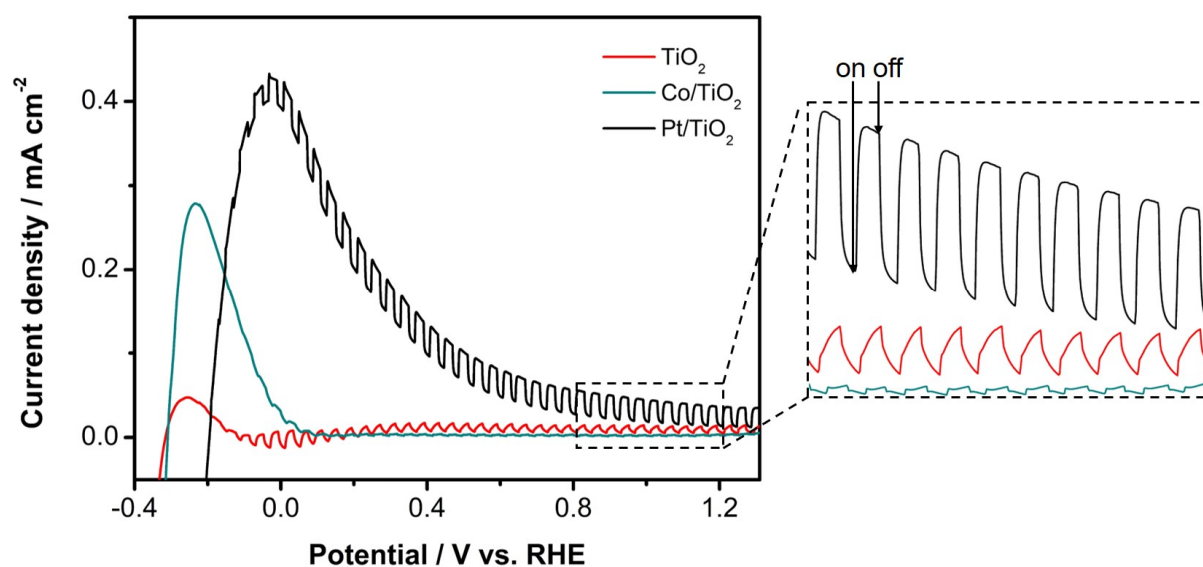


Figure 5.7. LSV for TiO₂ (red), Pt/TiO₂ (black), Co/TiO₂ (cyan) deposited onto FTO; measured under irradiation with UV-vis light (fibre-based light from UV-Consulting Pechl) in chopping mode (repeated light on-off every 2 sec, as shown in the zoomed region). 0.2 M Na₂SO₄ was used as electrolyte solution, and Ag/AgCl and Pt as reference and counter electrodes, respectively.

5.4 Conclusions

Photocatalytic water splitting tests revealed that H₂ evolution was faster in presence of Pt than Co on TiO₂, confirming the role of Pt as hydrogen evolution site.

Chapter 5

Pt and Co promoters were decoupled from TiO₂ and further studied supported on rGO by electrochemical methods. As expected, semi-redox reactions evaluated by RDE confirmed Pt as a more reactive co-catalyst for HER compared to Co, and better catalyst for water oxidation, although water was not fully oxidized to O₂. Furthermore, we clarified the role of co-catalyst (especially of Co) by performing PEC measurements of the promoters coupled to TiO₂ and forcing both Pt and Co to act as OER catalyst. Pt/TiO₂ and Co/TiO₂ successfully catalysed oxygen evolution reaction, as opposed to the photocatalytic water splitting tests, Co resulted to be less active than Pt. Moreover, an approximation of the co-catalytic reactivity towards HER and OER ($j_{k,HER} : j_{k,OER}$) was established from RDE results, such ratios could be used only if co-catalysts were tested in solution for the water splitting reaction. Nevertheless, when co-catalysts are in contact with semiconductors the formation of Schottky barrier favours electron trapping to the co-catalyst, thus promoters mainly catalyse HER. It is challenging to determine the ratio of active sites for HER and OER when Pt or Co are supported on TiO₂. However, PEC results revealed Pt (on Pt/TiO₂) as more efficient OER than HER.

Bibliography

1. Hernández-Alonso, M.D., et al. *Energy & Environmental Science*, 2009. **2**(12): p. 1231-1257.
2. Habisreutinger, S.N., L. Schmidt-Mende, and J.K. Stolarczyk. *Angewandte Chemie International Edition*, 2013. **52**(29): p. 7372-7408.
3. Linsebigler, A.L., G. Lu, and J.T. Yates. *Chemical Reviews*, 1995. **95**(3): p. 735-758.
4. Osterloh, F.E. *Chemistry of Materials*, 2008. **20**(1): p. 35-54.
5. Kamat, P.V. *The Journal of Physical Chemistry Letters*, 2010. **1**(2): p. 520-527.
6. Hummers, W.S. and R.E. Offeman. *Journal of the American Chemical Society*, 1958. **80**(6): p. 1339-1339.
7. Bhanvase, B.A., T.P. Shende, and S.H. Sonawane. *Environmental Technology Reviews*, 2017. **6**(1): p. 1-14.
8. Ge, M., et al. *International Journal of Hydrogen Energy*, 2017. **42**(12): p. 8418-8449.
9. Štengl, V., D. Popelková, and P. Vláčil. *The Journal of Physical Chemistry C*, 2011. **115**(51): p. 25209-25218.
10. Zhang, Q., et al. *Catalysis Today*, 2016. **274**: p. 8-14.
11. Li, L., et al. *ACS Applied Materials & Interfaces*, 2016. **8**(13): p. 8536-8545.
12. Gong, X., et al. *Chemistry of Materials*, 2016. **28**(22): p. 8082-8118.
13. Zhou, X., et al. *The Journal of Physical Chemistry C*, 2009. **113**(25): p. 10842-10846.
14. Huang, X., et al. *Nature Communications*, 2011. **2**: p. 292.
15. Lightcap, I.V., T.H. Kosel, and P.V. Kamat. *Nano Letters*, 2010. **10**(2): p. 577-583.
16. Rather, R.A., S. Singh, and B. Pal. *Journal of Industrial and Engineering Chemistry*, 2016. **37**: p. 288-294.
17. Yang, Y., et al. *International Journal of Hydrogen Energy*, 2014. **39**(15): p. 7664-7671.
18. Gong, X. and W.Y. Teoh. *Journal of Catalysis*, 2015. **332**: p. 101-111.
19. Memming, R., *Semiconductor Electrochemistry*. 2001, Germany: Wiley-VCH.
20. Dhakshinamoorthy, A., et al. *Energy & Environmental Science*, 2012. **5**(11): p. 9217-9233.
21. Bamwenda, G.R., et al. *Journal of Photochemistry and Photobiology A: Chemistry*, 1995. **89**(2): p. 177-189.
22. Sato, S. and J.M. White. *Chemical Physics Letters*, 1980. **72**(1): p. 83-86.
23. Abe, T., et al. *The Journal of Physical Chemistry B*, 1999. **103**(7): p. 1119-1123.
24. Montoya, A.T. and E.G. Gillan. *ACS Omega*, 2018. **3**(3): p. 2947-2955.
25. Sayama, K. and H. Arakawa. *Journal of the Chemical Society, Chemical Communications*, 1992(2): p. 150-152.
26. Abe, R., K. Sayama, and H. Arakawa. *Chemical Physics Letters*, 2003. **371**(3): p. 360-364.
27. Nguyen, T.K., J. Yun, and Y.S. Kim. *Electrocatalytic hydrogen evolution reaction based on reduced graphene oxide:Pt nanocomposite*. in *2016 11th International Forum on Strategic Technology (IFOST)*. 2016.
28. Fei, H., et al. *Nature Communications*, 2015. **6**: p. 8668.
29. Zuluaga, S. and S. Stolbov. *The Journal of Chemical Physics*, 2011. **135**(13): p. 134702.

Chapter 5

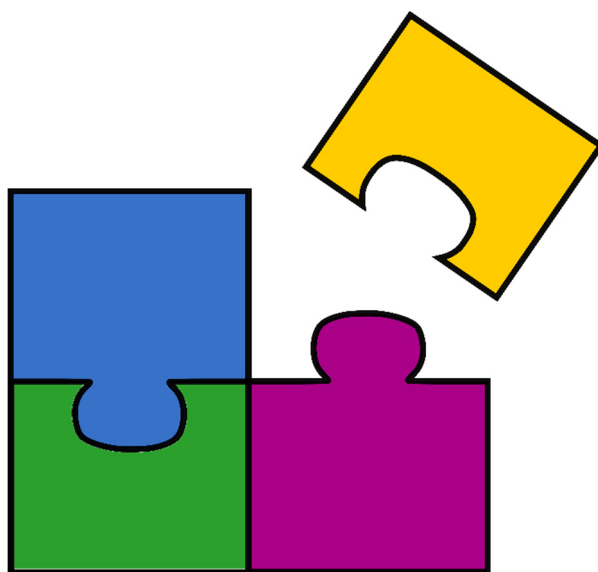
30. Yamada, H., et al. *Electrochemical and solid state letters*, 2004. **7**(12): p. 234-240.
31. Zhang, L., et al. *ACS Catalysis*, 2017. **7**(11): p. 7855-7865.
32. Reier, T., M. Oezaslan, and P. Strasser. *ACS Catalysis*, 2012. **2**(8): p. 1765-1772.
33. Nakabayashi, S., A. Fujishima, and K. Honda. *Chemical Physics Letters*, 1983. **102**(5): p. 464-465.
34. Teoh, W.Y., L. Mädler, and R. Amal. *Journal of Catalysis*, 2007. **251**(2): p. 271-280.
35. Denny, F., et al. *Journal of Molecular Catalysis A: Chemical*, 2007. **263**(1): p. 93-102.
36. Kho, Y.K., et al. *The Journal of Physical Chemistry C*, 2010. **114**(6): p. 2821-2829.

Electrochemical investigations of modified TiO₂ with promoters

Chapter 5

6.

Conclusions and outlook



6.1 Summary of thesis

CO₂ reduction and H₂O splitting reactions were evaluated under UV-vis light and continuous flow conditions in two different type of photocatalytic reactors, i.e. gas and liquid-phase, previously developed [1, 2]. Optimization of parameters such as control of temperature, reactor sealing, and sample-light distance was performed for developing a second generation of custom-made photoreactors.

Our work was based on Ga₂O₃ and TiO₂ materials. These materials are semiconductors with wide-bandgaps and high-energy light source is required to promote their electronic transitions, forcing us to work with UV-vis light. Although Ga and Ti oxides showed photocatalytic activities for H₂O splitting and CO₂ reduction reactions, their efficiencies remained low due to fast recombination of charge carriers (electron-hole) upon light excitation. Hence, Ga₂O₃ and TiO₂ photocatalysts are generally modified with metal or metal oxide particles (i.e. promoters or co-catalysts) known for trapping electrons from the semiconductor, thus enhancing the catalytic activity by decreasing the electron-hole recombination rate. From the large library of reported co-catalytic materials ranging from metals to non-metals [3], several metal/metal oxides were chosen (namely Zn, Rh, Cr, Pt, and Co) and simple wet impregnation method was employed to add those co-catalysts to the semiconductor (Zn, Rh, Cr were supported on Ga₂O₃ while Pt and Co on TiO₂). Although such metals are reported as common co-catalysts [4-8], physical aspects (e.g. metal-semiconductor interaction) and reaction mechanisms (e.g. surface chemical species under UV-vis irradiation) are not well discussed in literature. Therefore, in this work we aimed to gain deeper insights into the metal/s and photocatalyst interface and elucidate the photocatalytic reaction mechanisms of water splitting and CO₂ reduction.

In [Chapter 3](#), Zn and Rh-Cr co-catalysts were studied since they greatly influenced the photocatalytic water splitting activity of Ga₂O₃. Their synergistic function was elucidated by element selective XAS and XES. Formation of appropriate ZnGa₂O₄/Ga₂O₃ heterojunction was identified at the optimum Zn-loading (2-4 wt%). Such semiconductor interface favoured the charge transfer and separation through an optimum exposure of both materials to the excitation light, resulting in enhancement of the photocatalytic activity. Moreover, photocatalytic activity of ZnGa₂O₄ and Ga₂O₃

decreased due to the negative influence of ZnO phase formed at high Zn-loadings (≥ 20 wt%). Furthermore, the individual role of Rh-Cr was studied by means of sacrificial agents (AgNO_3), Ag poisoned Rh-Cr sites which were also identified by microscopy (STEM). The photodeposition of Ag induced an electronic structure change of Cr and Rh as evidenced by XANES, confirming the function of Rh-Cr as electron sink in water splitting reaction. Finally, the concerted actions among Rh-Cr and Zn were proven by *in situ* illumination modulation excitation XAS spectroscopy. The electronic structure of Zn ($\text{ZnGa}_2\text{O}_4/\text{Ga}_2\text{O}_3$) was slightly perturbed under irradiation; more importantly the degree of change of Zn absorption edge in the presence of Rh-Cr was boosted, indicating the communication and synergy between Zn and Rh-Cr co-catalysts deposited on Ga_2O_3 at the electronic level under photocatalytic conditions.

After a better understanding of the parameters influencing on water splitting reaction and co-catalyst/photocatalyst interface, CO_2 photoreduction was evaluated also in continuous flow but under gas-phase conditions (Chapter 4). The reaction was carried out with water-saturated CO_2 to avoid the use of sacrificial agents and to minimize the water content and thus its reduction reaction to H_2 . TiO_2 -based photocatalysts were used since our preliminary results did not show detectable catalytic activity for Ga_2O_3 materials in photocatalytic CO_2 reduction. TiO_2 is a widely reported photocatalyst from its discovery in 1972 [9], and loading of Pt on TiO_2 has been extensively studied due to the formation of Schottky barrier and an enhanced TiO_2 activity. However, there is a lack of reports about its function and also the addition of Co as promoter to TiO_2 .

Pt and Co co-catalysts had an impact on the activity and product selectivity of TiO_2 in the photocatalytic CO_2 reduction as presented in Chapter 4. CH_4 and H_2 were the only products evolved from CO_2 photoreduction under irradiation showing a transient activity, except for TiO_2 where H_2 presented steady-state activity. Formation of H_2 was enhanced in the presence of Pt whereas it was suppressed for Co/TiO_2 . The latter showed similar product selectivity to TiO_2 , indicating that different surface reactions occurred depending on presence/absence and also on the choice of co-catalyst. To gain further mechanistic insights, temporal evolution of surface species for CO_2 photoreduction reaction were evaluated by *in situ* DRIFTS. Formate species were identified as the common reactive intermediate formed over Pt/TiO_2 , Co/TiO_2 ,

Chapter 6

and pure TiO_2 , and its decomposition under UV-vis light was attributed to origin the transient photocatalytic activity. The high selectivity to H_2 of Pt/TiO_2 compared to Co/TiO_2 and TiO_2 was explained by the function of formate/formic acid decomposition facilitated by Pt. Contrastingly, Co/TiO_2 showed different bicarbonates reactivity with light, i.e. bicarbonate species disabled the access of water to Co/TiO_2 surface. Based on the DRIFTS study, we elucidated that carbonate formation over the catalyst surface is the major cause of surface site blocking, explaining the gradual deactivation of photocatalysts.

Since water is also involved in the mechanism of CO_2 reduction, the roles of Pt and Co on water splitting reaction were further studied by photocatalytic tests and electrochemical methods (Chapter 5). As depicted in the photocatalytic water splitting activity, H_2 formation was promoted for Pt/TiO_2 whereas it was not detected for Co/TiO_2 without the addition of sacrificial agents, supporting the results obtained in Chapter 4. Moreover, kinetics of hydrogen and oxygen evolution reactions, evaluated with those co-catalysts decoupled from TiO_2 (i.e. loaded on rGO) by using rotating disk electrode technique, also showed Pt as the best catalyst for water reduction and oxidation reactions. The co-catalysts ability to oxidize water was further confirmed when coupled with TiO_2 and evaluated in a PEC (photoelectrochemical cell). Pt/TiO_2 and Co/TiO_2 oxidized water more efficiently than bare TiO_2 , thus elucidating the benefits of metal loading into semiconductors. PEC results also revealed Pt as a more efficient OER than HER, Co instead resulted to be less active than Pt for both reactions.

6.2 Outlook

Investigation of photocatalytic systems under reaction conditions is always a great challenge, especially when liquids are involved in the reaction media. Water splitting reaction has been extensively studied by electrochemical methods to elucidate oxidation and reduction reactions of several types of electrodes surface [10-12]. Similarly, CO₂ photoreduction reaction in liquid has also been studied, however the requirement of sacrificial agents increases complexity when evaluating semi-redox reactions [13-15]. We have shown how infrared techniques are suitable for gaining insights into surface species involved in the CO₂ reduction under gas-phase conditions. Comparatively, chemical species formed at the electrode surface could be studied, although the reactions will take place in liquid-phase and/or in the presence of organic solvents (sacrificial agents) to enhance CO₂ solubility [16] thus making more challenging any *in situ* analysis.

In situ FTIR spectroscopy is a powerful tool to obtain real-time information about the chemical species involved in electrochemical reactions, i.e. time-resolved FTIR. Since 1980s [17], several reports showed the possibility of gaining information about adsorbates at electrode and species in solution for electrochemical reactions [18]. However, there are some limitations when studying solid/liquid interfaces (electrode/electrolyte); (i) absorption of IR light by electrolyte solution, (ii) partially loss of energy during the electrode IR reflection, and (iii) low signal-to-noise (S/N) ratio. Moreover, FTIR needs to be measured in reflection mode due to the electrode composition, where internal and external configurations have been developed. The internal reflection configuration uses attenuated total reflectance (ATR, [chap. 2, section 2.3.3](#)) where the electrocatalyst is directly deposited on the ATR crystal [19]. The IR beam is focused at back of the electrode and it is reflected, thus avoiding IR light to pass through the aqueous electrolyte solution [20, 21], but only adsorbed species can be detected and not all the type of materials can be successfully deposited on the ATR crystal. On the other hand, a thin layer of electrocatalyst is used for external reflection configuration, in this way a wide range of materials can be studied since it is not restricted by electrocatalyst deposition on the crystal [18]. Furthermore, thickness of the electrolyte layer is minimized by pressing the working electrode (inside

Chapter 6

the solution) against the IR window (CaF_2) where external reflections occur [22, 23]. However, performing reactions under flow conditions with external configurations is difficult because the working electrode needs to be removed after every measurement to ensure electrolyte mixing, whereas electrolyte solution can be passed continuously using internal configuration.

Besides the IR configuration, spectral acquisition can be performed by step-scan or rapid-scan. Step-scan mode is commonly used to study transient events because of its fast time-resolution in the nanosecond range (ns), e.g. electron transfer processes. However, the potential scan rate for studying electrochemical reactions is usually around $\sim 100 \text{ mV s}^{-1}$ thus rapid-scan technique is preferred (millisecond scale), so more reliable information of transient processes can be gained from the IR measurement [24, 25].

Based on the background of spectroelectrochemical cells, an alternative cell design using diffuse reflectance infrared Fourier transformed spectroscopy (DRIFTS) for CO_2 photoreduction reaction of modified TiO_2 with Pt and Co promoters deposited into fluorine doped tin oxide (FTO) electrode is proposed here. Cell design and measurement conditions were optimized under dark (without using irradiation), and later a new cell prototype was developed enabling electrode illumination mimicking photoelectrochemical cell principles. Pt and Co modified TiO_2 were evaluated as working electrodes half immersed in the electrolyte solution to minimize the electrolyte interferences with the IR beam.

6.2.1 Preliminary studies with spectroelectrochemical cell in diffuse reflectance mode

Custom-made cell to perform electrochemical measurements was developed in-house by 3D printer. The setup consisted of a portable IR (ARCOptix) and a small cell composed of ZnSe window and a lid to support the working, reference, and counter electrodes (**Figure 6.1**). Ag/AgCl and Pt wire were used as reference and counter electrodes, respectively. The setup was kept under N_2 atmosphere to avoid IR disturbances from CO_2 vibrations.

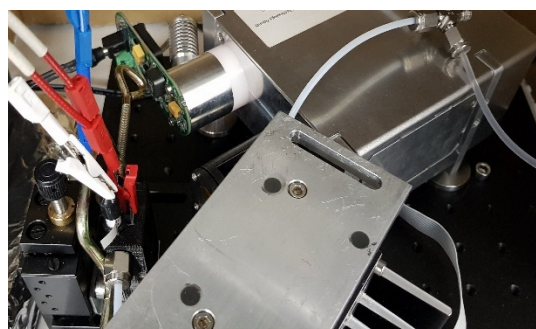
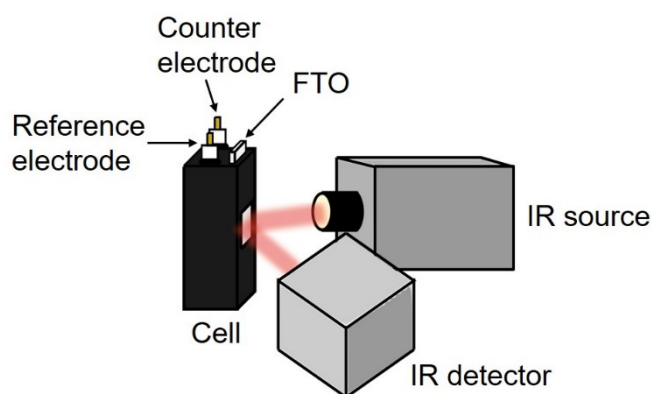


Figure 6.1. (top) Initial cell configuration for electrochemical measurement coupled with portable IR, and (bottom) setup picture.

Electrodes of TiO_2 promoted with Pt and Co were prepared following the protocol described in [chap. 5, section 5.2.1](#). FTO electrodes were immersed in a mixture of water/methanol (10 vol% of methanol), methanol was added to increase CO_2 solubility in water. IR spectra were acquired from the half part of electrode not in contact with the electrolyte solution, but spectral baseline fluctuated considerably with reaction time. For this reason, electrodes were stabilized inside the electrolyte solution for 1 h while CO_2 was bubbled through the solvent, and during this process, surface wetting of the electrode was monitored. After IR signal stabilization, linear sweep voltammetry (or cyclic voltammetry) was performed to identify potentials where redox reactions occurred ([Figure 6.2-a](#)), and then constant potentials at these values were applied while recording DRIFT spectra ([Figure 6.2-b](#) and [6.2-c](#)). Electrochemical measurements were synchronised with IR acquisition times, thus optimizing experimental conditions.

Great absorbance intensities and high S/N ratio were achieved. However, we did not obtain significant differences between the surface species adsorbed on Pt/ TiO_2

Chapter 6

and Co/TiO₂ at different potentials (e.g. spectral features after averaging spectra acquired in 5 min at 0.7 V and 1.6 V vs. RHE for Co/TiO₂ look almost the same, **Figure 6.2-d**).

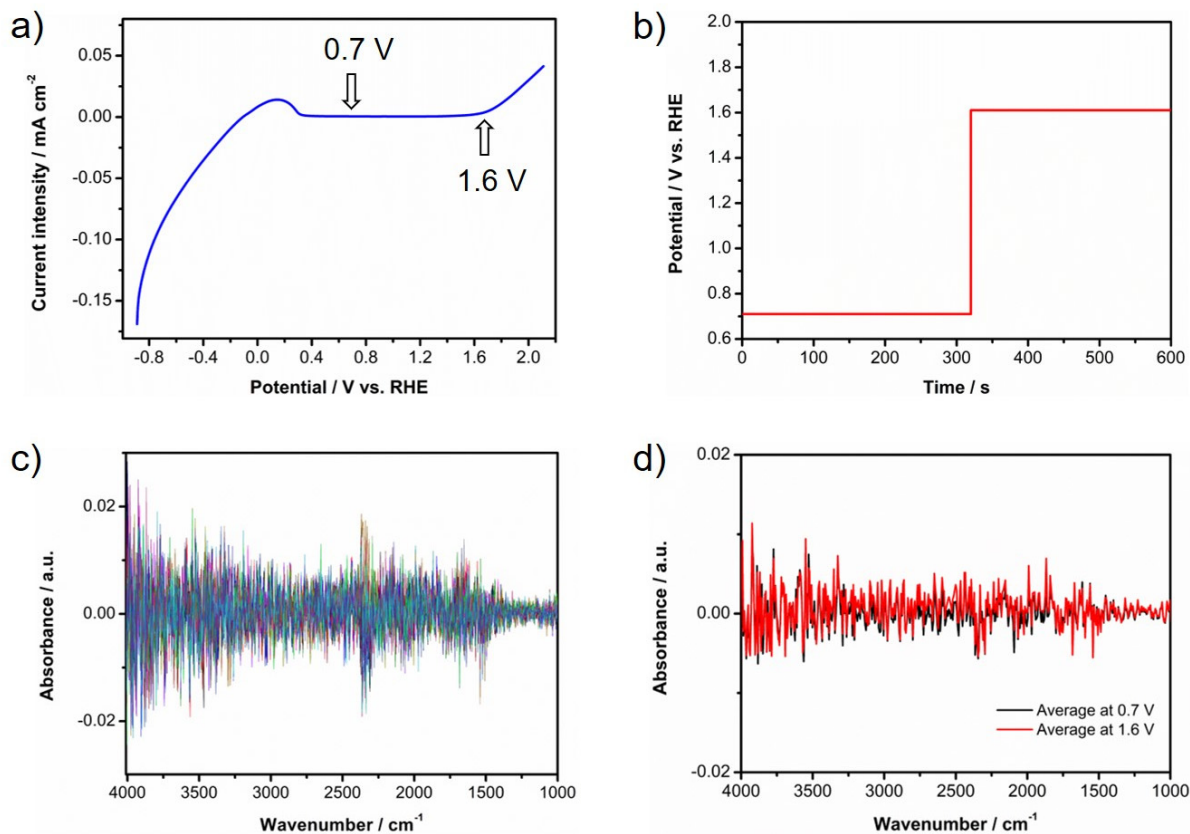


Figure 6.2. **a)** Linear sweep voltammetry from -0.9 V to 2.1 V vs. RHE for Co/TiO₂, **b)** constant potentials applied at 0.7 V and 1.6 V vs. RHE. **c)** IR spectra collected during 10 min (1 spectrum every 16 sec), with background spectrum collected from the last spectrum after electrode stabilization in the electrolyte solution, and **d)** averaged spectrum from the IR data at 0.7 V (red) and 1.6 V (black) vs. RHE.

6.2.2 DRIFTS coupled to photoelectrochemical cell

In situ irradiation can enhance photocatalyst reactivity and promote redox reactions at the electrode surface. As discussed in **Chapter 5**, reduction and oxidation reactions can be studied photoelectrochemically by chopping mode, e.g. applying constant potential to the electrode and switching light on/off [26]. This approach is a fast and reliable way of getting insights about the semiconductor behaviours and could be extended to study the role of promoters or co-catalysts in oxidation and reduction semi-reactions for photocatalytic CO₂ reduction.

Therefore, a new cell prototype was developed to couple photoelectrochemical cell with DRIFTS. Based on the setup depicted in [Figure 6.1](#), two additional windows were added to avoid the interference of UV-vis light with IR beam ([Figure 6.3](#)), the rest of elements were maintained. The two yellow windows are IR transparent (ZnSe) and the third one is transparent to UV light (quartz).

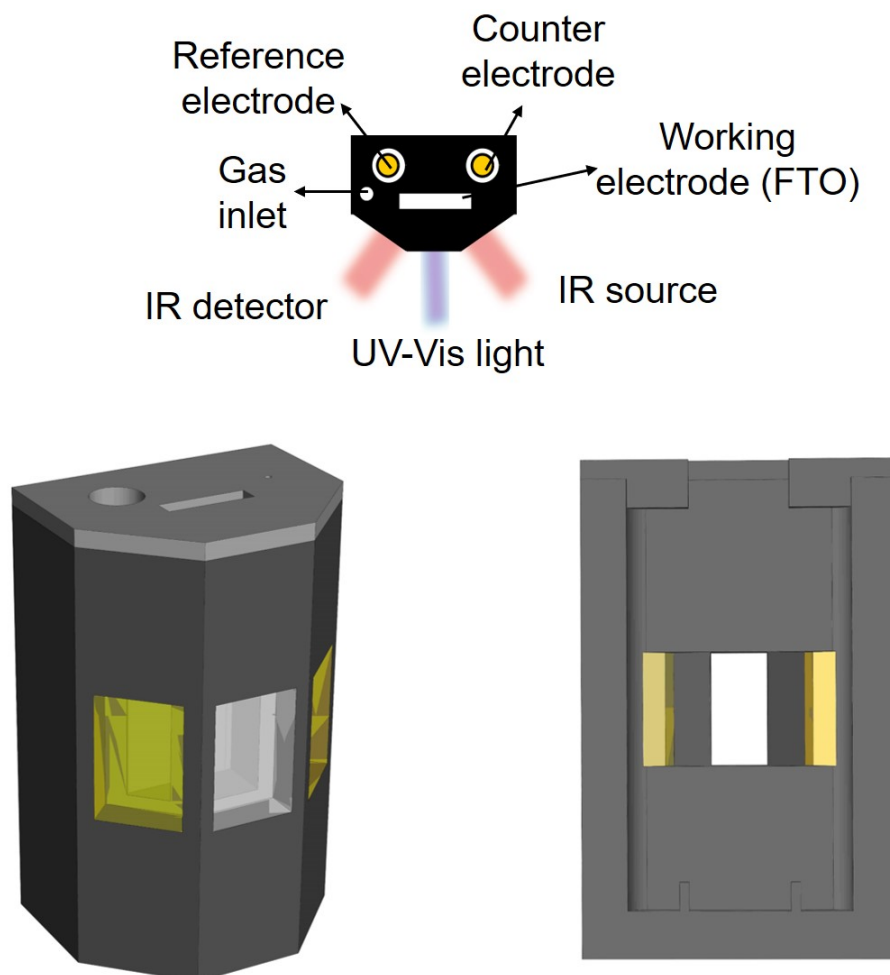


Figure 6.3. Cell prototype coupling photoelectrochemical cell with DRIFTS.

Further testing of photocatalyst/electrocatalyst materials will be performed on this new prototype. We expect to achieve significant differences among Pt and Co promoted materials for CO₂ photoreduction and obtain complementary information to the results obtained in [Chapter 4](#). Eventually, this cell configuration coupling IR, light and electrochemical methods could also be implemented to investigate other photocatalytic reactions and types of semiconductor materials.

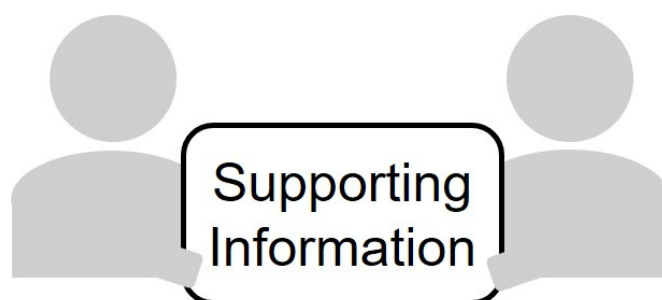
Bibliography

1. Bazzo, A. and A. Urakawa. *ChemSusChem*, 2013. **6**(11): p. 2095-2102.
2. Bazzo, A. and A. Urakawa. *Catalysis Science & Technology*, 2016. **6**(12): p. 4243-4253.
3. Liu, G., et al. *Journal of Materials Chemistry*, 2010. **20**(5): p. 831-843.
4. Chen, X., et al. *Chemical Reviews*, 2010. **110**(11): p. 6503-6570.
5. Maeda, K., et al. *Angewandte Chemie International Edition*, 2006. **45**(46): p. 7806-7809.
6. Maeda, K., et al. *Nature*, 2006. **440**: p. 295.
7. Maeda, K., et al. *The Journal of Physical Chemistry C*, 2006. **110**(26): p. 13107-13112.
8. Park, H., et al. *Journal of Photochemistry and Photobiology C: Photochemistry Reviews*, 2013. **15**: p. 1-20.
9. Fujishima, A. and K. Honda. *Nature*, 1972. **238**: p. 37.
10. Walter, M.G., et al. *Chemical Reviews*, 2010. **110**(11): p. 6446-6473.
11. Roger, I., M.A. Shipman, and M.D. Symes. *Nature Reviews Chemistry*, 2017. **1**: p. 0003.
12. Kang, D., et al. *Chemical Reviews*, 2015. **115**(23): p. 12839-12887.
13. Kumar, B., et al. *Annual Review of Physical Chemistry*, 2012. **63**(1): p. 541-569.
14. Oh, Y. and X. Hu. *Chemical Society Reviews*, 2013. **42**(6): p. 2253-2261.
15. White, J.L., et al. *Chemical Reviews*, 2015. **115**(23): p. 12888-12935.
16. Parkinson, B. *ACS Energy Letters*, 2016. **1**(5): p. 1057-1059.
17. Bewick, A. *Journal of Electroanalytical Chemistry and Interfacial Electrochemistry*, 1983. **150**(1): p. 481-493.
18. Ye, J.-Y., et al. *Nano Energy*, 2016. **29**: p. 414-427.
19. Mojet, B.L., S.D. Ebbesen, and L. Lefferts. *Chemical Society Reviews*, 2010. **39**(12): p. 4643-4655.
20. Matsui, T., et al. *Langmuir*, 2015. **31**(42): p. 11717-11723.
21. Ataka, K., T. Yotsuyanagi, and M. Osawa. *The Journal of Physical Chemistry*, 1996. **100**(25): p. 10664-10672.
22. Kanamura, K., et al. *Electrochimica Acta*, 2001. **47**(3): p. 433-439.
23. Machan, C.W., et al. *Organometallics*, 2014. **33**(18): p. 4550-4559.
24. Bellec, V., et al. *Electrochemistry Communications*, 2001. **3**(9): p. 483-488.
25. Miki, A., S. Ye, and M. Osawa. *Chemical Communications*, 2002(14): p. 1500-1501.
26. Paracchino, A., et al. *Nature Materials*, 2011. **10**: p. 456.

Chapter 6

7.

Appendices



Appendix A Supplementary Information of Chapter 3

Scanning transmission electron microscopy (STEM) was measured in annular dark-field imaging mode (HAADF) in a high-resolution FEI Tecnai F20 STEM microscope at the Catalan Institute of Nanoscience and Nanotechnology (ICN2) in Barcelona. Chemical analysis and chemical mapping were performed by energy dispersive X-ray spectroscopy (EDX) and electron energy loss spectroscopy (EELS), respectively. 4 wt% Zn-Ga₂O₃ and Rh-Cr/4wt% Zn-Ga₂O₃ materials prepared in ethanol solution and were deposited on the a TEM support grid.

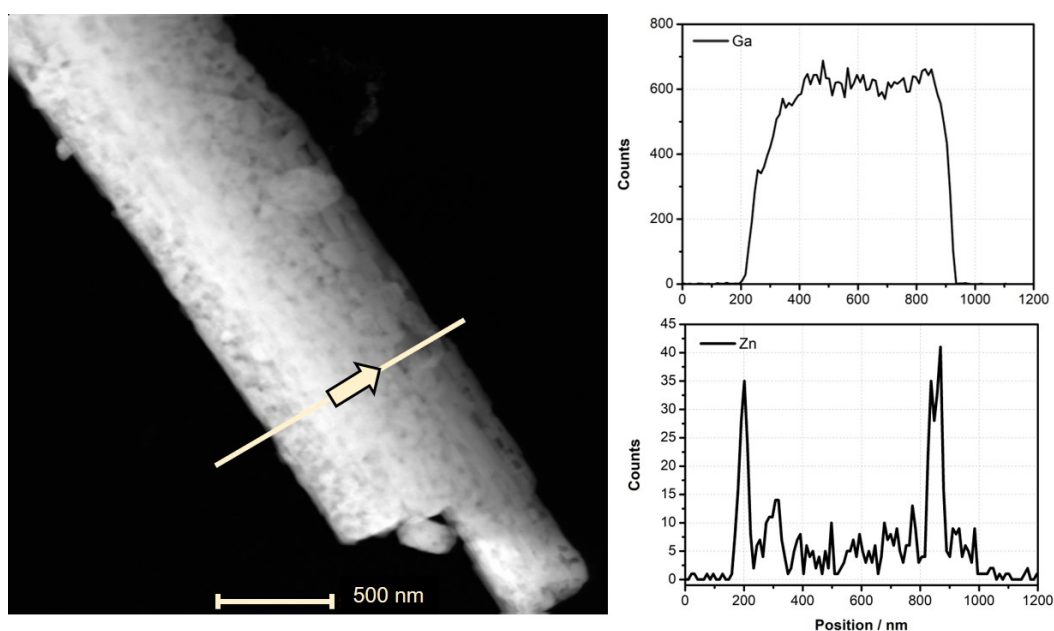


Figure 7.1. (left) STEM-HAADF image of 4 wt% Zn-Ga₂O₃ material, with the transversal line indicating where EDX was measured. (right) Elemental profiles of Ga (top) and Zn (bottom) along the transversal line.

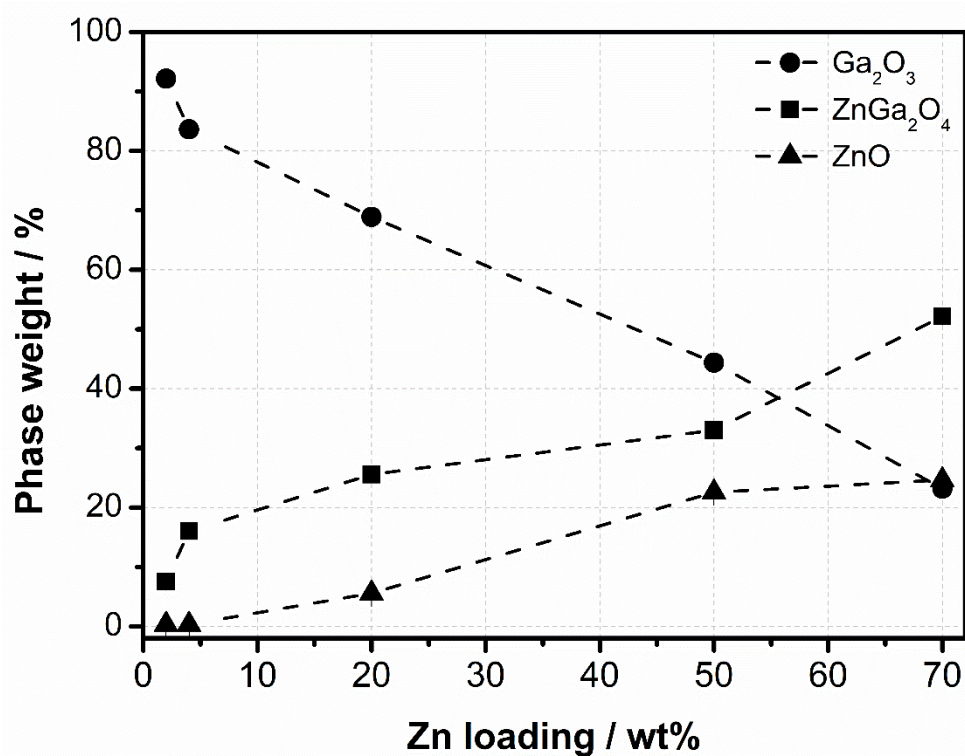


Figure 7.2. Quantitative phase analysis of the XRD data for xZn-modified Ga₂O₃ photocatalysts where x= 2, 4, 20, 50, and 70 wt% of Zn.

Appendices

The performance of density functionals PBE and PBE0 was compared, but due to the high computational cost of PBE0, PBE was applied to perform the cell optimization of the ZnO, Ga₂O₃, and ZnGa₂O₄ structures. First, the atomic positions in the corresponding cells and lattice parameters were optimized using PBE. After this, the energy calculations were performed by PBE0 to obtain more accurate DOS with the atomic positions and lattice parameters calculated above.

Table 7.1. DOS calculations details

Package			
	CASTEP		
Conditions of Cell optimization			
	ZnO	Ga ₂ O ₃	ZnGa ₂ O ₄
Functional	PBE	PBE	PBE
Energy tolerance (eV/atom)	1.00E-05	1.00E-05	1.00E-05
Max. force(eV/Å)	0.03	0.03	0.03
Max. stress (Gpa)	0.05	0.05	0.05
Max. displacement (Å)	0.001	0.001	0.001
Energy cutoff (eV)	750	800	800
K-mesh	5x5x4	5x5x2	3x3x3
SCF tolerance (eV/atom)	1.00E-06	1.00E-06	1.00E-06
Conditions of SCF by PBE0			
	ZnO	Ga ₂ O ₃	ZnGa ₂ O ₄
Functional	PBE0	PBE0	PBE0
Energy cutoff (eV)	600	600	600
K-mesh	4x4x2	4x4x2	3x3x3
SCF tolerance (eV/atom)	2.00E-06	2.00E-06	2.00E-06

The coverage or phase transformation of ZnGa₂O₄ into ZnO could be further determined by looking deeper into the Zn K-edge VtC-XES region. Typically, VtC spectra has two lines corresponding to Kβ_{2,5} (located below the Fermi level) and Kβ'' at lower fluorescence energy (Bergmann, U., *et al.*, *Chem. Phys. Lett.*, 1999. 302(1): p.119-124). At low Zn concentrations (2 and 4 wt%) the Kβ'' line was split because of the interaction from the metal (Zn) with s orbitals of O and d orbitals of Ga (**Figure 7.3**), this result was supported by the density of states calculations on the reference materials (details of calculation shown in **Table 7.1**). On the contrary, at high Zn loadings where ZnO phase was detected the Kβ'' line only contains the contribution of

s orbitals from O, indicating that first coordination shell of Zn atoms does not contain Ga atoms which might be attributed to the reduced accessibility of Zn atoms to the Ga_2O_3 surface, in agreement with the EXAFS analysis (Figure 7.4). In addition, the third emission line due to multielectron transitions (ME) from the emitted and absorbed photoelectrons is observed in the Zn K-edge VtC spectra (Figure 7.3). The intensity of this ME region is located below the Zn absorption edge energy and decreases with ZnO formation following the same trend that the photocatalytic activity results. However, correlation with the catalytic results are not discussed here because of the self-absorption effects that could also contribute to the ME intensity (Mortensen, D. R., *Phys. Rev. B.*, 2017. 96(12): p. 125136, and Valenza, R., *Phys. Rev. A.*, 2017. 96(3): p. 032504).

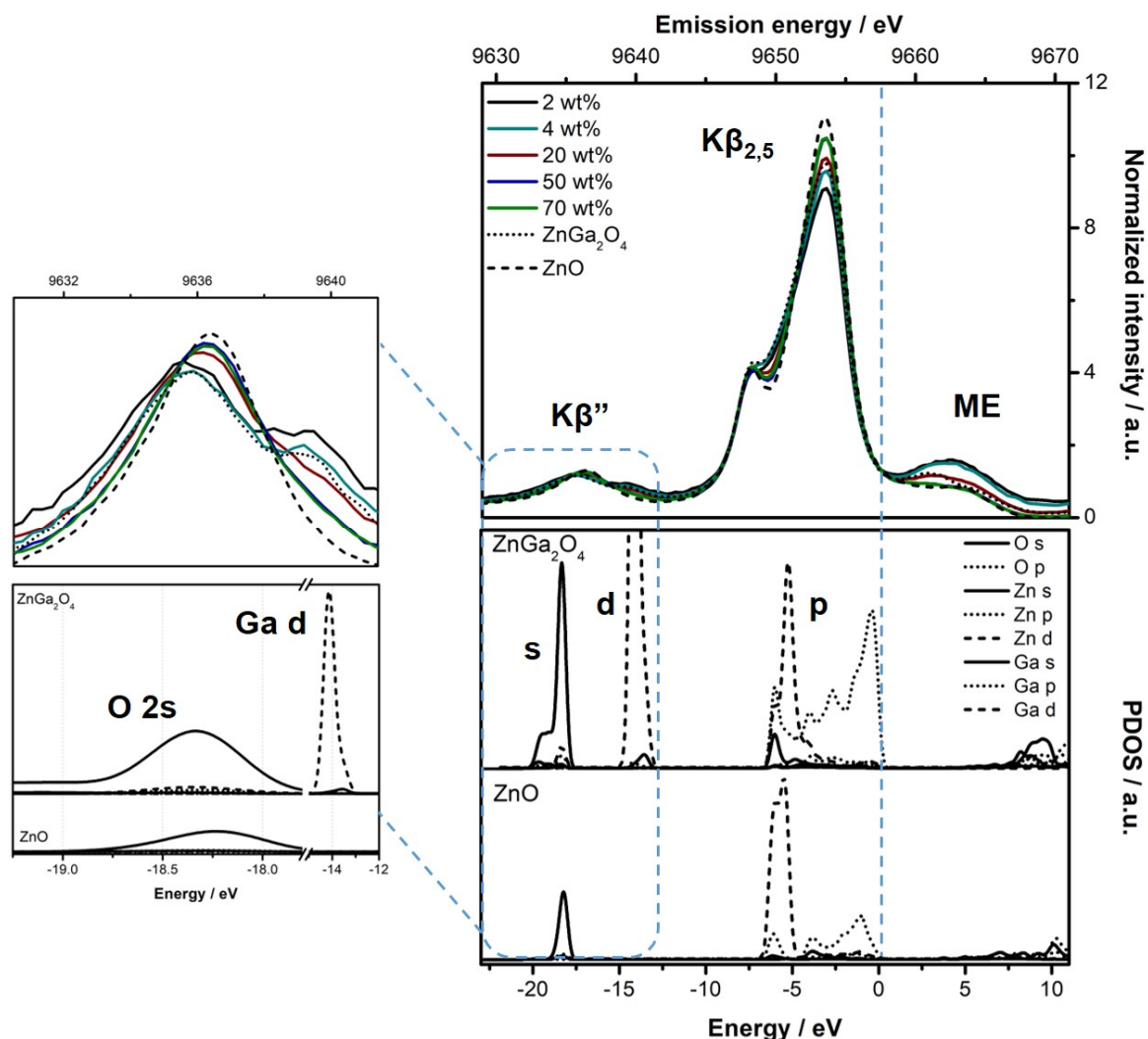


Figure 7.3. Zn K-edge VtC-XES with normalized intensity to the spectral area (top). PDOS calculations for O, Ga, and Zn where mainly s and p regions correspond to the $\text{K}\beta''$ and $\text{K}\beta_{2,5}$ lines, respectively. The dashed blue line indicates the Fermi level, and the zoomed region corresponds to $\text{K}\beta''$.

Appendices

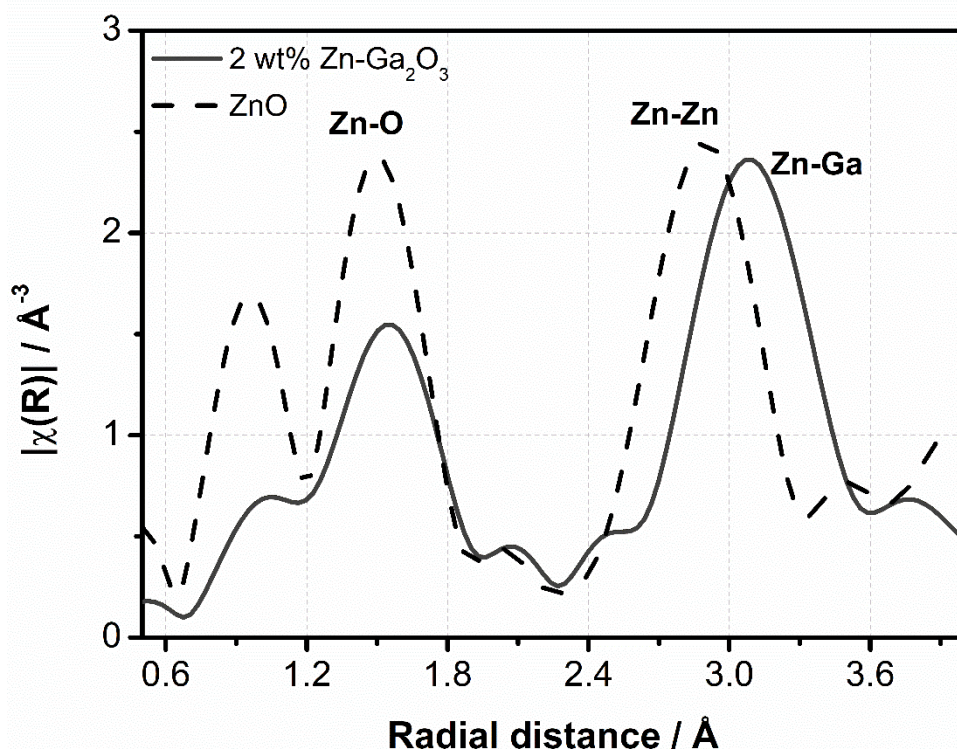


Figure 7.4. EXAFS analysis of low Zn content Ga_2O_3 (2 wt%) compared to ZnO (dotted line) reference material. Self-absorption correction was performed on the ZnO EXAFS data by using the Fluo algorithm (Haskel, 1999).

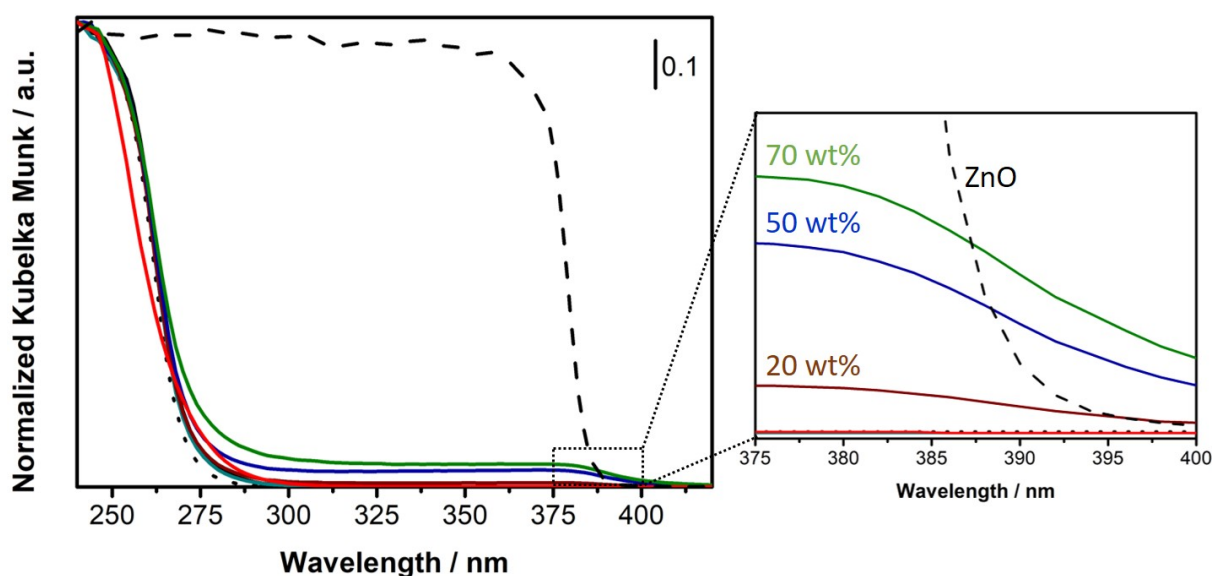


Figure 7.5. UV-vis DR spectra of $x\text{Zn-Ga}_2\text{O}_3$ materials with $x = 2$ (black), 4 (cyan), 20 (maroon), 50 (blue) and 70 (green) and of reference materials, ZnGa_2O_4 (red), Ga_2O_3 (dotted line) and ZnO (dashed line). Spectra are shown in normalized Kubelka Munk absorbance unit and the bandgaps were calculated from the slope of the adsorption spectra. Zoomed plot shows the region highlighting light absorption by ZnO.

For both Zn K-edge (**Figure 7.6-a**) and at Ga K-edge (**Figure 7.6-b**), opposite trends are observed for the unoccupied energy levels at the Zn and Ga absorption edges (inset plots, **Figure 7.6**). For the Zn K-edge, at small Zn concentrations (2 and 4 wt%) the lowest-unoccupied electronic states appear to be comparable to those of ZnGa₂O₄ (**Figure 7.6-a**), while at increasing Zn-loading where ZnO phase is more prominent, the absorption edges shift to lower energies, corresponding to smaller valance-conduction band gaps. This agrees with the UV-vis DRS study (**Figure 7.5**), at high Zn loading (≥ 20 wt%) a weak absorption extending in the visible region appears clearly due to the presence of ZnO, with the optical bandgap of 3.0-3.1 eV.

In contrast, the lowest-unoccupied energy states of Ga are shifted toward higher energies at higher Zn content, pure ZnGa₂O₄ shows the highest lowest-unoccupied energy state (**Figure 7.6-b**). The small shift of the unoccupied energy states of Ga at low Zn concentrations is likely attributed to the minor contribution of ZnGa₂O₄ phase for such Zn loadings.

Appendices

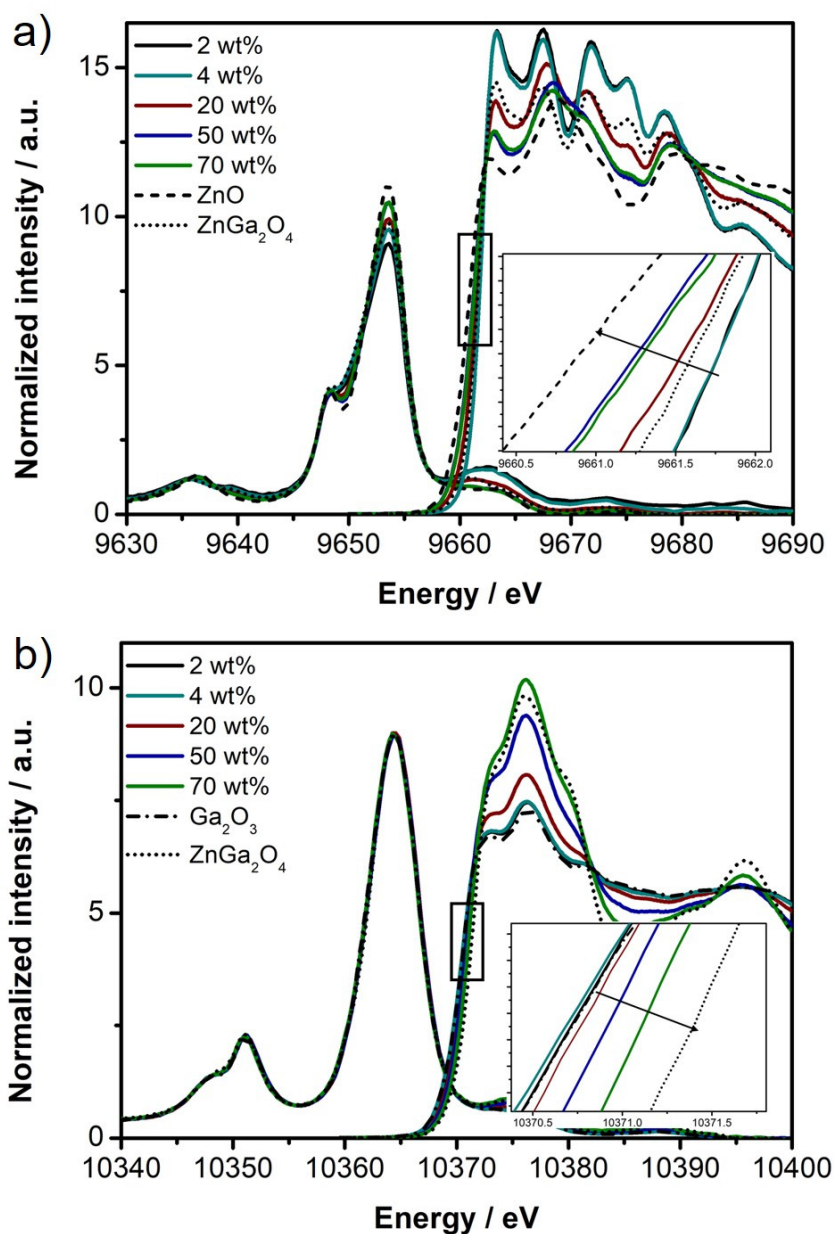


Figure 7.6. XAS and VtC-XES spectra for **a)** Zn K-edge and **b)** Ga K-edge. Pure ZnGa₂O₄ (dotted line), ZnO (dashed line), and Ga₂O₃ (dot-dashed line). Spectral intensity was normalized to the spectral area. Inset figures show the opposite energy changes of the absorption edge.

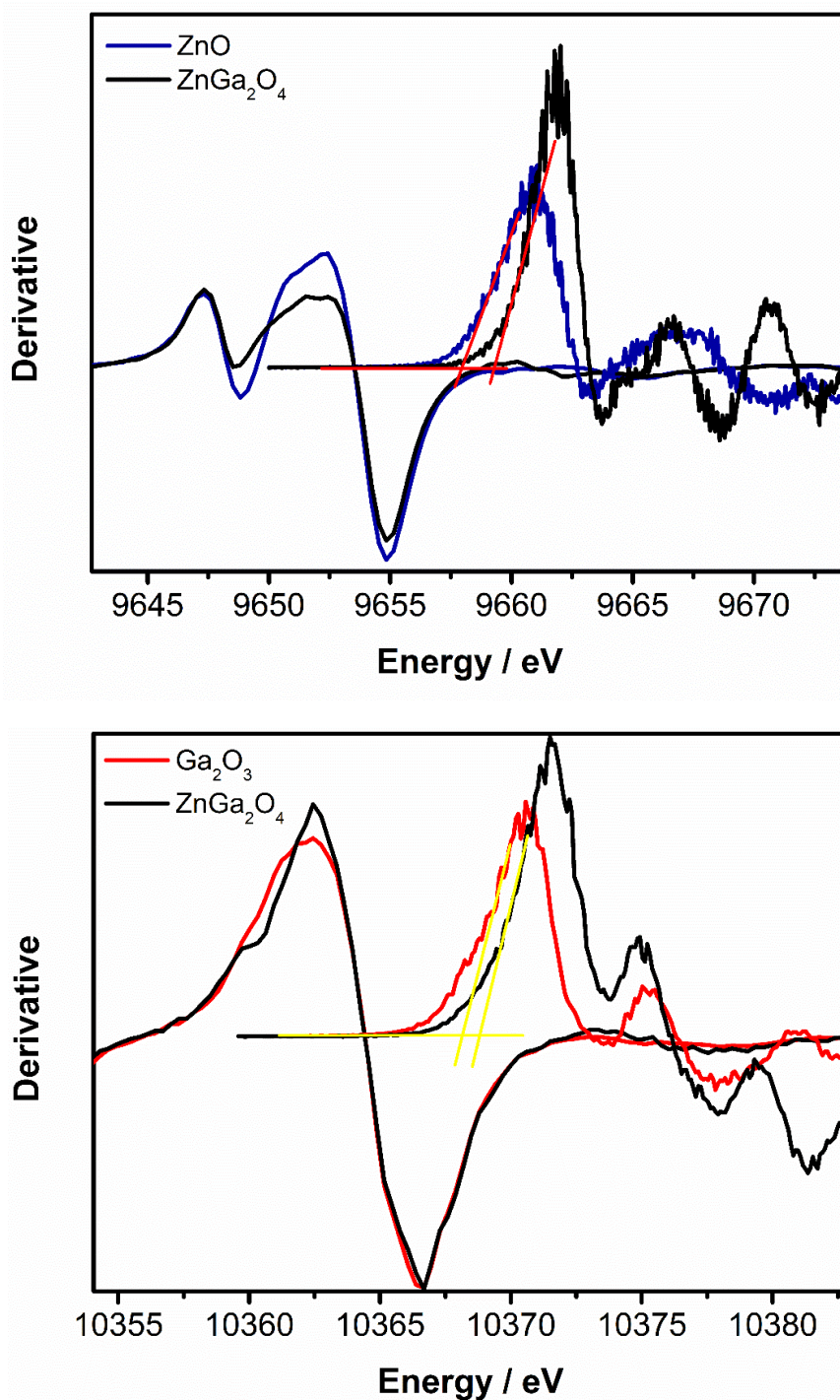


Figure 7.7 First derivative of XAS and VtC-XES spectra for Zn K-edge (**top**) and Ga K-edge (**bottom**). Red and yellow lines are positioned at the intersection between baseline at 0 intensity and the slope of the first derivative of XAS, and the intersection from baseline for XAS and XES was used to calculate the difference between the XAS and XES spectra.

Appendices

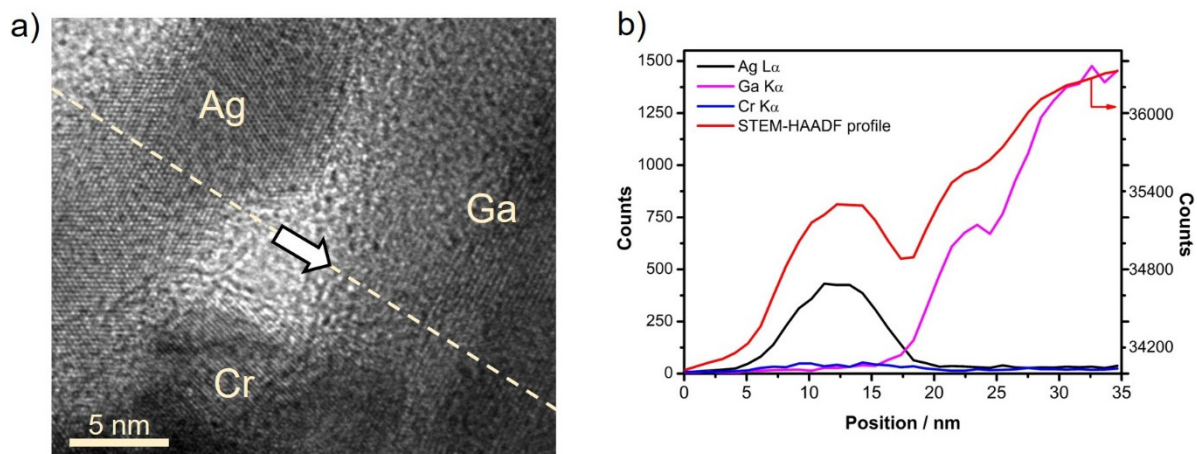


Figure 7.8. STEM-HAADF image of Rh-Cr/4 wt% Zn-Ga₂O₃, and elemental profiles over the diagonal for Ag (black), Cr (blue), and Ga (pink). Rh was not detected likely due to its low content.

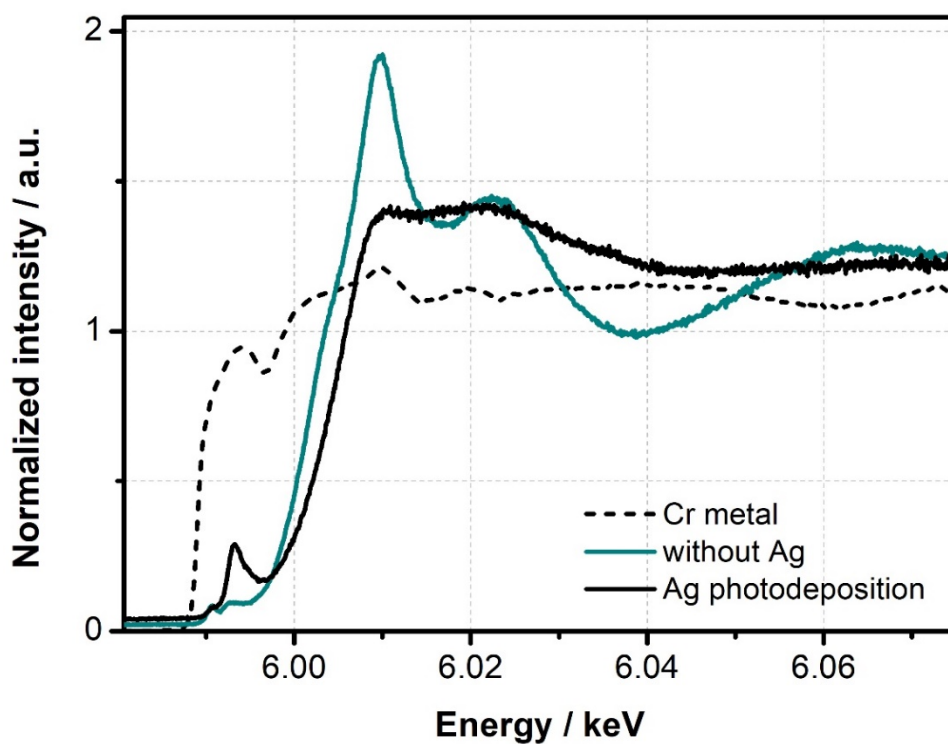


Figure 7.9. XANES spectra at Cr K-edge; Cr metal (dashed line), Rh-Cr/4 wt% Zn-Ga₂O₃ (cyan), and after silver photodeposition (black).

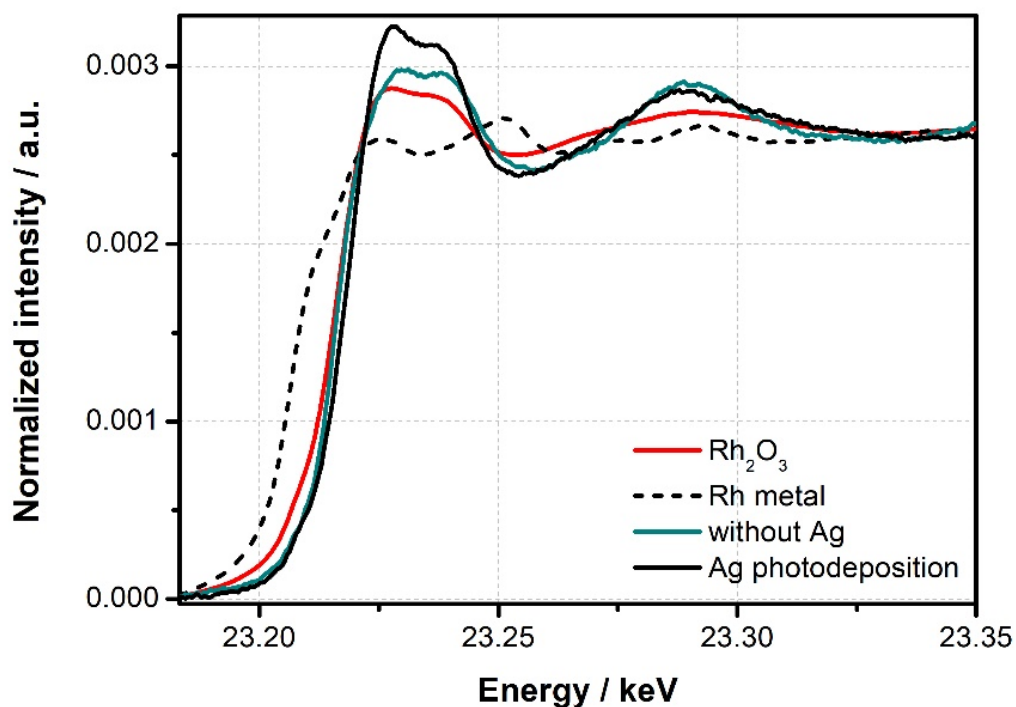


Figure 7.10. XANES spectra at Rh K-edge; Rh-Cr/4 wt% Zn-Ga₂O₃ (cyan), and after silver photodeposition (black). Rh₂O₃ (red) and metallic Rh (dashed lines) were used as reference materials.

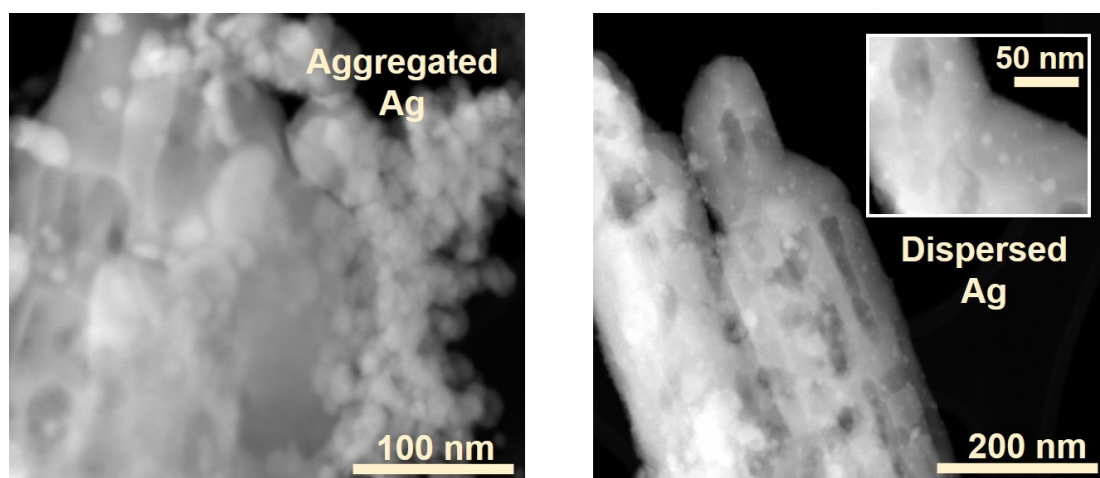


Figure 7.11. STEM-HAADF images of 20 wt% Ag deposited on Rh-Cr/4wt% Zn-Ga₂O₃ after photodeposition (**left**) and after impregnation (**right**).

Appendices

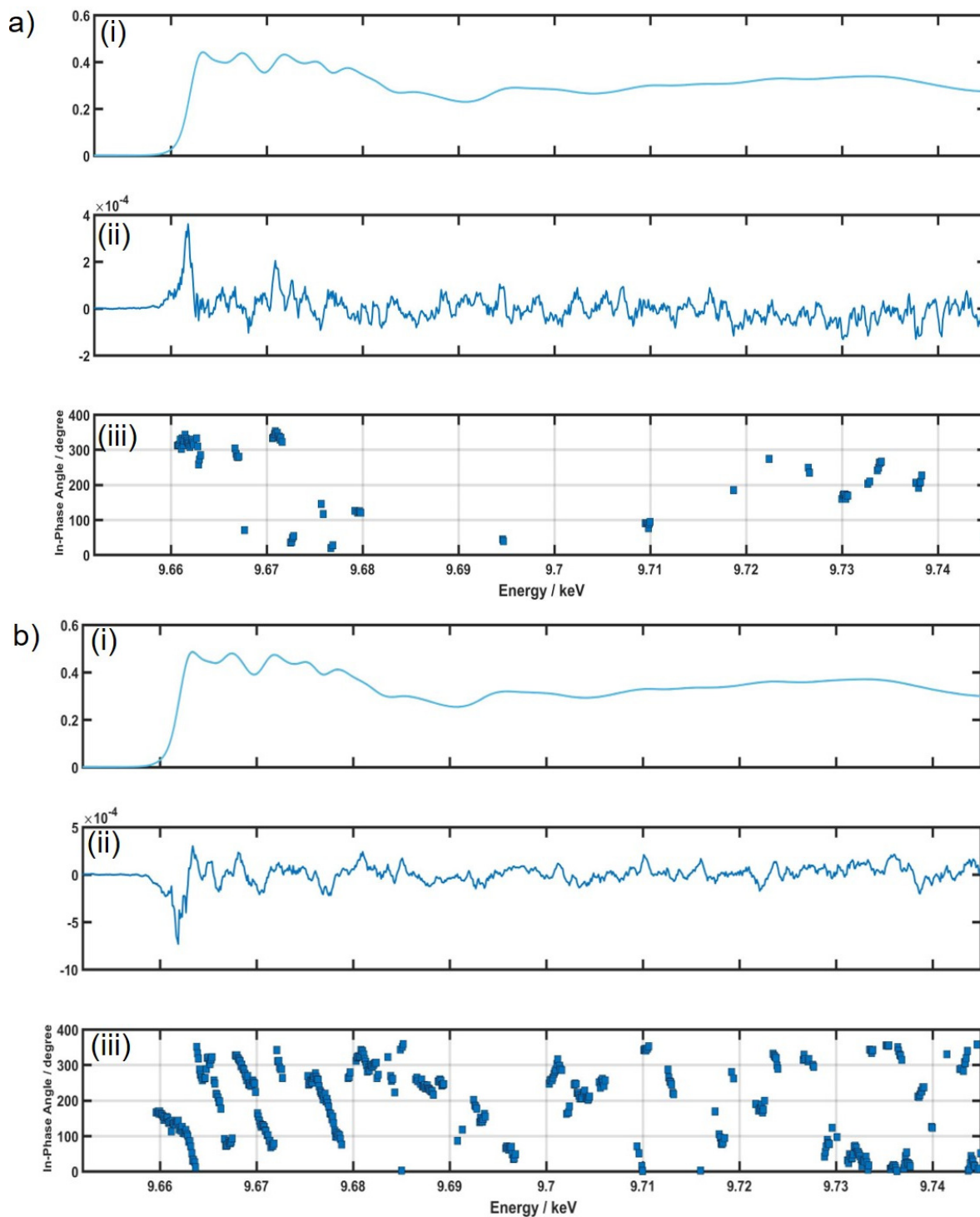


Figure 7.12. Zn-Kedge HERDF-XANES phase-domain spectra and in-phase angles analysis for a) 4wt% Zn-Ga₂O₃ and b) Rh-Cr/4wt% Zn-Ga₂O₃. The amplitude threshold to plot the in-phase angles was 0.0001.

Appendix B Supplementary Information of Chapter 4

Table 7.2. CH₄ and H₂ productivities obtained from the photoreduction of CO₂ with TiO₂, Pt/TiO₂, and Co/TiO₂. The activity (productivity) was calculated from the concentration profiles for each UV irradiation cycles (e.g. UV1 and UV2). The highest CH₄ and H₂ productivities observed in this work of are highlighted in orange and green, respectively.

	UV	CH ₄ ($\mu\text{mol g}_{\text{cat}}^{-1} \text{h}^{-1}$)	H ₂ ($\mu\text{mol g}_{\text{cat}}^{-1} \text{h}^{-1}$)	CH ₄ production respect to TiO ₂ (%)	H ₂ production respect to TiO ₂ (%)
TiO ₂	1	1.79	0.80	-	-
	2	0.74	0.51	-	-
Pt/TiO ₂	1	1.46	5.28	-	560
	2	0.62	1.57	-	208
Co/TiO ₂	1	2.58	1.52	44	90
	2	1.17	0.62	58	22

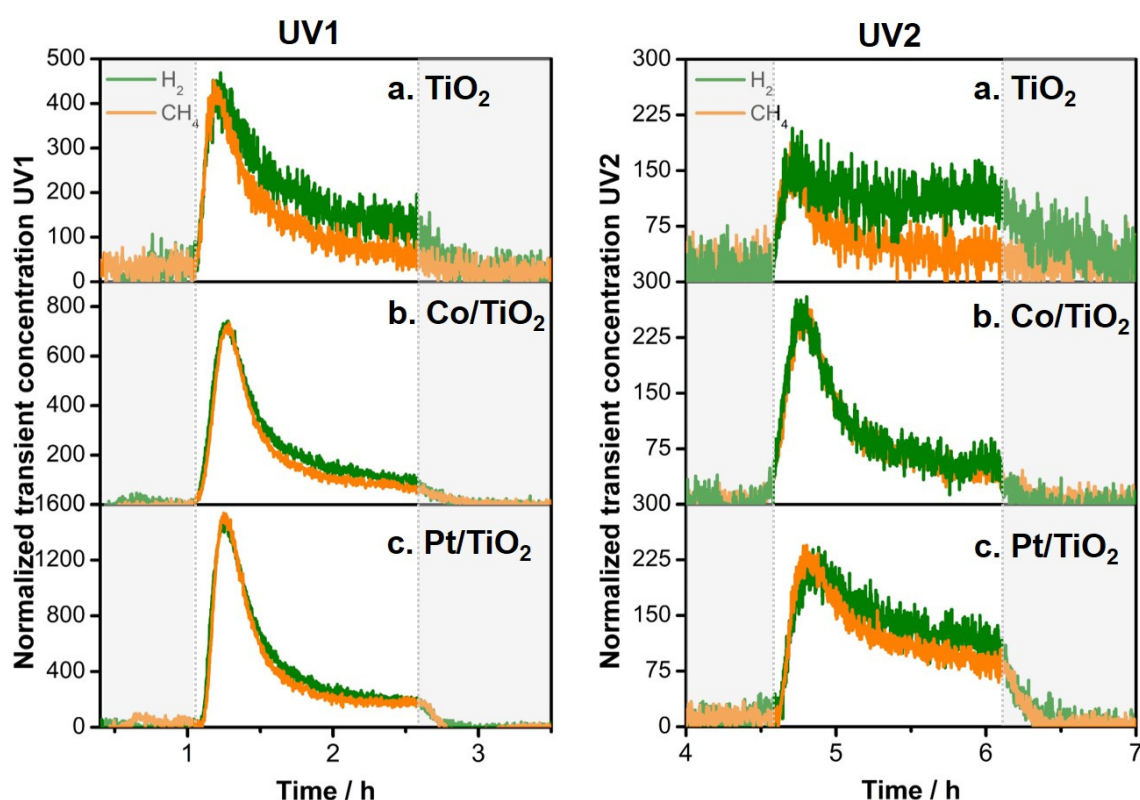


Figure 7.13. CH₄ (orange) and H₂ (green) concentration profiles normalized by the maximum concentration during UV1 (left) and UV2 (right) for **a)** TiO₂, **b)** Co/TiO₂, and **c)** Pt/TiO₂ in CO₂ photoreduction reaction at 423 K as shown in *chap. 4, section 4.3.1*.

Appendices

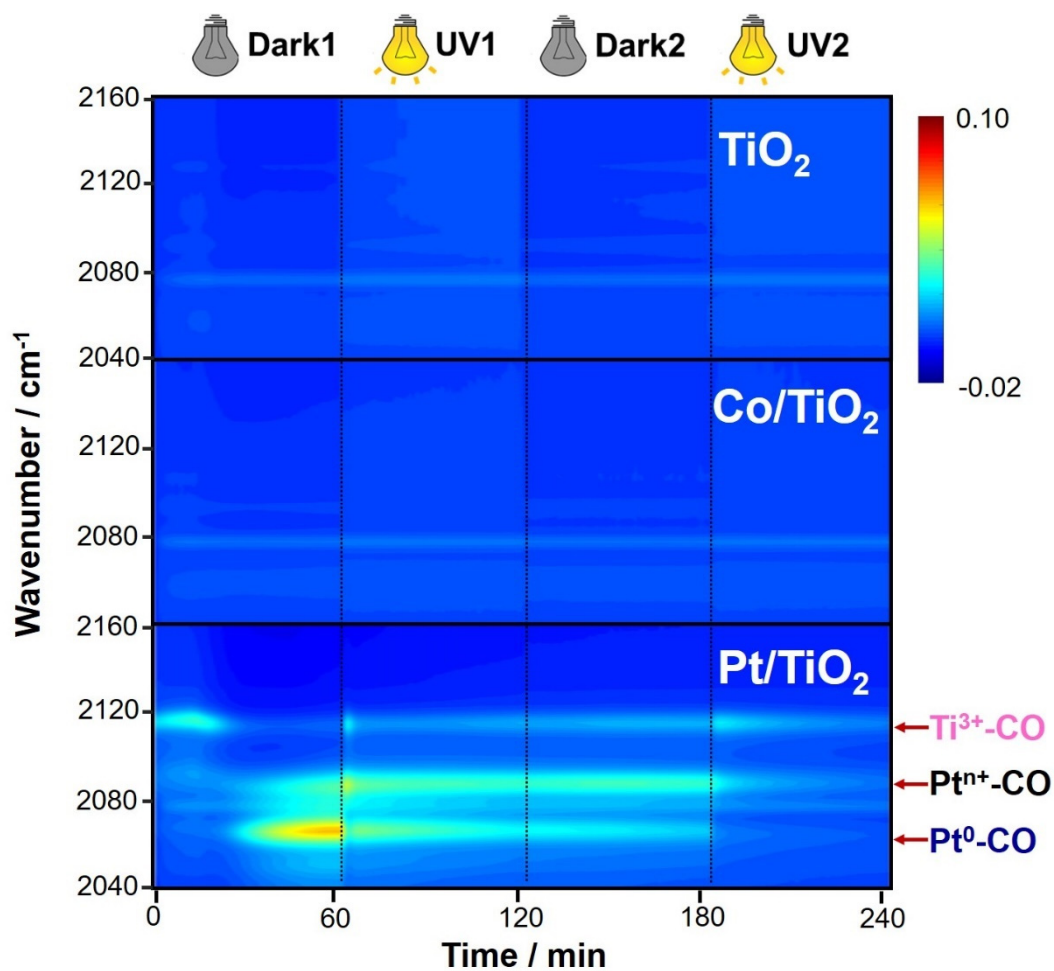


Figure 7.14. Evolution of carbonyl bands over TiO₂, Co/TiO₂, and Pt/TiO₂ (top to bottom) during CO₂ photoreduction reaction during Dark1, UV1, Dark2, and UV2. Surface carbonyl species on Ti³⁺, Ptⁿ⁺, and Pt⁰ observed for Pt/TiO₂ to are highlighted. Absorbance ranges from -0.02 (blue) to 0.10 (red).

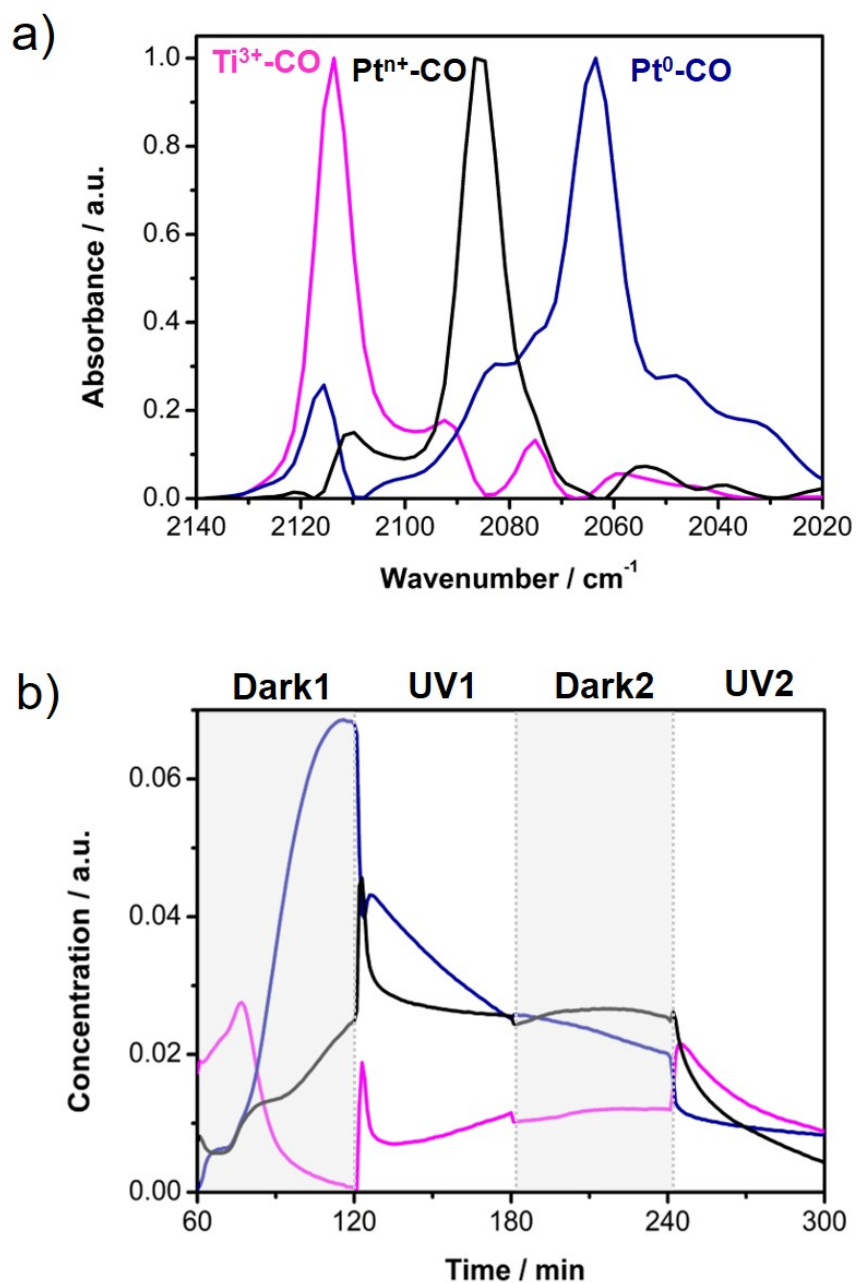


Figure 7.15. a) Component spectra and b) concentration profiles of the carbonyl species observed over Pt/TiO₂ during CO₂ photoreduction reaction. Three carbonyl species on Pt⁰ (blue), oxidized Pt (black), and Ti³⁺ (magenta) are identified.

Appendices

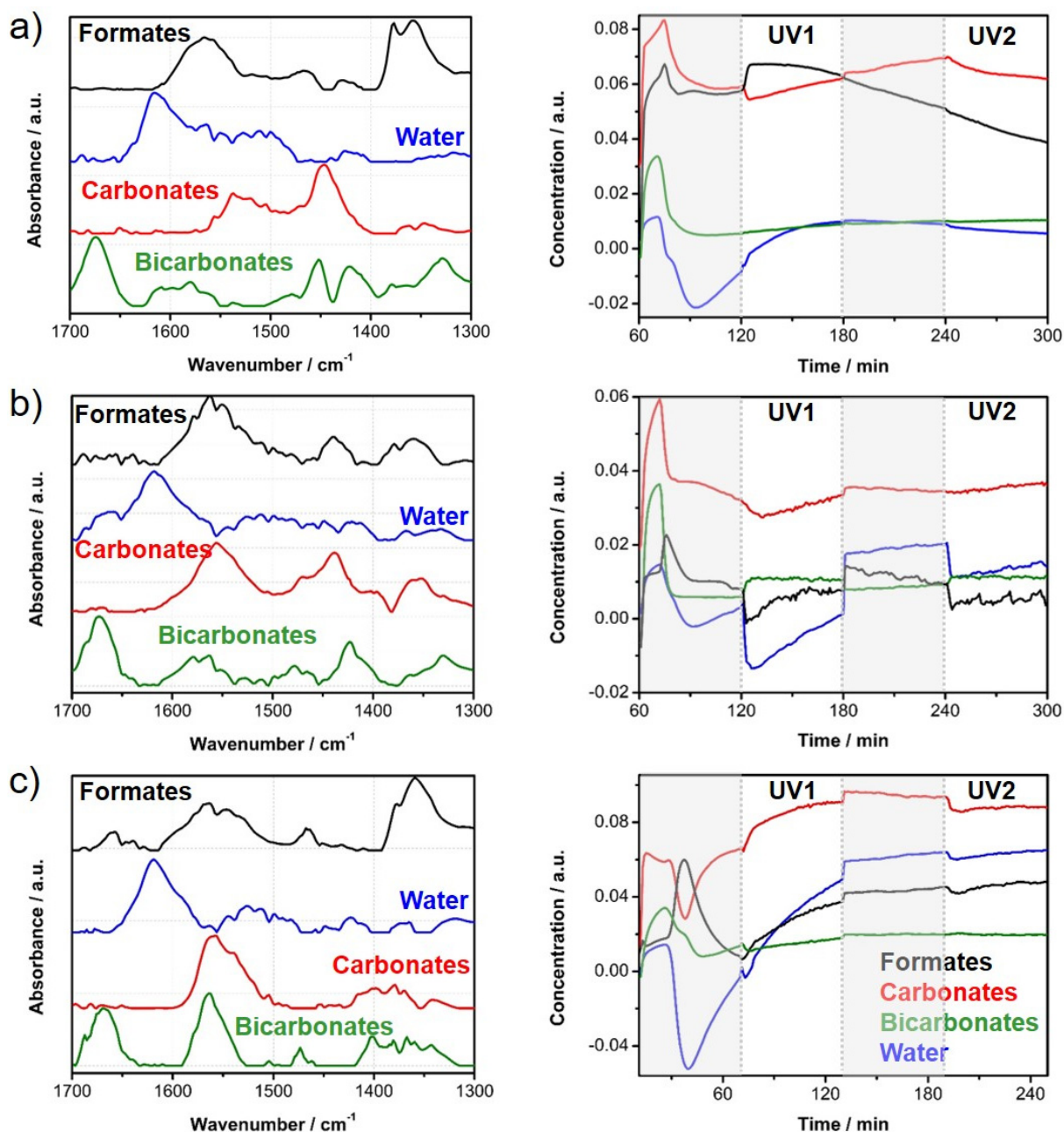


Figure 7.16. Component spectra and concentration profiles obtained by the MCR analysis of the low frequency region ($1300\text{-}1700\text{ cm}^{-1}$) for **a)** Pt/TiO₂, **b)** Co/TiO₂, and **c)** TiO₂. Spectra and concentration profiles are for formate (black), carbonates (red), bicarbonates (green), and water (blue) surface adsorbed species.

Table 7.3. Comparison between experimental and reported bands used on the assignments of surface species from the component spectra on [Figure 7.16](#) at low IR frequency region.

Experimental bands (cm ⁻¹)	Reported bands (cm ⁻¹)	Attributed to	Reference
1675 and 1450 (Pt) 1672 and 1425 (Co)	• 1600 and 1470 • 1620 and 1453 • 1673 and 1430	• Bidentate bicarbonates • Bicarbonates • Bicarbonates	• Kondo, J. et al. <i>J. Chem. Soc. Faraday Trans.</i> , 1988, 84 (2): p. 511-519 • Guglielminotti, E. <i>Langmuir</i> , 1990, 6 (9): p. 1455-1460 • Bando, K. K. et al. <i>Appl. Catal. A</i> , 1997, 165 : p. 391-409, Turek, A. et al. <i>J Phys. Chem.</i> , 1992, 96 (12): p. 5000-5007
1550 and 1340 (Pt) 1560 and 1330 (Co)	• 1556 and 1325 • 1595 and 1282 • 1579 and 1319 • 1550 and 1310	• Bidentate carbonates • Bidentate carbonates • Bidentate carbonates • Bidentate carbonates	• Bianchi, D. et al. <i>Appl. Catal. A</i> , 1994, 112 (2): p. 219-235 • Kondo, J. et al. <i>J. Chem. Soc. Faraday Trans.</i> , 1988, 84 (2): p. 511-519 • Liao, L.F. et al. <i>J. Phys. Chem. B</i> , 2002, 106 (43): p. 11240-11245 • Guglielminotti, E. <i>Langmuir</i> , 1990, 6 (9): p. 1455-1460
1438 (Co) 1440 (Pt)	• 1483 and 1373 • 1461	• Unidentate carbonates • Monodentate carbonates	• Kondo, J. et al. <i>J. Chem. Soc. Faraday Trans.</i> , 1988, 84 (2): p. 511-519 • Liao, L.F. et al. <i>J. Phys. Chem. B</i> , 2002, 106 (43): p. 11240-11245
1560, 1380, 1360 (Pt) 1560 and 1360 (Co)	• 2966, 2875, 1586, 1385, 1361 • 1555 and 1370 • 2885-95, 1562, 1370, 1390 • 2933, 2858, 1591, 1353 • 2945, 2921, 2867, 1323	• Formates • Formates • Formates • Formates • Formic acid	• Kondo, J. et al. <i>J. Chem. Soc. Faraday Trans.</i> , 1988, 84 (2): p. 511-519 • Liao, L.F. et al. <i>J. Phys. Chem. B</i> , 2002, 106 (43): p. 11240-11245 • Guglielminotti, E. <i>Langmuir</i> , 1990, 6 (9): p. 1455-1460 • Bando, K. K. et al. <i>Appl. Catal. A</i> , 1997, 165 : p. 391-409 • Miller, K.L. et al. <i>J. Catal</i> , 2010, 275 (2): p. 294-299

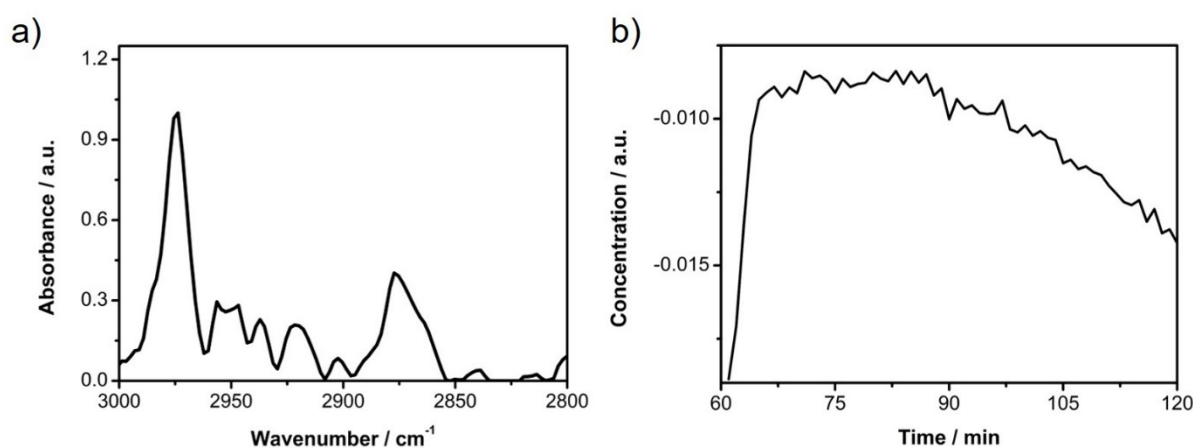


Figure 7.17. a) Component spectrum and b) concentration profile of formate species over Pt/TiO₂ during UV1 obtained by the MCR analysis of the CH region between 2800-3050 cm⁻¹.

Appendices

Raman measurements were performed using a BWTEK dispersive i-Raman portable spectrometer equipped with 785 nm excitation laser and a TE-cooled linear array detector. Samples before and after CO₂ photoreduction reaction were measured in powder form.

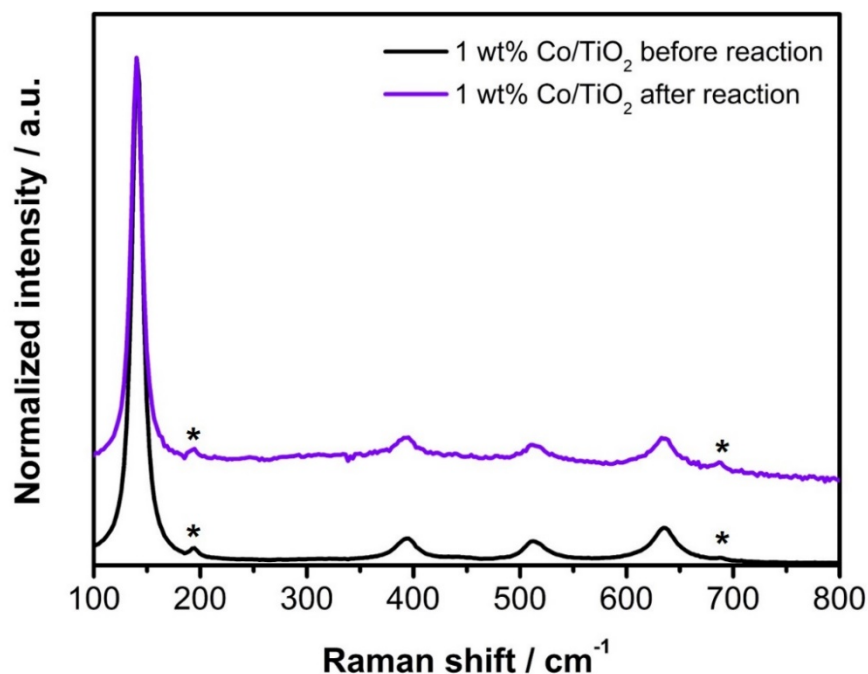


Figure 7.18. Raman spectra of 1 wt% Co/TiO₂ before and after performing the photocatalytic CO₂ reduction with 785 nm excitation laser. 1 wt% Co-loading is shown because for low concentration (e.g. 0.2 wt%) of cobalt signals from Co₃O₄ were not identified. Raman peaks marked with (*) correspond to Co₃O₄ reference material (Jiang, J. and L. Li, *Materials Letters*, 2007. 61(27): p. 4894-4896).

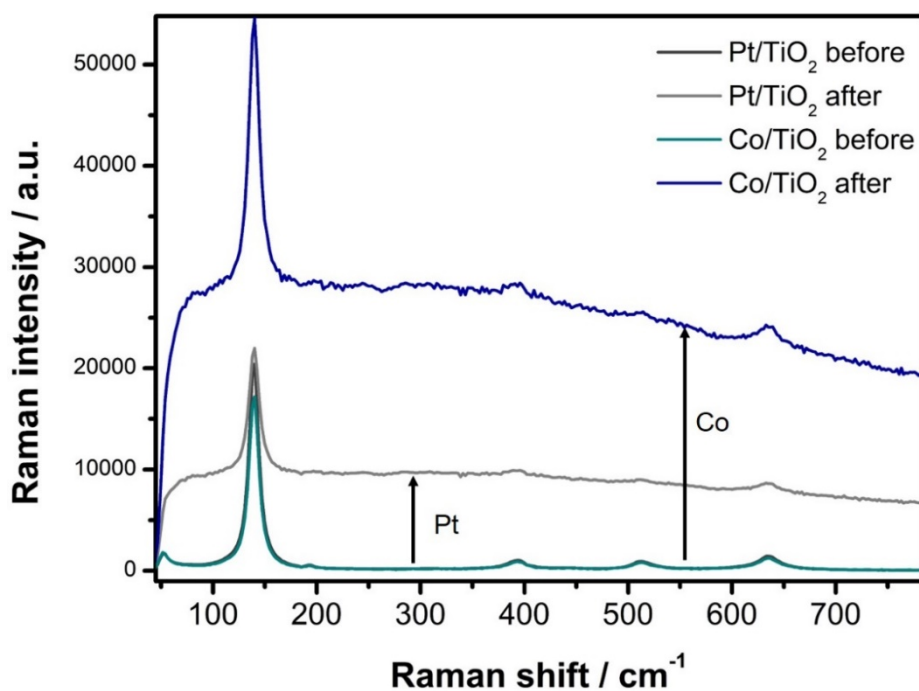


Figure 7.19. Raman spectra of Pt/TiO₂ and Co/TiO₂ (0.2 wt% of metal loading) before and after CO₂ photoreduction reaction with 785 nm excitation laser.

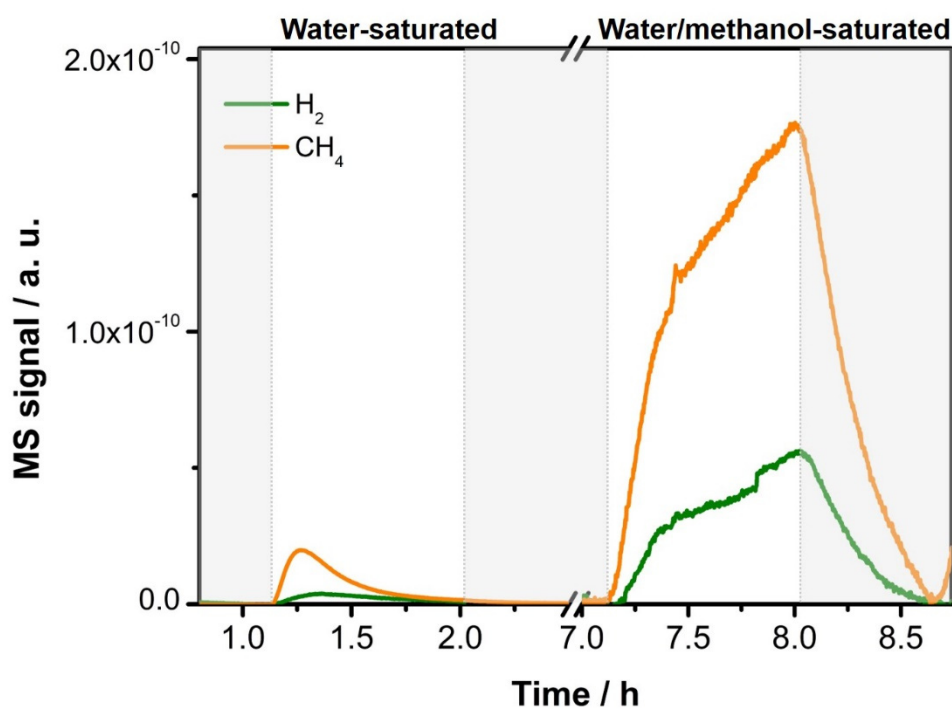


Figure 7.20. Concentration profile (MS) of CH₄ (orange) and H₂ (green) during CO₂ photoreduction reaction over TiO₂. Two light off/on (grey region indicates light off) cycles were performed under the atmosphere of CO₂ saturated with **a**) water vapour and **b**) water/methanol vapour (10% v/v methanol).

Appendices

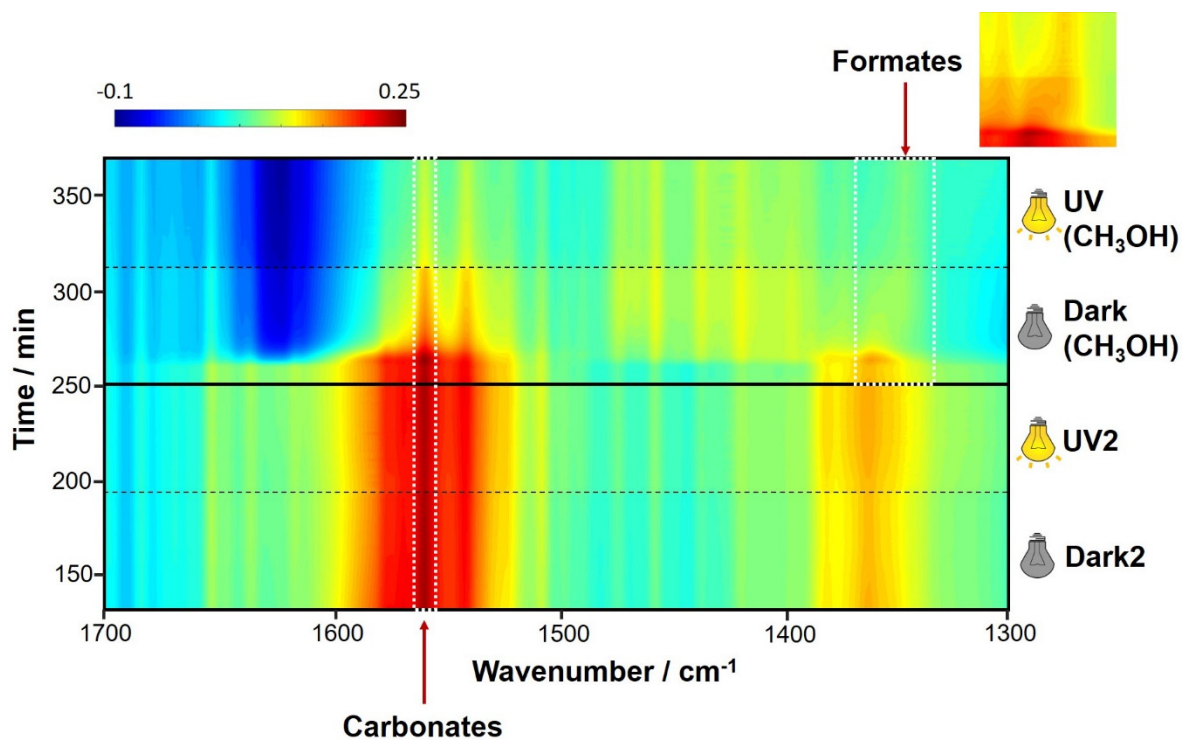


Figure 7.21. *In situ* DRIFT spectra during Dark2, UV2, Dark (CH₃OH), and UV (CH₃OH), from bottom to top, observed for bare TiO₂ during the CO₂ photoreduction reaction at 423 K. After two light off/on, an additional light off/on cycle was evaluated by passing CO₂ saturated with water/methanol (10% v/v methanol). Absorbance is from -0.1 (blue) to 0.25 (red).

Appendices

Shorthand and glossary

ΔG^0	Gibbs free energy
ALS	Alternating least squares
<i>Appx.</i>	Appendix
ATR	Attenuated total reflection
CB	Conduction band
<i>Chap.</i>	Chapter
CV	Cyclic voltammetry
DFT	Density functional theory
DOS	Density of states
DRIFTS	Diffuse reflectance infrared Fourier transformed spectroscopy
DRS	Diffuse reflectance spectroscopy
EDX	Energy-dispersive X-ray spectroscopy
E_f	Fermi level energy
E_g	Bandgap
E_{red}^0	Standard reduction potential
ESRF	European Synchrotron Radiation Facility
E_x	Electron affinity
EXAFS	X-ray absorption fine structure spectroscopy
FTIR	Fourier transformed infrared
FTO	Fluorine doped tin oxide electrode
GC	Gas chromatograph
GC-MS	Gas chromatography coupled with mass spectrometry

Shorthand and glossary

GO	Graphene oxide
HAADF	High annular dark-field imaging mode
HER	Hydrogen evolution reaction
HERFD	High energy resolution fluorescence detected
IR	Infrared
IRRAS	Reflection-absorption infrared spectroscopy
I-V	Current density versus potential curves
$j_{k,HER}$	Kinetic current for HER
$j_{k,OER}$	Kinetic current for OER
LCA	Linear combination analysis
LCF	Linear combination fitting
LED	Light-emitting diode
LN-MCT	Liquid nitrogen cooled HgCdTe detector
LSPR	Localized surface plasmonic resonance
LSV	Linear sweep voltammetry
MCR	Multivariate curve resolution
MES	Modulation excitation spectroscopy
MFC	Mass flow controller
MS	Mass spectrometer
NASA	National Aeronautics and Space Administration
NHE	Normal hydrogen electrode
OER	Oxygen evolution reaction
ORR	Oxygen reduction reaction
PEC	Photoelectrochemical cell

PSD	Phase-sensitive detection
PXRD	Powder X-ray diffraction
RDE	Rotating disk electrode
RGO	Reduced graphene oxide
Rh-Cr	$\text{Rh}_{2-y}\text{Cr}_y\text{O}_3$
RHE	Reference hydrogen electrode
RPM	Rotations per minute
S/N	Signal-to-noise ratio
STEM	Scanning transmission electron microscopy
TEM	Transmission electron microscopy
UV	Ultraviolet light
VB	Valance band
Vis	Visible light
VtC	Valance-to-core
XANES	X-ray absorption near-edge structure spectroscopy
XAS	X-ray absorption spectroscopy
XES	X-ray emission spectroscopy
ϕ	Semiconductor work function

Shorthand and glossary

List of publications

JOURNAL PUBLICATIONS

1. CO₂ Activation over Catalytic Surfaces.

Andrea Álvarez, **Marta Borges**, Juan José Corral-Pérez, Joan Olcina, Lingjun Hu, Daminen Cornu, Rui Huang, Dragos Stoian, Atsushi Urakawa, *ChemPhysChem*, 18 (2017) 3135.

2. Synergistic interplay of Zn and Rh-Cr promoters on Ga₂O₃ based photocatalysts for water splitting.

Marta Borges Ordoño, Shunsaku Yasumura, Pieter Glatzel, and Atsushi Urakawa. *Phys. Chem. Chem. Phys.*, 20 (2018) 23515

3. Spectroscopic insights into the active species under UV light over Pt or Co modified TiO₂ for CO₂ photocatalytic reduction.

Marta Borges Ordoño and Atsushi Urakawa. *Manuscript in preparation*

List of publications

CONFERENCE CONTRIBUTIONS

1. August **2018**, Tokyo Conference on Advanced Catalytic Science and Technology (TOCAT), Yokohama (Japan) – **posters presentation**

- a) Spectroscopic insights into the active species under UV light over Pt or Co modified TiO₂ for CO₂ photoreduction reaction
- b) Synergistic interplay of Zn and Rh-Cr promoters on Ga₂O₃ based photocatalysts for water splitting

Marta Borges and Atsushi Urakawa

2. August **2017**, 13th European Congress on Catalysis (EUROPACAT), Florence (Italy) – **posters presentation**

- a) Synergetic interplay of Co and TiO₂ in continuous CO₂ photoreduction to CH₄
- b) Insights into H₂ and O₂ evolution sites through selective Ag deposition over Rh-Cr/Zn-modified Ga₂O₃

Marta Borges and Atsushi Urakawa

3. June **2017**, ICIQ PhD day, Tarragona (Spain) – **flash presentation.**

Insights into oxygen and hydrogen evolution sites through site selective Ag deposition over Rh-Cr promoted Zn-Ga₂O₃.

Marta Borges and Atsushi Urakawa

4. June **2016**, 9th European Meeting on Solar Chemistry and Photocatalysis: Environmental Applications (SPEA9), Strasbourg (France) – **poster presentation.** Electrochemical method as supportive characterization to evaluate promoter effects in half-reactions of photocatalytic water splitting.

Marta Borges and Atsushi Urakawa

5. July **2015**, UniCat Summer School, Berlin (Germany) – **poster presentation.** Origin of Zn and Rh-Cr promotion to wide-bandgap metal oxides in photocatalytic water splitting.

Marta Borges, Antonio Bazzo, and Atsushi Urakawa

6. July **2015**, Sociedad Española de Catálisis (SECAT), Barcelona (Spain) – **oral presentation**.

Influence of Synthesis Methods on the Formation of Active Sites in Zn-doped Ga₂O₃ for Photocatalytic Water Splitting.

Marta Borges and Atsushi Urakawa

7. June **2015**, Japan-Spain symposium, Tarragona (Spain) – **poster presentation**.

Origin of Zn and Rh-Cr promotion to wide-bandgap metal oxides in photocatalytic water splitting.

Marta Borges, Antonio Bazzo, and Atsushi Urakawa

List of publications

Curriculum Vitae

PERSONAL INFORMATION

Name	Marta Borges Ordoño
Date of birth	September 29 th , 1988
Place of birth	Olot, Girona (Spain)
Nationality	Spanish
Email	marta.borgem@gmail.com

EDUCATIONAL BACKGROUND

2014 – Present, PhD in Heterogeneous Catalysis

The Institute of Chemical Research of Catalonia (ICIQ) and University Rovira i Virgili, Tarragona-Spain

PhD thesis under the supervision of Prof. Dr. Atsushi Urakawa. Thesis project focused on the evaluation of continuous photocatalytic CO₂ reduction reaction into valuable chemical compounds. Photocatalytic materials were modified with co-catalysts and further investigated by spectroscopic techniques and electrochemical methods.

09/2017-12/2017, research stay at the City University of Hong Kong (HK) under the supervision of Prof. Dr. Wey Yang Teoh. Project based on the rational design of semiconductor materials for CO₂ photoreduction and its evaluation using electrochemical techniques (rotating disk electrode and photoelectrochemical cell).

Research topics:

- Reaction engineering, CO₂ conversion, photocatalysis
- Mechanistic studies using *in situ* and *ex situ* characterization techniques mainly based on X-ray adsorption and emission (synchrotron radiation) and diffuse reflectance infrared Fourier transformed spectroscopies

Grants:

- Severo Ochoa 2014 (SVP-2014-068551)

Curriculum Vitae

2013 – 2014, Masters in Nanotechnology and Materials Science

Autonomous University of Barcelona and Catalan Institute of Nanoscience and Nanomaterials (ICN2), Barcelona-Spain (8.6/10)

Master thesis under the supervision of Prof. Daniel Ruiz-Molina. Research project focused on the encapsulation of metallic nanoparticles in coordination polymers (CPPs) as dual contrast agents for Magnetic Resonance Imaging (MRI) in collaboration with The Catalan Institute of Materials of Barcelona (ICMAB).

Subjects: preparation of materials and nanomaterials, advanced characterization techniques at the nanoscale, nanomedicine and nanochemistry.

2006 – 2011, Chemistry Degree

University Rovira i Virgili, Tarragona-Spain (7.2/10)

02/2011-06/2011, final Degree project (ERASMUS) under the supervision of Dr. Paul Collier at Johnson Matthey Technology Centre (UK). The main objective of the project was to find a method for loading metal particles into metal-organic frameworks (MOFs) to obtain a bimetallic system with two active sites for gas adsorption applications.

Subjects: Organic Chemistry, Inorganic Chemistry, Analytical Chemistry, Physical Chemistry.

WORK EXPERIENCE

2014, Research Scientist

Johnson Matthey Technology Centre, Sonning Common, Reading-UK

Inks preparation with doped zeolites. Optimisation of ink printing by using different polymers as binders. Characterization and testing for internal applications.

2011 – 2013, Research Scientist

Johnson Matthey Technology Centre, Sonning Common, Reading-UK

Research topics:

- Development and improvement of current synthesis methods to make Metal-organic frameworks (MOFs) as part of the EU project NANOMOF. The main objective was the design of scale up process to supply MOFs for the EU project partners
- Optimization of solvent-free synthesis methodologies to be applied on the MOFs synthesis and structural characterization
- Synthesis of zeolitic imidazolate frameworks (ZIFs) as an alternative support for metal particles for EU project CATAPULT. The objective was to reduce the platinum content of a fuel cell by developing a free platinum catalyst capable to provide high mass activity and durability

Personal achievements:

- Novel preparation to obtain from gram to kg scale of MOFs and delivery to the EU project partners reaching the targeted deadline
- I have been involved in all the steps to make MOFs materials, from the laboratory scale to the kg scale, including processing and characterization
- Internal presentations and monthly reports on progress work
- Presentations to the EU commission for 6 monthly project reviews
- I have learnt and strength my networking abilities during travelling around Europe

Other duties and skills acquired:

- Time and project management skills
- Communicational skills - Report writing and presentation for internal and external purposes
- Attendance of various technical conferences
- Critical thinking

SEMINARS AND COURSES

- Metal-organic frameworks (MOF2012), Edinburgh (UK)
- Sociedad Española de Catálisis (SECAT'15) with oral contribution, Barcelona (Spain)

Curriculum Vitae

- 9th European Meeting on Solar Chemistry and Photocatalysis: Environmental Applications (SPEA9), poster contribution, Strasbourg (France)
- 13th European Congress on Catalysis (EUROPACAT), posters contribution, Florence (Italy)
- Tokyo Conference on Advanced Catalytic Science and Technology (TOCAT8), posters contributions, Yokohama (Japan). Poster award.



**UNIVERSITAT
ROVIRA i VIRGILI**